UNIVERSITY OF TECHNOLOGY SYDNEY
Faculty of Engineering and Information Technology

Novel Control Strategies for Smart Electrical Car Parks

by

Tingting He

A Thesis Submitted
in Partial Fulfillment of the
Requirements for the Degree

Doctor of Philosophy

Sydney, NSW, Australia

2018

Certificate of Authorship/Originality

I certify that the work in this thesis has not been previously submitted for a degree nor has it been submitted as a part of the requirements for other degree except as fully acknowledged within the text.

I also certify that this thesis has been written by me. Any help that I have received in my research and in the preparation of the thesis itself has been fully acknowledged. In addition, I certify that all information sources and literature used are quoted in the thesis.

Acknowledgements

I would like to thank all those people who contributed one way or another towards the completion of this thesis. I highly appreciate the expert supervision, guidance, encouragement and financial support from my supervisor, Professor Jianguo Zhu throughout this thesis research. Associate Professor Dylan Lu has been a constant source of insightful thoughts, inspiration and guidance. I have benefited greatly, on numerous occasions, from his timely advice, continuous encouragement, and generous support over the years. I also would like to thank our group members Associate Professor Li Li, Dr Gang Lei and Associate Professor Youguang Guo for their time and valuable suggestions.

I would like to thank all my other friends in the Electrical Engineering Department for the good times I shared with them. Mr Tianshi Wang, Mr Shuo Wang, Mr Linfeng Zheng and Mr Jianwei Zhang were always there for me whenever I needed assistance with the experimental test on the dSPACE software and the hardware detection. Mr Tran-Hiep Dinh, Mr Sayed Royal and Miss Xinchi Wei always helped me with my studying.

I would like to express my special gratitude to my parents, Xiaoping Chen and Jing He, and my boyfriend Yingjie Bai for their love, their sacrifices without which I could not have achieved my goal. They were always ready to lend an ear when I needed to talk to someone to relieve the pressures of the day.

Finally, I acknowledge the financial support from the China Scholarship Council. Without the support, funding, opportunities, and encouragement offered to me from each of these, I would not have been able to complete this dissertation and degree.

Tingting He

Sydney, NSW, Australia, 2018.

Contents

List of Figures

List of Tables

Abbreviations

AEMO - Australia Energy Market Operator

DPC - Direct Power Control

DTC - Direct Torque Control

EV - Electric Vehicle

G2V - Grid-to-Vehicle

ICE - Internal Combustion Engine

IGBT - Insulated-Gate-Bipolar-Transistor

KVL - Kirchhoff's Voltage Law

MMPC - Modified Model Predictive Control

MPC - Model Predictive Control

MPDCC - Model Predictive Direct Current Control

MPDPC - Model Predictive Direct Power Control

MPPIC - Model Predictive Proportional Integral Control

MPSMC - Model Predictive Sliding Mode Control

PFC - Power Factor Correction

PHEV - Plug-in Electric Vehicle

PI - Proportional Integral

PLL - Phase Locked Loop

PWM - Pulse Width Modulation

SMC - Sliding Mode Control

SOC - State of Charge

SVC - Static Var Compensator

SVPWM - Space Vector Pulse Width Modulation

THD - Total Harmonic Distortion

UTS - University of Technology Sydney

VOC - Voltage Oriented Control

V2G - Vehicle-to-Grid

V2V - Vehicle-to-Vehicle

V4G - Vehicle-for-Grid

WPAN - Wireless Personal Area Networks

Symbols

m - the mth EV

M - the total number of EVs

n - the nth period

N - the total periods

N_m - the total parking periods of the mth EV

E_m^n - the energy of the mth EV in the nth period (kWh)

E_m - the current stored energy of the mth EV (kWh)

$E_{m,c}^n$ - the charging energy of the mth EV (kWh)

$E_{m,d}^n$ - the discharging energy of the mth EV (kWh)

C_m - the battery capacity of the mth EV (kWh)

$SOC_{m,fin}$ - the final SOC of the mth EV (%)

$SOC_{m,ini}$ - the initial SOC of the mth EV (%)

p_m^n - the charging/discharging power of the mth EV in the nth period (kW)

$p_{m,c,max}$ - the maximum charging power of the mth EV (kW)

$p_{m,c,max}$ - the maximum charging power of the mth EV (kW)

$p_{m,d,max}$ - the maximum discharging power of the mth EV (kW)

$\mathbf{S}_{\alpha\beta}$ - the switching states in the $\alpha\beta$ coordinate

$\mathbf{S_{abc}}$ - the switching state vector in the *abc* coordinate

$\mathbf{v}_{\alpha\beta}$ - the input voltage vector of the three-phase converter in $\alpha\beta$ coordinate

$\mathbf{v}_{\mathbf{g},\alpha\beta}$ - the grid voltage vector in the $\alpha\beta$ coordinate

$\mathbf{i}_{\mathbf{g},\alpha\beta}$ - the grid current vector in the $\alpha\beta$ coordinate

* - the complex conjugate

$\mathbf{i}_\mathbf{g}^*$ - the complex conjugate of grid current

ABSTRACT

Due to the clean energy imperatives and strong desire to reduce greenhouse gas emissions, electric vehicles (EVs) were introduced into the car market several decades ago. In 2016, electric cars hit a new record with over 750 thousand sales worldwide. China was the largest electric car market with more than 40% of all car sales in the world. With an increasing number of electric cars, private and publicly accessible charging infrastructure has also continued to grow. As most of the time these electric cars are parked in personal or public car parks. A car park with these parked electric vehicles can be regarded as a large energy storage system. These vehicle batteries can be used as energy storage devices to exchange the power between the grid and vehicles. With this idea, a new smart car park model is proposed, where the power flows among electrical vehicles, as well as between batteries and the main grid. Based on this model, an optimal charging/discharging scheme is developed to maximum the profits for the car park and reduce the cost for the car owners. The proposed smart electrical car park is able to buy or sell electricity in the form of active and/or reactive power, i.e. kWh and/or kVARh, from or to the main grid to improve the power quality. According to the current state of charge of the car battery bank, customer and grid demands, a control centre makes the decisions and sends the instructions for the specific charging/discharging mode to each charging station.

The model predictive control (MPC) method is distinguished for its several advantages: free of modulation, simple inclusion of system parameters, constraints and demands in the algorithm. With this MPC strategy, EV chargers are able to transmit the active and reactive power between the EV batteries and the power grid. When providing the reactive power from the EVs to the main grid, EV batteries can be regarded as static VAR compensators to improve the power quality. To improve the system performance, a modified MPC scheme is proposed for better performance. The modified MPC is based on the application of an optimal voltage vector chosen from an extended set of 20 modulated voltage vectors with a fixed

duty ratio. To solve the computational problem introduced by the increased voltage sets, a pre-selective algorithm is proposed for the MMPC method. Six voltage vectors are pre-selected from the 20 sectors. The conventional and proposed MPC methods are compared through numerical simulation and experimental test results via a two-stage two-level three-phase off-board charger. Better system performance can be achieved with the modified MPC method.

The conventional MPC method, however, produces a large overshoot/undershoot, a long settling time and a large steady state error under disturbances. To overcome these deficiencies, a sliding mode controller is employed to replace the PI controller in MPC. A model predictive sliding mode control (MPSMC) scheme is proposed to achieve better stability and dynamic performances. Since the control law and the controller are based on the system model, the proposed scheme can reduce the effects of unexpected disturbances, such as the output voltage demand and the resistive load variations. Numerical simulation and experimental test results are obtained via the proposed MPSMC method and compared with the results form the traditional MPC scheme.

For convenient integration into the power grid, the topology of an electric car park can be based on either AC bus or DC bus. The EV chargers can be controlled to achieve four-quadrant operation, delivering active and reactive power from or to the main grid. The system performance obtained from simulation tests with these two topologies are compared and discussed, including the cost, reliability, size, active and reactive power ripples, and current distortion, etc.

Chapter 1

INTRODUCTION

1.1 Significance and Background

A small-scale electric vehicle (EV) was first designed and developed in the 1800s. Due to the limitation of technologies in early last century, the performance of EVs was poor. In the modern time, new battery technologies, in particular, lithium-ion, which can provide higher power and energy density than other types of batteries, make EVs much better accepted by the market. As an environment-friendly and cost-effective substitute of the internal combustion engine (ICE) vehicles, EVs show many superiorities over the gasoline-powered cars, such as quiet operation, ease of driving, and independence to fossil fuels. Without emitting the green-house gasses, EVs are becoming more and more attractive and popular, especially to urban drivers.

By employing the grid-to-vehicle (G2V) technology and a high capacity battery, EVs can be recharged from the main grid [1]-[2]. With the vehicle-to-grid (V2G) and vehicle-to-vehicle (V2V) technologies, EVs can be regarded as energy storage devices which can provide battery power to the main grid or other electric equipments [3]-[4]. With large numbers of EVs parked, smart car parks could be regarded as large energy storage systems. These smart car parks located in office buildings and shopping malls have shown an enormous commercial potential to incorporate EV batteries into the power grid. Instead of being a burden or unexpected load to the power grid, EVs can function as active power compensators by charging/discharging energy from/to the grid.

Besides exchanging the active power with the grid, EVs have high capability in

providing the reactive power, working as static VAR compensators (SVCs) [5]. This operation is known as the vehicle-for-grid (V4G), in which the EVs can support the main grid by delivering the reactive power [6].

1.2 Research Objectives

With the increasing number of EVs on the market, it would be a good idea to make full use of these EV batteries. A smart electric car park, with huge numbers of EVs parking, can achieve bidirectional active power flow between the EVs and grid by V2G and G2V technologies. On the other hand, the reactive power can also be provided or absorbed by the car park to support the grid demand.

The objective of the research in this thesis is to build and analyse a smart car park model and develop effective control schemes of EV chargers based on model predictive control (MPC) method. This research objective can be broken down into three targets as follows:

i. Build a smart car park model and maximize the profit of the car park by an optimal charging/discharging scheme for the EVs;

ii. Develop the predictive control methods for the EV chargers to achieve bidirectional active and reactive power flow between the EV batteries and the main grid;

iii. Compare the smart car park systems with AC and DC buses with the MPC scheme.

1.3 Thesis Organization

This thesis is organised as follows:

- *Chapter 2* presents a literature review of EV charger topologies, charging levels, charging power rates, converter control methods, and wireless telecommunication technologies. The features of unidirectional and bidirectional, on-board and off-board EV chargers are analysed in this chapter. The modern digital control methods, such as the proportional integral (PI) control, direct power control (DPC), sliding mode control (SMC) and MPC, are briefly introduced and presented.

- In *Chapter 3*, a model of the smart car park system with an optimal charging/discharging method is designed. A real electricity price and vehicle parking distribution are considered in this model. This chapter shows that with the G2V, V2G and V2V technologies, the smart car park owner can get benefits from the electricity price gap between the EV drivers and the power grid.

- *Chapter 4* presents the basic MPC scheme for a three-phase two-level EV charger to work in the four-quadrant operations. The EV charger prediction model and cost function are built in this thesis research. The system controlled by the DPC method is used to compare with the MPC technique. A modified model predictive control (MMPC) with extended voltage space vectors is proposed. A laboratory scaled-down setup is developed to show and validate the dynamic and steady state performance obtained by the DPC, MPC, and MMPC methods.

- *Chapter 5* presents a model predictive sliding mode control (MPSMC) for a three-phase converter. This chapter illustrates that the MPSMC has substantial improvement upon the basic MPC. The proposed method has a faster dynamic and better steady state performance.

- In *Chapter 6*, the smart car park system with AC and DC bus topologies are compared. The features of two topologies, including the system reliability,

system performance, and grid current total harmonic distortion (THD), are compared and analysed.

- *Chapter 7* presents a brief summary of the thesis contents and the project contributions are given. Recommendation for the future work is given as well.

Chapter 2

LITERATURE REVIEW

2.1 Introduction

Due to the invention of the lead-acid battery by Gaston Plante, the first electric car was built in the United States in 1891 [7]. With further technological developments, an electric hybrid vehicle for the U.S. clean car incentive program was built in 1972. Because of the limitations in the battery technology, the program only lasted 5 years. After around 130 years since the first electric car was invented, the commercial production of electric vehicles (EVs) has now been realized. Tesla, Nissan, Chevy and Bavarian Motor Works are the top EV companies in the current electric car market.

Currently, EVs are attracting more and more attentions from the researchers due to their reduced fuel usage and greenhouse emissions. These environment-friendly EVs also have a higher energy efficiency around 60% compared to 20% for gas powered vehicles to convent energy into vehicle movement [8]. There was a big issue of EVs in the early stage that their driving distance was limited by the battery capacity. Recently, with the advanced technology of lithiumion battery, the driving range for a fully charged EV has been increased from around 60 $\sim$ 120 miles to 400 $\sim$ 500 miles [9]. Due to this improvement, EVs now take a significant place on the vehicle market and become popular among car drivers.

With the advanced grid-to-vehicle (G2V), vehicle-to-grid (V2G), vehicle-to-vehicle (V2V) and vehicle-for-grid (V4G) technologies, EVs can support the grid through ancillary services, such as load balance and reactive power support [10, 11]. When

a huge load is suddenly plugged in or out, a voltage deviation can occur, which is one of the key power quality concern for the grid [12]. Using the G2V and V2G technologies, EV batteries can be charged overnight and discharged in the daytime to smooth the load on power plants and avoid additional generator start-ups. This enables the system to improve the power quality rather than being a load burden on the power grid. Besides exchanging the active power with the grid, EVs can also provide reactive power to the power grid. Since the grid always demands a range of reactive power, this operation (V4G) can support the grid by improving the power factor and reducing the voltage deviation. Bidirectional power flows, power factor control and voltage deviation mitigation can be achieved by the infiltration of EVs.

2.2 Types of Electric Vehicles

Considering of the degree that electricity is used as the energy source, there are three main types for EVs: hybrid EVs (HEVs), plug-in hybrid EVs (PHEVS) and battery EVs (BEVs). HEVs are powered by both petrol and electricity. HEVs start off using the electric motor, and then the petrol engine cuts in as load or speed rises. The two motors are controlled by an internal computer which ensures the best economy for the driving conditions [13]. PHEVs are also powered by both petrol and electricity, except that PHEVs can recharge the battery through both regenerative braking and plugging-in to an external electrical charging outlet. PHEVs have an electric motor range of between 50-100 km before the petrol engine kicks in [14]. Due to the added weight and complexity, the electric motor range of a PHEV will generally be less than a BEV. BEVs are fully electric vehicles, meaning they are only powered by electricity and do not have a petrol engine, fuel tank, and exhaust pipe. BEVs are also known as plug-in EVs as they use an external electrical charging outlets to charge the batteries. BEVs can also recharge their batteries through regenerative braking. The range of a BEV is currently around 100-150 km, and

Table 2.1 :

Examples of EVs on the market

Model	Max charger capacity	Approximate range on full charge	Miles added per hour	EV types
Audi A3 e-tron	3.3 kW	240 km	11	PHEV
BMW i3	7.4 kW	190 km	25	EV
Tesla Model S	10/20 kW	500 km	29/58	EV
Tesla Model X	10/20 kW	465 km	29/58	EV
Cadillac ELR	3.3 kW	550 km	11	PHEV
Nissan Leaf	3.3/6.6 kW	151 km	11/22	EV
Ford Focus Electric	6.6 kW	122 km	22	EV

as most motorists drive around 35-70 km per day, the BEV can be a good option [14]. Table 2.1 lists the details of some PHEVs and EVs performance on the current market [15], [16].

2.3 Types and Topologies of EV Chargers

Based on the power ratings, there are three types of EV chargers: Levels 1, 2 and 3, as summarized in Table 2.2. Drivers can plug their EVs into convenient outlets at home or at the office with on-board chargers for Level 1, known as the slow charging. EV batteries can be charged during the daytime at the office station or overnight at home station. As the slowest charging method, it is likely to be employed in home or residential charging stations during overnight off-peak hours at low electricity prices. The infrastructure cost is about USD500 - USD880 [17]. The primary method used for private and public equipment is Level 2 charging, which is much faster than Level 1. Level 2 requires a 208 or 240 V outlet. It needs some

Table 2.2 :

EV charger power levels

	Level 1	Level 2	Level 3 (Fast charging)
Voltage	120 V	208 or 240 V	200 or 450 V
Current type	AC	AC	DC
Useful Power	1.4 kW	7.2 kW	50 kW
Maximum output	1.9 kW	19.2 kW	150 kW
Charging time	4-46 hours	1-6 hours	0.4-1 hour
Charging topology	On-board	On-board	Off-board
	1-phase	1 or 3-phase	3-phase
Charging location	Home or office	Private or public outlets	Commercial station

special equipment and a standardized vehicle-to-charger connection. This leads to an increase in its installation cost within the range between USD1,000 and USD3,000 [18]. Single-phase charger topologies are usually applied in Levels 1 and 2. Level 3 (DC fast) charging are intended for commercial applications, with three-phase off-board solutions normally. Due to some dedicated equipment, the infrastructure cost for this power level charger is approximately between USD10,000 and USD20,000. Levels 2 and 3 are usually used for public charging and installed in parking lots, shopping centres, hotels, and restaurants, etc.

EV battery chargers can be classified into four groups based on the designated power flow direction, namely, unidirectional on-board chargers, unidirectional off-board chargers, bi-directional on-board chargers, and bi-directional off-board chargers [17]. The P-Q coordinate in Fig. 2.1 describes the available operation regions for EV battery chargers. The positive axes of P and Q indicate the active and reactive power flow from the grid to the battery, respectively. According to the power trans-

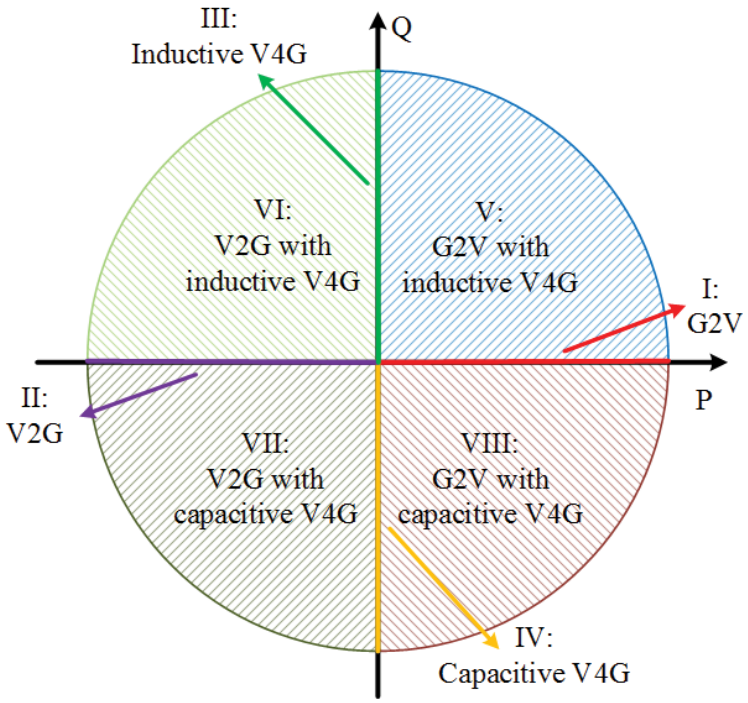

Figure 2.1 : Different working operation located in the PQ axis

mission direction, the PQ plane can be divided into eight operation modes. The axes of the PQ frame, defined as Modes I $\sim$ IV, represent the pure G2V, V2G, inductive V4G and capacitive V4G operations, respectively. Working under these operations, the active or reactive power is delivered separately between the EVs and the grid. The system can be controlled at a unity power factor operation as well. The rest of the four quadrants shows the V2G or G2V operation along with capacitive or inductive V4G operation. During these working states, EVs can exchange both active and reactive power with the grid. EV batteries can smooth the electricity load by plugging in or out of the charging stations, by providing or consuming the reactive power to improve the power quality.

2.3.1 Unidirectional chargers

Unidirectional chargers operate along the positive P-axis of the P-Q coordinate (Modes I, V and VIII), as shown in Fig 2.1. The active power flow is available only

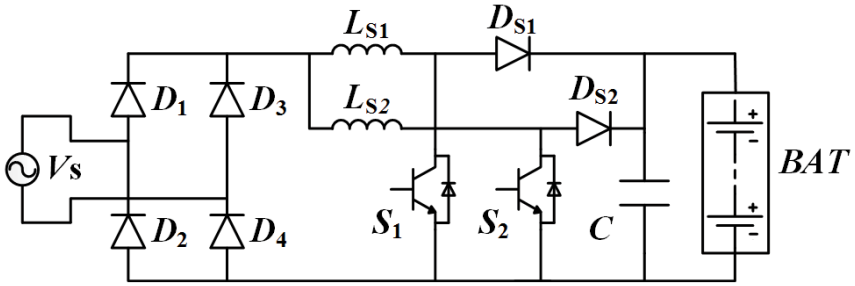

(a) Interleaved unidirectional charger circuit.

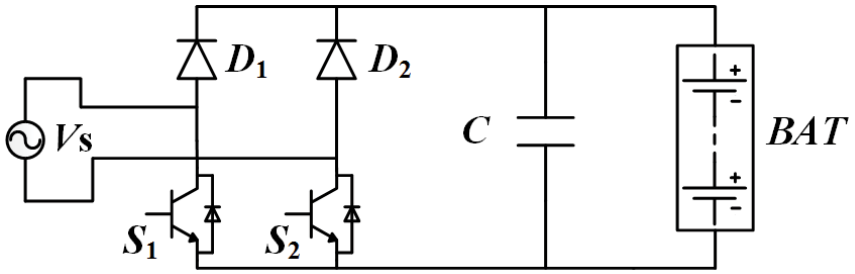

(b) Symmetrical boost rectifier topology.

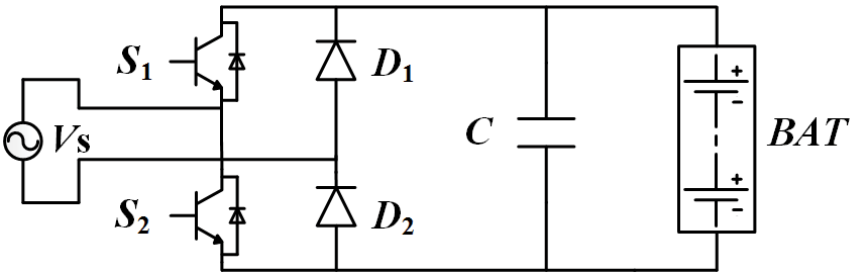

(c) Asymmetrical boost rectifier topology.

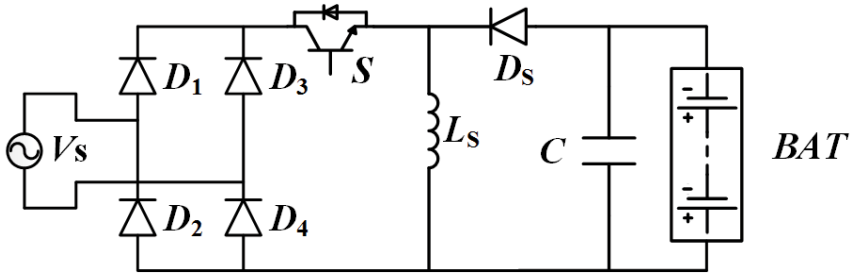

(d) Inverting buck/boost PFC rectifier circuit.

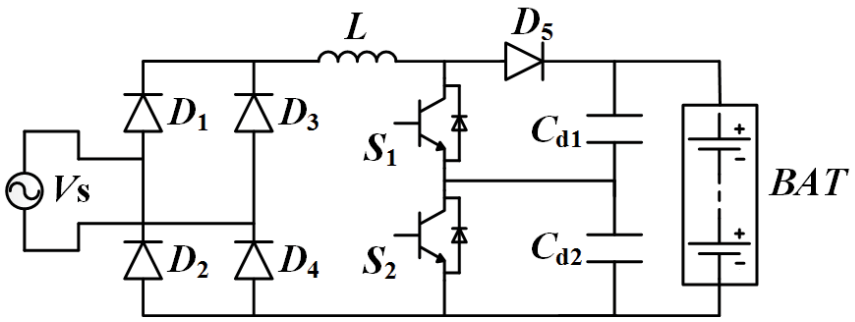

(e) Unidirectional multilevel charger topology.

Figure 2.2 : Unidirectional charger structures.

from the grid to the vehicle. Meanwhile, reactive power is possible to be transmitted during the battery charging process. However, this will introduce undesirable low-frequency current harmonics [21]. Therefore, these chargers are always preferable to operate close to unity power factor in Mode I.

Various topologies, such as half-bridge, full-bridge and multi-level converters, have been studied for both single-phase and three-phase unidirectional chargers. The power factor correction (PFC) boost converter, a conventional topology, is used in low-power applications [21]. Considering the costs, sizes and component stresses of chargers, circuits of different topologies are applied in diverse application fields, such as the interleaved AC/DC boost converter, inverting or positive buck/boost PFC converter and the multilevel converter [17, 22], as presented in Fig 2.2.

2.3.2 Bidirectional chargers

To make full use of EV batteries, smart chargers with V2G technology has been proposed and studied extensively. With the G2V and V2G technologies, the active power can be transfered between the EV batteries and the grid. They are controlled to operate in the P-axis of the PQ plane for unity power factor. Apart from transmitting the active power in V2G/G2V operations, reactive power compensation

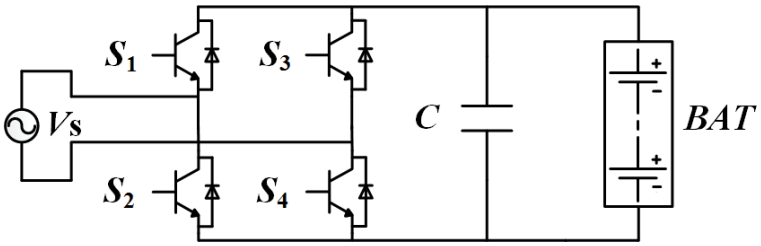

(a) Single-phase bidirectional charger topology.

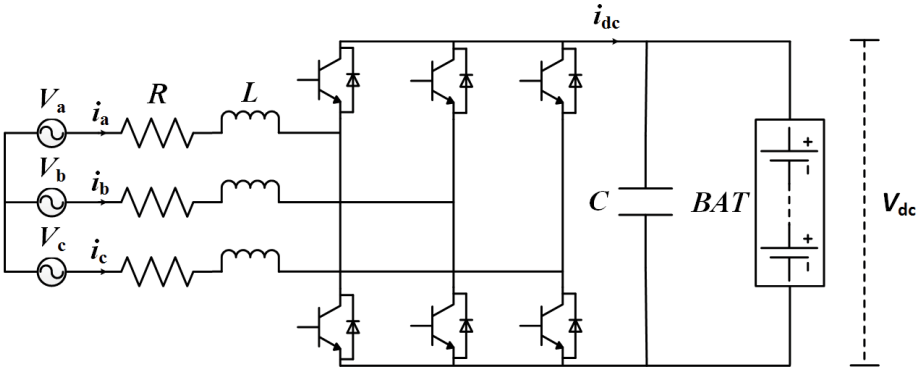

(b) Three-phase bidirectional charger topology.

Figure 2.3 : Bidirectional charger structures.

(inductive or capacitive) provided by the capacitor can improve the power quality of the utility grid. During the V4G operation, the EV batteries can be regarded as capacitor banks, and static compensators, etc. Note that it is undesirable for the battery state of charge (SOC) and its lifetime to be affected during the reactive power operation [23]. However, the lifetime of DC-link capacitors will be reduced due to the increasing charging-discharging cycles.

Fig. 2.3 shows the typical circuits of (a) a single-phase and (b) a three-phase bidirectional battery chargers, respectively. Most EV chargers are able to be plugged into a home or office outlet for Level 1 (slow charging) or Level 2 [17]. They are usually designed for on-board chargers for private or public facilities with single-phase topology. For commercial applications, such as shopping mall and official car parking spots, three-phase structures are normally applied with Level 2 or 3

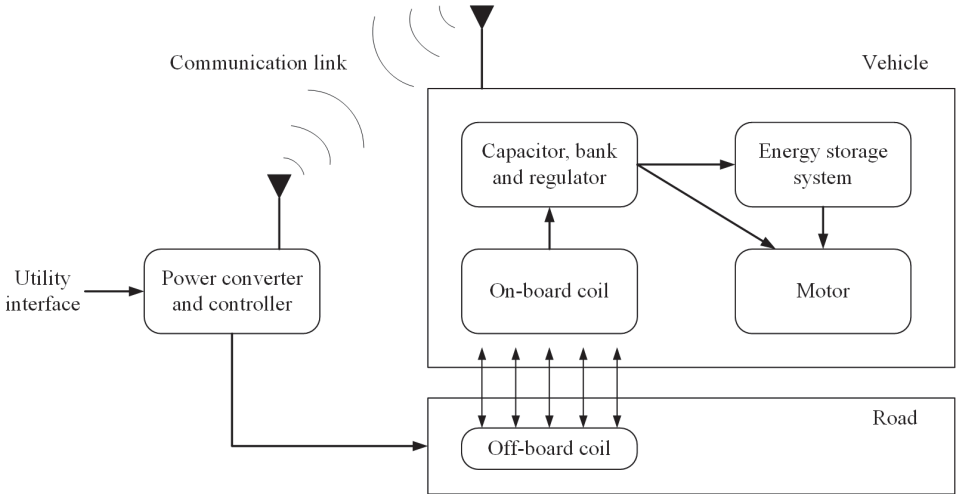

Figure 2.4 : Main components of a wireless charging system

chargers installed for off-board charging. Therefore, a three-phase circuit is selected and studied for the smart car park in this thesis.

2.3.3 Wireless EV chargers

Wireless power transfer, as an emerging technology, has been used in EV chargers to transfer power over large air gaps recently due to its convenience [19]. Generally, a wireless charging system includes a utility interface, an off-board power converter with controller, off-board coils, on-board power electronics and communication interface between the road-side and vehicle-side radios, as shown in Fig. 2.4. The off-board power converter consists of an AC/DC power factor correction converter and a high frequency DC/AC converter. Instead of physical connection or a regulator transformer, the wireless charger transfers power via a magnetic field [20]. There are some challenges for the wireless EV chargers, such as safety considerations, acceptable power transfer efficiency at high transfer power range, increasing power level, and misalignment tolerance.

2.4 Control Strategies and Methods for Chargers

Various of control strategies have been studied to control the power converters and drives in recent years. Mithat and Metin used the proportional integral (PI) controllers for both the single-phase on-board and three-phase off-board bidirectional EV chargers [23, 24]. Two outer PI loops are utilized to track reference active and reactive power commands. In [25]-[27], hysteresis and linear controls with pulse width modulation (PWM) are the most established. Nevertheless, due to the presence of faster and more powerful microprocessors, more sophisticated and effective control methods have been employed in recent decades, such as the fuzzy logic control, sliding mode control and predictive control. Specifically, the fuzzy logic is more suitable for applications where the controlled system or some of its parameters cannot be known. Based on the reaching condition, existing condition and stability condition, the switching nature of the power converters is considered in the sliding model control. Besides these control schemes, some others, such as neural networks and neuro-fuzzy, have been analysed in the literature [28].

Among these control strategies, the predictive control scheme shows great advantages over the others in terms of controlling the power converters. It is conceptually simple to handle multiple and non-linear variables and constraints, and practically convenient to implement [28]. Compared with the classical control schemes, the predictive control strategy needs a high amount of calculation, which can be readily solved by using fast microprocessors today. Generally, the quality of the controller depends on the quality of the model. The fundamental principle of the predictive control is to use the system model to predict the future behaviour of the controlled variables. The predictive control can be classified into four types: the deadbeat control, the hysteresis-based predictive control, the trajectory-based predictive control, and the MPC method. The MPC method can be based on either continuous or

finite control set. The MPC with continuous control set needs a modulator during operation, and a fixed switching frequency can be obtained. On the other hand, the MPC with finite control set is independent of the modulator. The switching frequency is variable and the algorithm is low in complexity. For both MPC schemes, constraints can be included directly.

2.4.1 Direct power control

Derived from the original direct torque control (DTC) used in controlling AC motors, DPC is aimed at regulating the instantaneous active and reactive power of the converter system directly [29]-[31]. The main principle of this scheme is to select a control vector from a switching table based on the errors between the expected and estimated values of active and reactive power as well as the angular position of the estimated voltage source vector [32]. Therefore, no internal current control loops and PWM modulator are needed in DPC, which contributes to its excellent transient performance, robustness and simplicity [33]-[35].

Fig. 2.5 illustrates a block diagram of the conventional DPC strategy used in the AC/DC converter. The reference value of active power, P_{ref}, is obtained from a PI controller used as a DC voltage regulator, while the reactive power reference, Q_{ref}, is always set to be zero to ensure the unity power factor operation. The estimations of active and reactive power, P and Q, are calculated by voltages and currents on the AC side, as well as the position of power source voltage S, which is located in an $\alpha\beta$ plane of 12 sectors. The tracking errors between the measured and expected values of active and reactive power, denoted as d_P and d_Q, are generated by two fixed bandwidth hysteresis comparators. Then, according to the tracking errors d_P and d_Q, and the angular position of the estimated voltage source vector, the converter switching states can be selected from a switching table in each sampling period.

However, there are two significant challenges for this DPC scheme. One is that

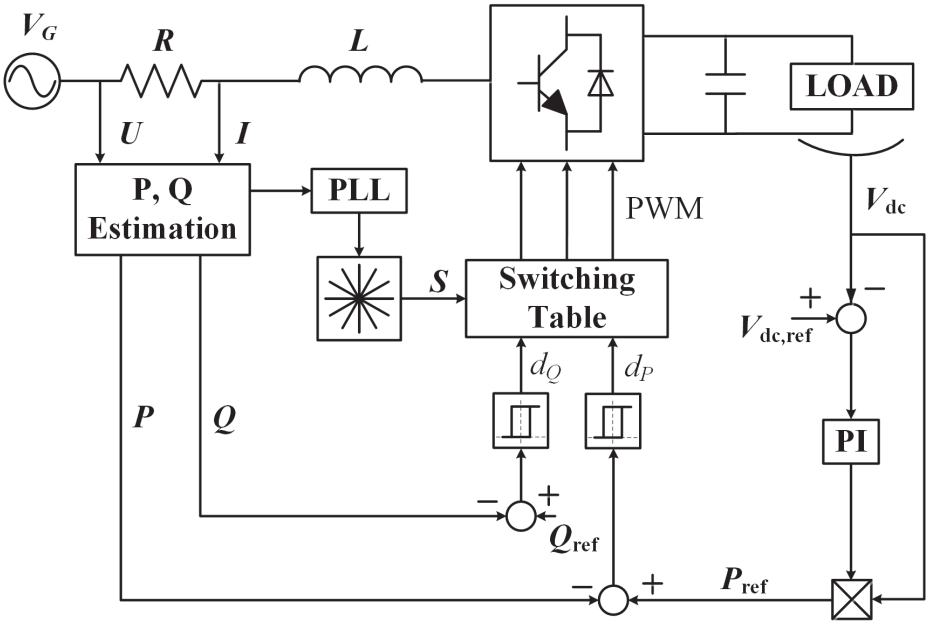

Figure 2.5 : Block diagram of conventional DPC.

the variable switching frequency mainly depends on the sampling frequency, system parameters, reference values of active and reactive power and the converter switching states. This will lead to a broadband harmonic spectrum in the AC line currents. Another challenge is that in order to achieve perfect tracking of a time varying signal, high sampling frequencies need to be applied. As a result, they are very sensitive to current ripples. Therefore, variable switching frequency, large power ripples and high switching frequencies hinder the application of this control method.

2.4.2 Sliding mode direct power control

As an effective robustness control scheme, sliding mode control (SMC) is known for its high dynamic response and robustness against parameter variations and disturbances [36]. It is a nonlinear control method using a designed sliding surface as a reference hyper plane [37]. A control law is used to ensure the controlled system state variables trajectories are directed onto this sliding surface or towards the expected equilibrium within a finite time [38]. Since the sliding surface and control

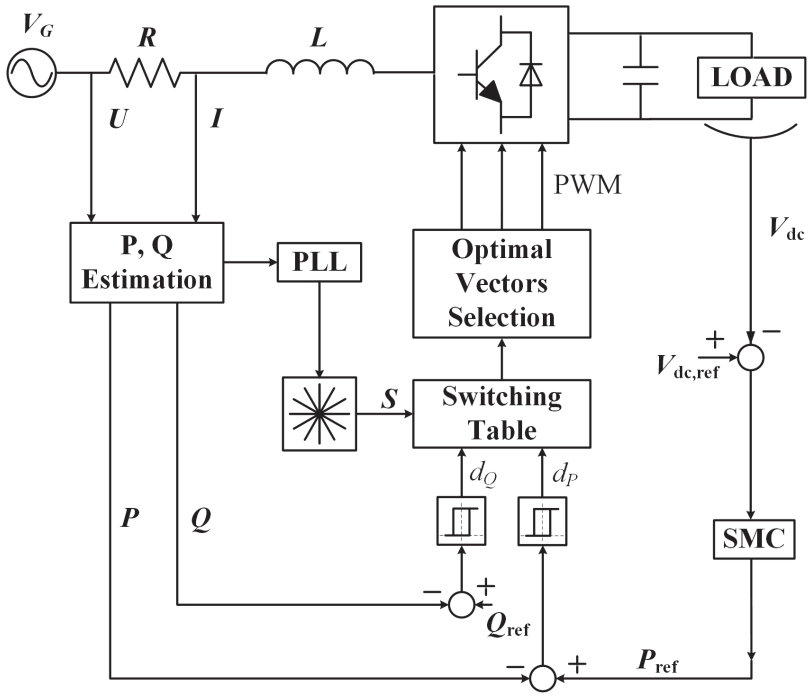

Figure 2.6 : Block diagram of SMC.

law are based on system model, when the parameters or load change, the controller can work effectively with the updated system and new requirements.

The SMC strategy of AC/DC conversion is illustrated in Fig. 2.6. The error between the measured and referenced values of the voltage on the DC side, denoted as V_{dc} and $V_{dc,ref}$, is controlled by the SMC to be zero. The reference value of active power P_{ref} can be generated by this SMC controller. Compared with estimated values of active and reactive power, the two errors are generated by two hysteresis comparators and sent to the switching table. An optimal vector will be selected to determine the switching states for the next sample time period.

In order to guarantee the stability and effectiveness of the system, the designed sliding surface and control law are needed to meet three conditions, namely, the reaching condition, existence condition and stability condition [39]. The reaching condition is to ensure that the system reaching point will finally reach the sliding

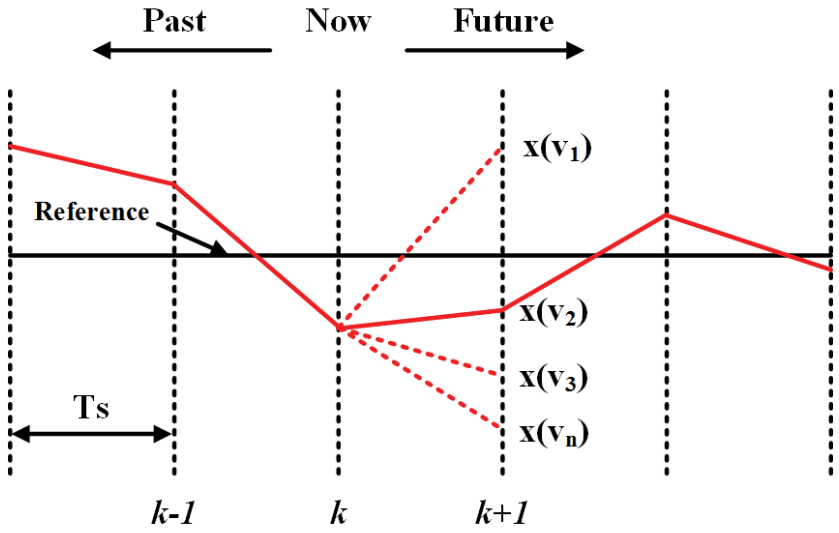

Figure 2.7 : Working principle of MPC.

surface no matter where its initial position is in the state space. The existence condition ensures the state trajectory of reaching points in the neighbourhood field of the switching surface is capable to reach the sliding surface during a finite period [40]. The stability condition of the sliding mode can be derived by applying the Lyapunov stability analysis [38].

2.4.3 Model predictive direct power control

The main principle of MPC is to build a predictive system model to predict the behaviour of system variables over an N-step time horizon [41, 42]. The system predictive model can be expressed as a discrete-time state-space model. The working principle of MPC is shown in Fig. 2.7 for a one-time step horizon. A variable x is supposed to reach the reference value. The state-space model is used to predict all possible control variables ($x(v_1)$, $x(v_2)$, $x(v_3)$, $\cdots$, $x(v_n)$) [43, 44]. A cost function J is applied to indicate the error between the expected and measured values of the control variables according to its control objectives [45, 46]. The aim of MPC is to choose an optimal switching state closest to the reference value for the next sample

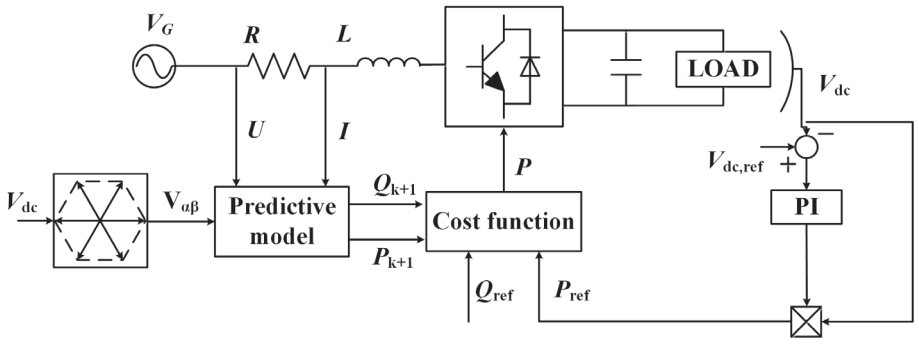

Figure 2.8 : Block diagram of MPC.

period (T_s). This selected switching state can minimize the cost function J.

Fig. 2.8 shows a block diagram of the MPC scheme used in an AC/DC converter over one step prediction [47]. The objective of this system is to control the active and reactive power. Hence, the referenced and measured active and reactive powers are processed in the cost function to select a DC voltage vector as well as a switching state. According to the space voltage vector pulse width modulation (SVPWM), the output voltage of the converter V_{dc} can be controlled to eight vectors in two-phase stationary $\alpha\beta$ coordinate based on eight possible switching states. Based on the state-space model, there are eight current vectors determined by the voltage vectors. Thus, eight vectors of active and reactive powers can be achieved and used in the cost function which has also eight cases [48]. Among these cost function values, a minimum one is selected for the next sampling period. Once a minimum cost function is selected, an active power and a reactive power can be determined as well as the current vector. According to the selected current vector, a switching state can be found based on the relevant voltage vector. Finally, the active and reactive powers can be controlled to the reference values, respectively.

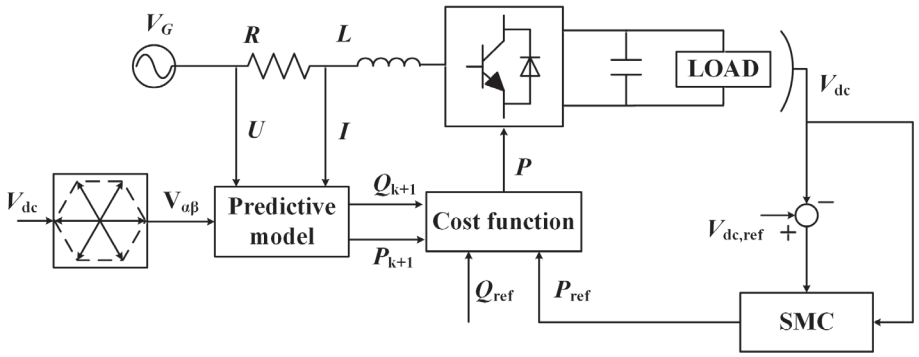

Figure 2.9 : Block diagram of MPSMC.

2.4.4 Model predictive sliding mode control

In the conventional model predictive control method, a proportional integral (PI) controller is used to generate the active power reference, as shown in Fig. 2.8. This traditional model predictive scheme, however, produces a large overshoot/undershoot, a long settling time and a large steady state error under disturbances. The PI coefficients are difficult to be tuned to a perfect set manually. In addition, when the system parameters and demands change, it is impossible to apply a fixed pair of the PI coefficients to suit all operation conditions. To overcome these deficiencies, a sliding mode controller is employed to replace the PI controller in [49]. Since the control law and the controller are designed based on the system model, the model predictive sliding mode control (MPSMC) method can reduce the effects of unexpected disturbances, such as the variations of output voltage demand and load resistance. A control block of the model predictive sliding mode control scheme is presented in Fig. 2.9.

2.5 Communication Methods between EVs and Centre Controller

In recent years, wireless telecommunications have been widely used in the smart micro grid for control data and signal transmission. Among existing technologies, there are three typical ones: wireless local area networks (WiFi-802.11n), wireless personal area networks (ZigBee), and wireless metropolitan area networks (WiMAX) [50].

2.5.1 Wi-Fi

The Wi-Fi technology is based on IEEE 802.11 and has been applied in the following types of network: 802.11b, 802.11a, 802.11g and 802.11n. The first 802.11b network was able to transfer data at up to 11 megabits per second (Mbps). Then followed shortly thereafter by 802.11a and 802.11g, the maximum speed of them being 54Mbps with throughput speeds approximately 25 Mbps. Due to the requirement of consumers and businesses seeking higher bandwidth, the network 802.11g was quickly proposed and accepted [51]. Nowadays, the network 802.11n leads a new Wi-Fi speed standard which is capable of a bandwidth of around 108 Mbps. Since it will be a new industry standard, n-compliant devices will be interoperable. The comparison of the primary IEEE 8-2.11 specifications is summarized in Table 2.3.

2.5.2 ZigBee

A modern technology which empowers the wireless personal area networks (WPAN) is ZigBee. It is a specification for a suite of high-level communication protocols used to create personal area networks built from small, low-power digital radios based on an IEEE 802.15.4 standard [51, 52]. As a global control network standard, it has the following characteristics:

Table 2.3 :

Comparison of the primary IEEE 8-2.11 specifications

	802.11a	802.11b	802.11g	802.11n
Maximum data rate	54 Mbps	11 Mbps	54 Mbps	600 Mbps
Modulation	OFDM	DSSS or CCK	DSSS or CCK or OFDM	DSSS or CCK or OFDM
RF band	5 GHz	2.4 GHz	2.4 GHz	2.4 GHz or 5 GHz
Number of spatial streams	1	1	1	1, 2, 3 or 4
Channel width	20 MHz	20 MHz	20 MHz	20 MHz or 40 MHz

- Low electricity consumption with its battery life ranging from months to years;
- The typical range around 70-100 m;
- Low cost in device, installation and maintenance. This means that the batteries used in ZigBee devices can last up to years using primary cells (low cost) without any chargers (low cost and easy installation). Due to the simplicity of ZigBee, low maintenance is needed for the inherent configuration and redundancy of network devices;
- Maximum data rates allowed for each of the frequency bands are fixed as 250 kbps @2.4 GHz, 40 kbps @ 915 MHz, and 20 kbps @ 868 MHz [51].

2.5.3 WiMAX

The IEEE approved the 802.16 standard in June 2004, which is known as WiMAX [53]. It is able to be employed for wireless networking like WiFi. WiMAX is capable

Table 2.4 :

Comparison of Emerging Wireless Technologies

Technology	Wi-Fi	ZigBee	WiMAX
Application	Wireless LAN Internet	Sensor network	Metro area broadband Internet connectivity
Typical	100 m	70-100 m	50 km
Frequency range	2.4 GHz	2.4 GHz	2-11 GHz
Data rate	108-600 Mbps	250 Kbps	75 Mbps
Modulation	DSSS	DSSS	QAM
Network	IP & P2P	Mesh	IP
IT network connectivity	Yes	No	Yes
Access protocol	CSMS/CA	CSMS/CA	Request/Grant
Key advantages	Wider bandwidth flexibility	Cost, power	Throughput coverage

of higher data rates over longer distances and effective utilization of bandwidth. Also, interference can be reduced to a minimum value.

2.5.4 Comparison of wireless technology

Table 2.4 summaries the main characteristics of these technologies that enable smart grid area communication. In this thesis, Wi-Fi is selected as the communication technology in the smart car park due to its typical range of 100 m and wider bandwidth, which is low cost and suitable. The control centre communicates with the power grid, charging stations and energy storage devices via Wi-Fi to achieve power transmission between EVs and the control centre.

2.6 Concluding Remarks

In this chapter, a literature survey is presented on different types of EVs on the current market, types and topologies of the EV battery chargers and describe the major control methods available today. DPC, SMC, MPC and MPSMC methods are widely studied and applied in power electronic converters, which are detailed in the following chapters. The major communication technologies, including Wi-Fi, ZigBee and WiMAX, for smart micro grid applications, are compared in Table 2.4. As it performs better than other communication technologies, such as, ZigBee and WiMAX, Wi-Fi is selected for the smart car parks due to its suitable typical range and low cost. EV batteries, charging stations and the control centre can readily interface with each other through Wi-Fi.

Chapter 3

OPTIMAL CHARGING/DISCHARGING METHOD FOR SMART ELECTRIC CAR PARKS

3.1 Introduction

Due to the fast depletion of fossil fuels and large quantities of greenhouse gas emissions, efficient and clean electrical vehilces (EVs) have drawn great attention recently [54, 55]. No doubt, they will be widely used in the near future [56, 57]. Furthermore, since the battery banks of EVs consume huge amounts of electricity from the power grid, new vehicele-to-grid (V2G) and vehicle-to-vehicle (V2V) technologies are being developed to take advantage of the energy stored in these rechargeable batteries [21], [58]-[60], and help balance the power grid between the demand and supply needs, and aid in the delivery of the energy to EVs [3, 61, 62].

Compared with the EVs used in public transportation, personal EVs are much greater in number, but are employed for only around 4% of the day for transport [63]-[65]. Since they are parked for about 96% of the time, it would be a good idea to develop their energy storage capability to provide a secondary service in the electricity market [66]-[69]. A smart electrical car park, with a large number of parked EVs, can be regarded as a large capacity energy storage unit. Taking advantage of the new V2G technology and an appropriate economic strategy, this car park is able to yield profits by providing effective services to the EV customers and the electricity supplier [70]-[73]. Inspired by this idea, we propose an approach to using a smart electrical car park to enable the personal EVs to participate in the

energy market.

In the recent literature of EVs, in which the EV batteries are considerd as controllable parts in the power system. Numerous papers pay attention to optimizing EVs charging and discharging modes, so as to participate in ancillary services in the smart grid [74]. Some works aim to minimize the expense of EVs to the owner or to reduce the total cost of the aggregator separately. The works of [3], [75] and [76] indicate that the proposed charging strategies of using the realistic analysis of EVs' driving profiles can cut down the charging costs for EV owners. In 2012, Nguyen et al. [54] proposed a smart charging and discharging method for multiple plug-in hybrid EVs (PHEVs) in a building car park to optimize the energy consumption for this building. An energy cost-sharing model and a distributed algorithm were presented to minimize the peak load and the total energy cost at the same time.

With the bidirectional chargers, the EV batteries can exchange the active power with the utility grid in grid-to-vehicle (G2V) and vehicle-to-grid (V2G) operations. The EV batteries can also meet the reactive power command from the grid, which is known as the V4G operation. In this operation mode, EV batteries function as static VAR compensators (SVCs), and capacitor banks, etc. In this chapter, an optimal charging/discharging method is proposed to enable the smart car park system to benefit from the electricity price gap between the grid and the EV customers, and to support the grid with the reactive power.

3.2 System Model

In this section, a smart electrical car park model is introduced. As shown in Fig. 3.1, this smart electrical car park system is composed of numerous smart charging stations, a central controller and energy storage devices. The smart charging stations have touch screen panels to interface with the customers, allowing the customers to input their demands and special needs. These touch panels are connected to a con-

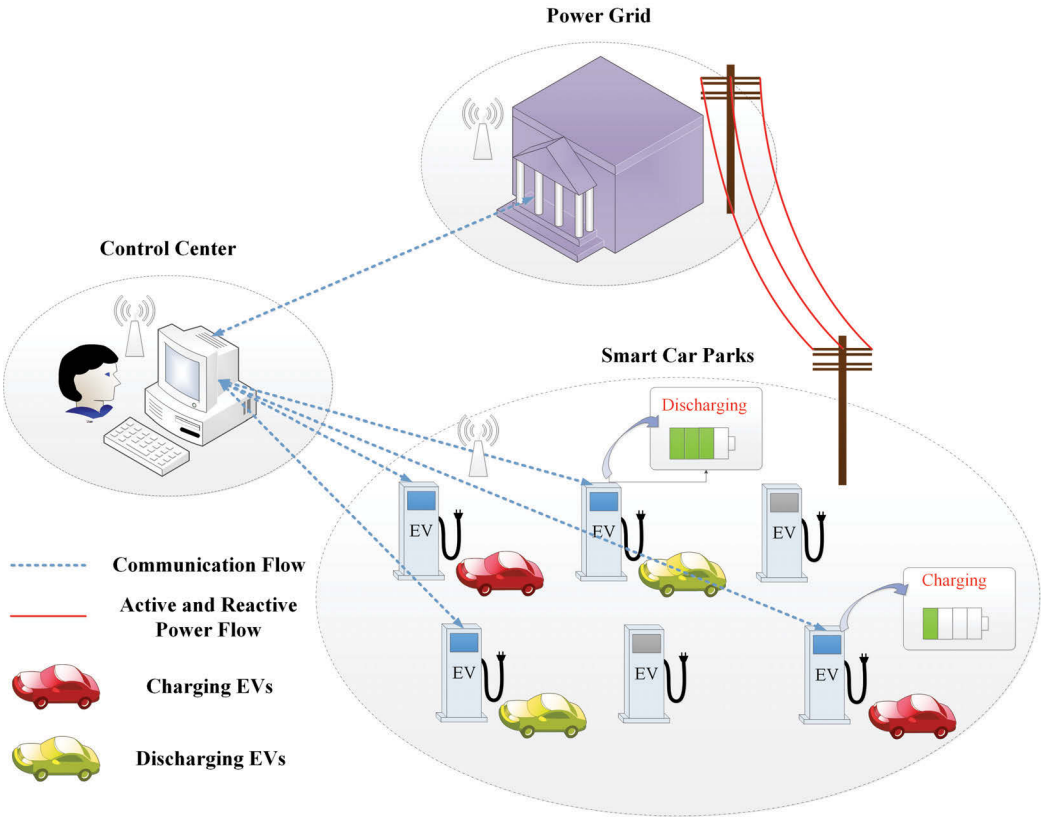

Figure 3.1 : Framework of the smart car park system.

trol centre via either cable or Wi-Fi [70]. The central controller collects the basic information from the main grid and EVs. The EV information includes battery capacity characteristics (i.e. the rated capacity, available capacity, voltages, expected charging and discharging currents), the initial SOC the final SOC, and the parking time (arrival and departure time), etc. The charging rates of EVs obtained from the charging scheme are sent to the chargers by the controller at every time slot. With the G2V and V2G technologies, EV batteries can exchange the active power with the main grid. However, the active power commands from the EV batteries and the utility grid may be different at times. Therefore, energy storage devices, such as battery and super-capacitor banks, are used to compensate for the power difference between the grid and the EV batteries within its capacity. It is of great assistance to keep the balance of the active power for the grid [23].

Apart from delivering the active power, this car park can supply the reactive power to support the grid in the V4G operation. During this operation, the EV batteries function as SVCs. It is important to note that the lifetime of EV batteries could not be shorten by the reactive power operation [24]. Other components, e.g. the DC-link capacitors, might be affected due to the increased number of charging-discharging cycles.

This kind of smart electrical car park can be located in office buildings, shopping malls, and residential communities in the future. According to the charging time in the report [77], 30 minutes is the minimum charging period for EVs parked in an office, home, and public and commercial parking lots. Therefore, in this thesis, the time slot (Δt) is set as 30 minutes. Note, however, that the time slot can be adjusted according to the requirements of different types of smart car parks.

Based on the designed time slot, the working time of smart electrical car parks is divided into several control periods. A single integer number between 0 and 24 is used to represent the time. For example, if the car park opens from 7 A.M. to 9 P.M., it is divided into 28 time blocks (N = 28) with each time block equal to 30 minutes. For easy reference, all the major notations are listed in Table 3.1.

3.2.1 Range of charging/discharging powers

In order to avoid overcharging or over-discharging the EV batteries, the charging power constraint for each EV should be considered before participating in the G2V and V2G processes. Since the charging rate varies depending on the types and conditions of EV batteries, EVs are divided into several categories according to the initial SOC, the final SOC, the charging type and the parking time. The information can be set by the customers through the touch screen panels.

Table 3.1 :

Major notations for variables used in this chapter.

Symbol	Variable
m	The mth EV
M	Total number of EVs
n	The nth period
N	Total periods
N_m	Total parking periods of the mth EV
E_m^n	Energy of the mth EV in the nth period (kWh)
E_m	Current stored energy of the mth EV (kWh)
$E_{m,c}^n$	Charging energy of the mth EV (kWh)
$E_{m,d}^n$	Discharging energy of the mth EV (kWh)
C_m	Battery capacity of the mth EV (kWh)
$SOC_{m,fin}$	Final SOC of the mth EV (%)
$SOC_{m,ini}$	Initial SOC of the mth EV (%)
p_m^n	Charging/discharging power of the mth EV in the nth period (kW)
$p_{m,c,max}$	Maximum charging power of the mth EV (kW)
$p_{m,d,max}$	Maximum discharging power of the mth EV (kW)

A parameter L is introduced to represent the charging type, defined as

$$L = \begin{cases} 1, & \text{this EV can only be charged,} \\ 0, & \text{this EV can be charged and discharged,} \\ -1, & \text{this EV can only be discharged.} \end{cases} \tag{3.1}$$

Some of the EVs only park for a short time, and thus, the priority objective is to meet the demand of customers rather than to charge more economically. In order to solve this problem, the maximum idle parking time for the mth EV $t_{m,p,max}$ is employed, which is calculated by

$$t_{m,p,max} = t_{m,p} - \frac{E_{m,need}}{p_{m,max}}, \tag{3.2}$$

where $t_{m,p}$ is the parking time, $E_{m,need}$ the needed charging/discharging energy, and $p_{m,max}$ the maximum charging/discharging power, for the mth EV. If the maximum idle parking time $t_{m,p,max}$ is less than one time slot Δt, the charging or discharging rate is set to the maximum value.

Finally, according to the above analysis, the charging power range of EVs is summarized in Table 3.2.

3.2.2 Electricity price

The hourly electricity price is a function of time, denoted as $f(t)$. Specifically, the hourly electricity prices in NSW, Australia, during one month (January 1 $\sim$ 31, 2015) were obtained from the Australian Energy Market Operator (AEMO) [78], which is responsible for the National Electricity Market of south-eastern Australia. The average hourly electricity prices over a month, used for simulation during the car park opening hours from 7 A.M. to 10 P.M., are presented in Fig. 3.2. It is used to calculate the electricity fee for the EV drivers and the car park owner.

The car park owner purchases the electricity from the grid at a wholesale rate, as well as selling it to the grid [5]. Meanwhile, the EV customers buy or sell it at

Table 3.2 :

Range of charging/discharging power.

SOC demand	Type	Charging power range	
		$t_{m,p,max} \leq \Delta t$	$t_{m,p,max} > \Delta t$
$SOC_{m,ini} < SOC_{m,fin}$	L=1	$p_m = p_{m,c,max}$	$p_m \in [0, p_{m,c,max}]$
	L=0	$p_m = p_{m,c,max}$	$p_m \in [-p_{m,d,max}, p_{m,c,max}]$
	L=-1	—	—
$SOC_{m,ini} = SOC_{m,fin}$	L=1	$p_m = 0$	$p_m = 0$
	L=0	$p_m = 0$	$p_m \in [-p_{m,d,max}, p_{m,c,max}]$
	L=-1	$p_m = 0$	$p_m = 0$
$SOC_{m,ini} > SOC_{m,fin}$	L=1	—	—
	L=0	$p_m = -p_{m,d,max}$	$p_m \in [-p_{m,d,max}, p_{m,c,max}]$
	L=-1	$p_m = -p_{m,d,max}$	$p_m \in [-p_{m,d,max}, 0]$

a general price as individuals. Therefore, four price-coefficients (δ_1, δ_2, δ_3 and δ_4), are introduced to describe the prices for EV customers and car park owners buying and selling electricity, respectively. The prices of EV customers and car park owners charging and discharging electricity can be formulated as

$$price(t) = \delta_k \times f(t), \quad k = 1, 2, 3, 4, \tag{3.3}$$

where $k = 1$ means EV customers take electricity from the grid (i.e. charging their EVs), and δ_1 is equal to 1, as the EVs act as individual customers; $k = 2$ means EV customers discharge electricity to the grid; $k = 3$ or 4 means the car park charges or discharges electricity, respectively. Normally, δ_3 is less than or equal to δ_1 since the car park buys electricity at a wholesale price. δ_2 is less than or equal to δ_4 because the car park has the ability to sell a large amount of electricity to the grid according to its demands, while an EV customer just sells a small amount of electricity to the car park as an individual at random periods of time.

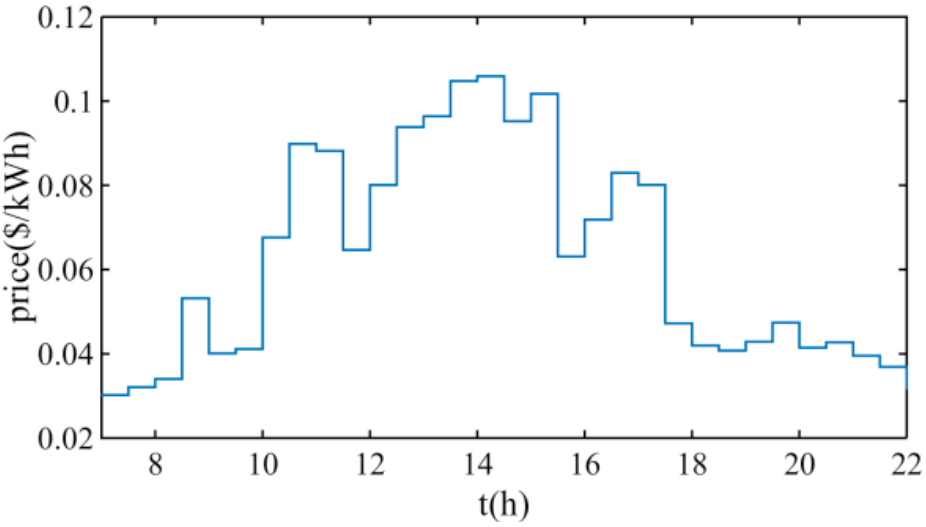

Figure 3.2 : Average hourly prices of electricity in NSW.

3.2.3 Grid demand

Another benefit for this smart electrical car park is that it can provide the stored energy to the grid during the peak hours and behaves as a load during the off-peak hours.

Fig. 3.3 exemplifies the relationship between the total electricity demand and the average regional reference price during one day, which is also obtained from AEMO [78]. It can be observed that the electricity price is high when the demand is increasing, and vice versa. Therefore, EVs can discharge energy to the main grid during the periods of high demands (such as 8 am $\sim$ 0 am), which can relieve the pressure on the grid. On the other hand, more EVs can be connected to the grid to be charged during the off-peak hours (such as 0 am $\sim$ 8 am).

3.2.4 Profits of smart electric car parks

The profit of a smart electrical car park is composed of two parts, as depicted in Fig. 3.4. One is the electricity price gap gained by exchanging the active power between the EVs and the grid. Another one is the income by working as a static

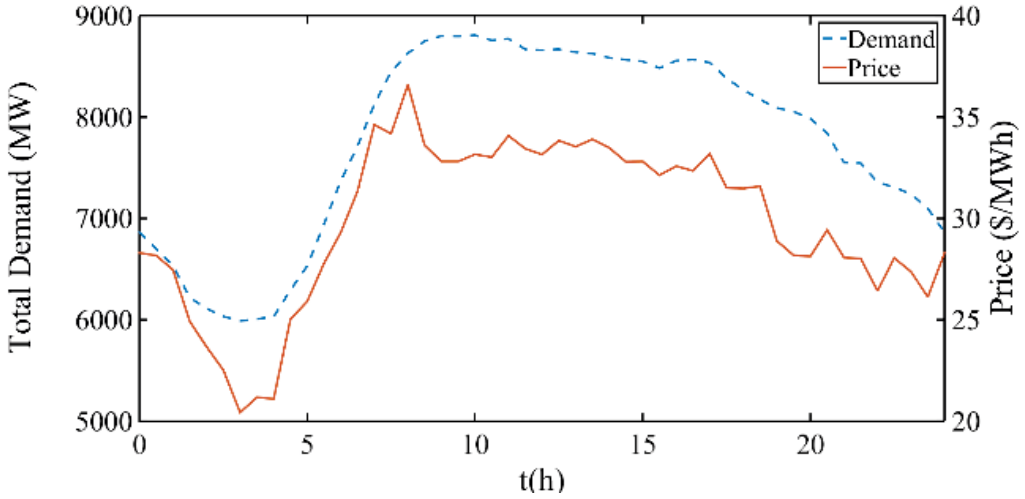

Figure 3.3 : Electricity demand and average regional reference price.

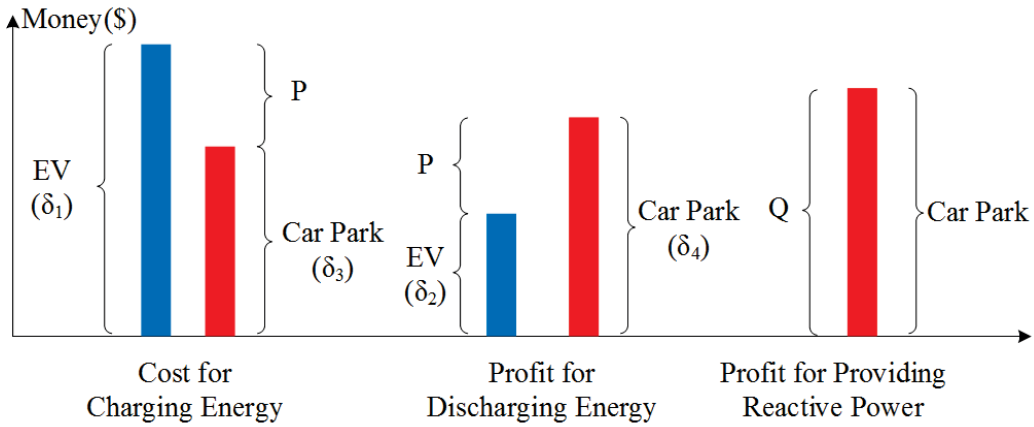

Figure 3.4 : Main profits of smart electrical car parks.

var compensator to provide the reactive power. The profit of exchanging the active power can be divided into two subparts: the charging profit and the discharging profit.

The profit of providing the active power to the grid can be calculated by

$$profit^n_{P,Grid} = \begin{cases} -(\delta_3 \times f(n)) \times P^n_{Grid} \times \Delta t, & P^n_{Grid} \geq 0, \\ (\delta_4 \times f(n)) \times P^n_{Grid} \times \Delta t, & P^n_{Grid} < 0, \end{cases} \tag{3.4}$$

where P^n_{Grid} is the active power. If $P^n_{Grid} \geq 0$, the EVs are wanting to be charged and the car park purchases the electricity from the grid at a wholesale price with

the price coefficient δ_3. Otherwise, the EVs are set to discharge energy to the grid and the car park sells the electricity at a wholesale price with the price coefficient δ_4.

Due to the energy storage devices, the active power provided by the grid during the nth time slot can be calculated by

$$P^n_{Grid} = P^n_{EVs} + P^n_{storage}, \tag{3.5}$$

where P^n_{EVs} is the charged energy for EVs and $P^n_{storage}$ is the energy stored in the storage devices during the nth time slot. The energy stored in storage devices can compensate the active power difference flexibly according to requirements for energy by the EVs and grid.

Then, taking (3.3), (3.4) and (3.5) into account, the total profit for the car park selling or buying the active power from the grid and EVs can be calculated by

$$profit^n_p = ((\delta_1 - \delta_3) \times f(n)) \sum_{n=1}^{N} \left\{ \sum_{m=1}^{M} E^n_{m,c} \right\} - ((\delta_4 - \delta_2) \times f(n)) \sum_{n=1}^{N} \left\{ \sum_{m=1}^{M} E^n_{m,d} \right\}, \tag{3.6}$$

where M is the total number of EVs parking during the nth time slot, N the total number of periods during the opening hours for the car park, $E^n_{m,c}$ and $E^n_{m,d}$ are the charging and discharging energy for the mth EV during the nth time slot, respectively. Then, this profit is the sum of the charging and discharging active power incomes from the grid and the EV owners.

The second profit of providing the reactive power to the grid can be calculated by

$$profit^n_Q = price^n_Q \times Q^n_{Grid} \times \Delta t, \quad Q^n_{Grid} \leq 0, \tag{3.7}$$

where Q^n_{Grid} is the reactive power that can be provided to the grid and $price^n_Q$ the reactive power price. Since the grid always hungers for the reactive power, the provided reactive power with the direction from the grid to the customers is always negative.

According to (3.6) and (3.7), the overall profit for the car park during the nth time slot can be calculated as

$$profit^n = profit_P^n + profit_Q^n. \tag{3.8}$$

3.3 Proposed Charging/Discharging Scheme

3.3.1 Objective function

In this section, an optimal charging scheme is proposed to maximize the efficiency and profits for the car park owner.

In this model, the electricity price, charging time and desired SOC are all taken into account to allow EVs to participate in the V2G, G2V and V2V system. Note that the reactive power reference is set to be zero to operate at the unity power factor normally, when there is no requirement of reactive power profit. When the main grid requires the reactive power, the car park can provide the reactive power to the grid as requested for up to its maximum capacity. It can be clearly seen that the reactive power profit is always larger than or equal to zero for the car park. The profit of the reactive power can be added or deleted directly in the objective function. Optimizing the active power profit is the main target in this charging/discharging scheme. Then, according to (3.8), the objective function J at the nth time slot can be described as

$$J(n) = \sum_{n=1}^{N} \left\{ (price_{EV} - price_{CP}) \times \sum_{m=1}^{M} E_m^n \right\}, \tag{3.9}$$

where $price_{EV}$ and $price_{CP}$ are the electricity prices for EV customers and the car park owner, respectively. Based on (3.3), they can be calculated by

$$price_{EV} = \frac{1}{2}\left[(\delta_1 + \delta_2) + (\delta_1 - \delta_2)\right] \times sign(\sum_{m=1}^{M} E_m^n) \times f(n), \tag{3.10}$$

and

$$price_{CP} = \frac{1}{2}\left[(\delta_3 + \delta_4) + (\delta_3 - \delta_4)\right] \times sign(\sum_{m=1}^{M} E_m^n) \times f(n). \tag{3.11}$$

Substituting (3.10) and (3.11) into (3.9) yields

$$J(n) = \sum_{n=1}^{N} \left\{ \frac{1}{2} \left[\begin{array}{c} ((\delta_1 + \delta_2) - (\delta_3 + \delta_4) + (\delta_1 - \delta_2) \\ -(\delta_3 - \delta_4)) sign(\sum_{m=1}^{M} E_m^n) \times f(n) \end{array} \right] \times \sum_{m=1}^{M} E_m^n \right\}. \tag{3.12}$$

When operated under the assumption that the electricity price for purchasing and selling are the same in the simulation (i.e. $\delta_1 = \delta_2$ and $\delta_3 = \delta_4$), the profit for the EV driver is in the most conservative state. As the electricity price gap between the charging and discharging modes increases, the benefits for EV drivers and the car park will increase. Then, the objective function J can be rewritten as

$$J(n) = \sum_{n=1}^{N} \left\{ (\delta_1 - \delta_3) \times f(n) \times \sum_{m=1}^{M} E_m^n \right\}. \tag{3.13}$$

3.3.2 System constraints

The following constraints are defined for the proposed algorithm.

$$\left\{ \begin{array}{l} 0 \leq p_m^n \leq p_{m,c,max} \\ -p_{m,d,max} \leq p_m^n \leq 0 \end{array} \right., \tag{3.14}$$

$$E_m^n = p_m^n \Delta t = \left\{ \begin{array}{ll} E_{m,c}^n, & p_m^n \geq 0 \\ E_{m,d}^n, & p_m^n < 0 \end{array} \right., \tag{3.15}$$

$$E_m = SOC_{m,ini} \times C_m + \sum_{n=1}^{N'_m} E_m^n, \quad N'_m \in [0, [\frac{t_m}{\Delta t}]], \tag{3.16}$$

$$E_{m,need} = \sum_{n=1}^{N_m} E_m^n = \sum_{n=1}^{N_m} (p_m^n \times \Delta t), \tag{3.17}$$

$$0 \leq E_m \leq E_{m,nned} \leq C_m, \tag{3.18}$$

$$20\% \leq SOC \leq 90\%, \tag{3.19}$$

$$0 \leq P_{storage}^n \leq P_{storage,rated}, \tag{3.20}$$

$$P_{Grid}^n = P_{EVs}^n + P_{storage}^n. \tag{3.21}$$

Constraint (3.14) ensures that the charging rate calculated by the optimal charging scheme will be kept within the range of the charging power. Constraints (3.15) - (3.17) assign the charging energy during each time slot and show the current energy stored in batteries. In this way, EVs can be charged or discharged to the anticipated value. Constraint (3.18) is proposed to avoid overcharge or over-discharge. Besides, in order to avoid negative influence to the battery lifetime, the range of SOCs is set as a default range between 20% and 90% by the car park if car owners do not set it, as shown in constraint (3.19). However, if the final SOC is set out of the range by customers, the EVs should be charged or discharged to the desired values. For example, if an EV customer sets the final SOC as 100%, the range of this EVs SOC will be updated between 20% and 100%. Constraints (3.20) and (3.21) show that the storage device is designed to compensate the active power difference between the EVs and grid demands within its maximum capacity.

3.3.3 Algorithm

The mathematics model is set up in Matlab by using Yalmip Wiki and the optimization problem is solved by the solver-IBM ILOG Cplex Optimizer 12.6.1.

At the beginning of each day, the central controller updates the system information, e.g. the amount of energy stored in energy devices. Then, at the beginning of a time slot Δt, the central controller performs the actions, following the flow chart presented in Fig. 3.5. All the unplugged EVs are be parked in this car park, but they should be not considered to participate in the charging/discharging scheme.

3.4 Drivers Information

3.4.1 Distribution of vehicles' parking times

In order to develop an accurate car park system model, the probability density function of EVs' parking information is required. An office-type car park, located in

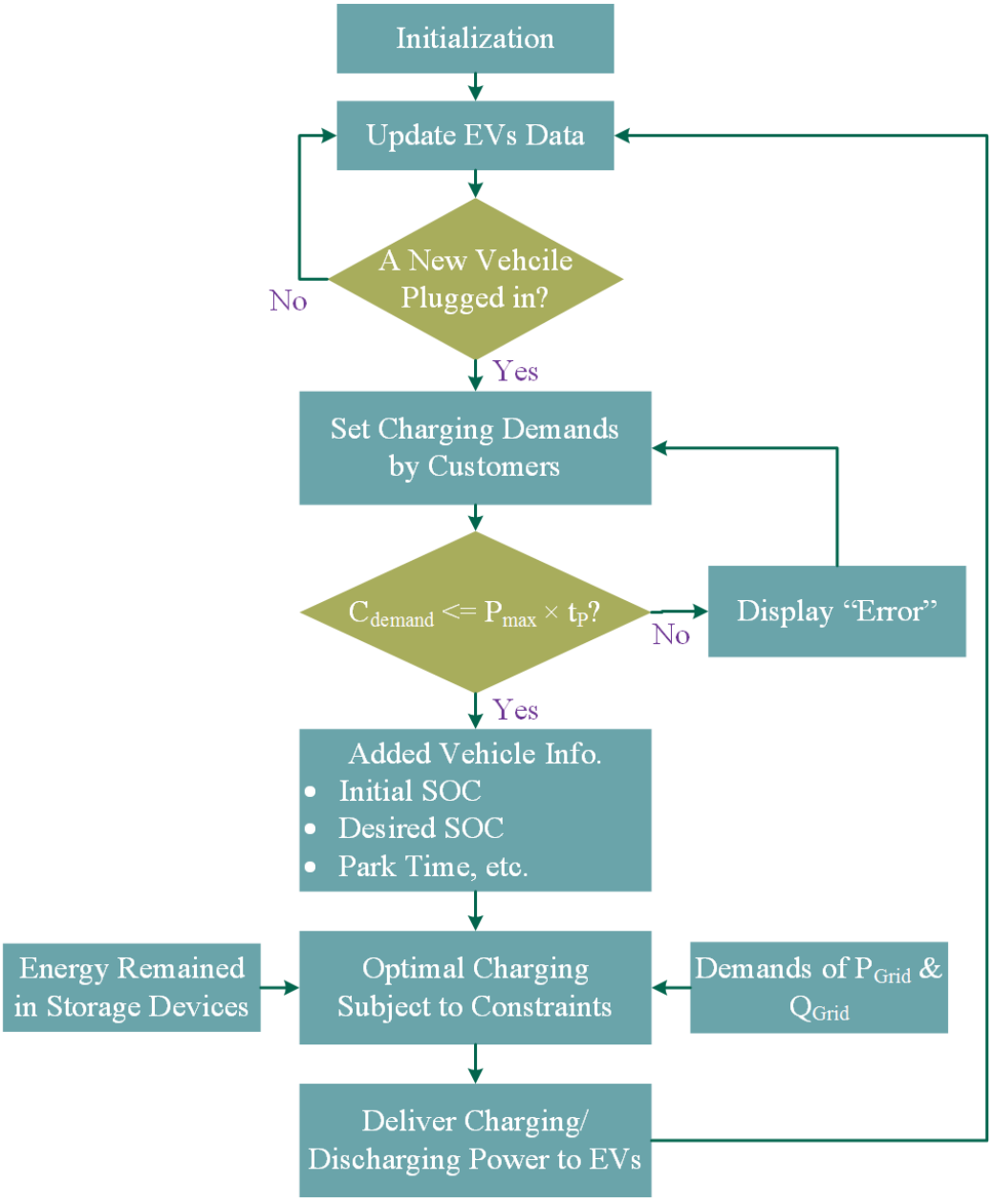

Figure 3.5 : Flow chart of the proposed algorithm.

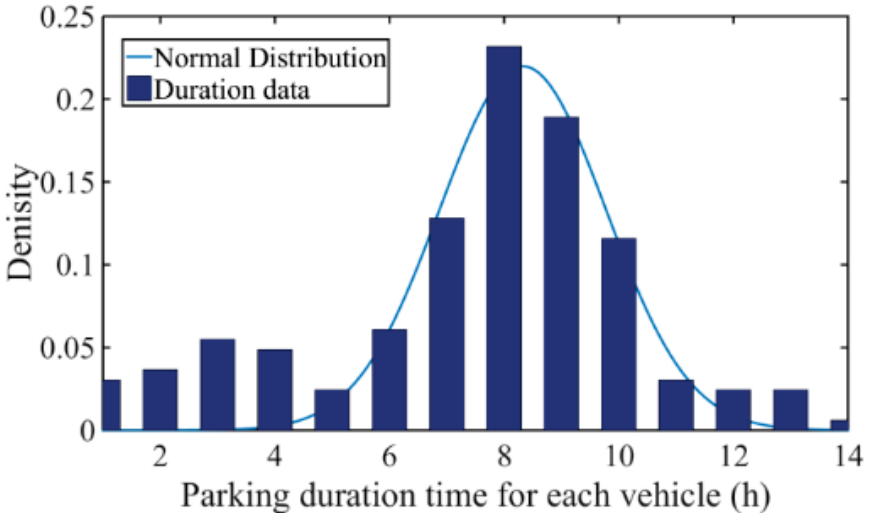

Figure 3.6 : Distribution of parking duration time.

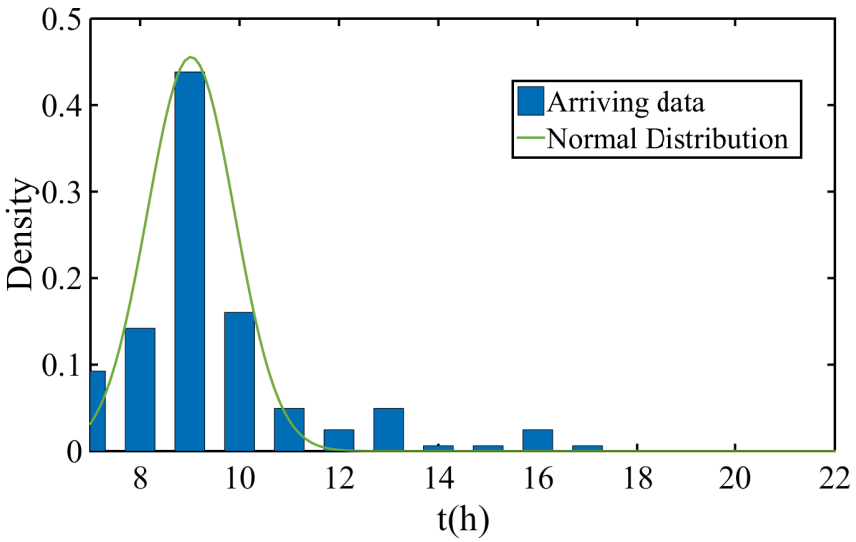

Figure 3.7 : Distribution of arrival time.

the underground level of Building 10 at the University of Technology Sydney (UTS), was investigated. Its opening time is from 7 A.M. to 10 P.M. from Monday to Friday with 150 parking lots. The survey of this UTS car park during a normal working week indicates the parking time of vehicles, as depicted in Fig. 3.6, which is a normally distributed random variable with μ=8.30 h and σ=1.81 h. The distribution

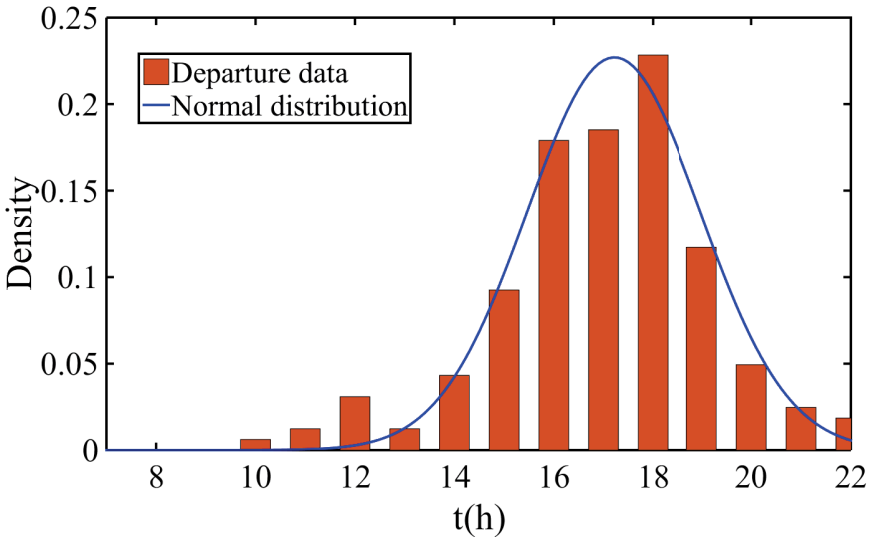

Figure 3.8 : Distribution of departure time.

function for parking hours can be given by

$$f(x;\mu,\sigma) = \frac{1}{\sqrt{2\pi}\sigma} e^{-\frac{(x-\mu)^2}{2\sigma^2}}. \tag{3.22}$$

As shown in Fig. 3.6, most of the vehicles will park more than 3 hours. Their parking duration times are enough to enable EVs to participate in our proposed secondary service in the electricity market.

Similarly, the arrival and departure times follow the normal distributions as well, as depicted in Figs. 3.7 and 3.8, respectively. Table 3.3 lists their distribution parameters.

Although these cars are traditional vehicles, it is reasonable to assume that the behaviours of drivers would change little in the future. Therefore, the information from the survey can be utilized as the EV parking information.

3.4.2 Simulation settings

All EV customers are assumed to have set their demands via the touch screen panels after parking, such as $SOC_{m,fin}$, L, $t_{m,p}$, $p_{m,c,cmax}$, and $p_{m,d,max}$. According

Table 3.3 :

Distribution parameters of arrival and departure times.

Parameter	Arrival	Departure
μ	9.021	17.22
σ	0.8755	1.7572

Table 3.4 :

Simulation settings.

Parameter	Value
C_m	$30 \sim 80$kWh
$SOC_{m,ini}$	$10\% \sim 80\%$
$SOC_{m,fin}$	$50\% \sim 90\%$
Δt	0.5 h
δ_1	1
δ_2	1
δ_3	0.9
δ_4	0.9

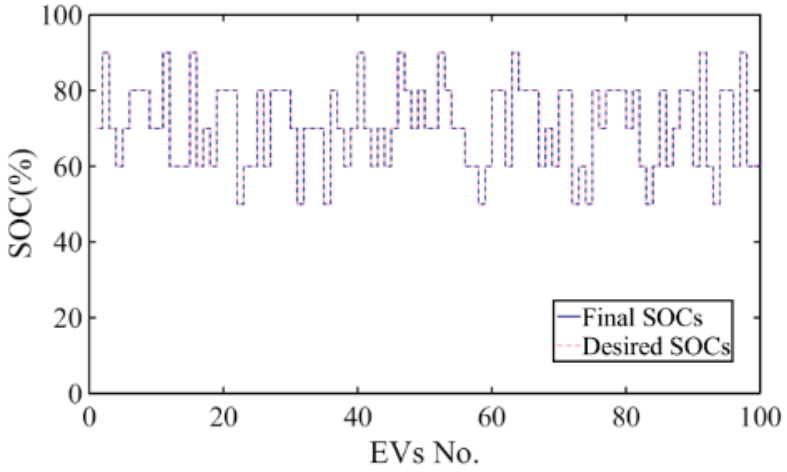

Figure 3.9 : Curve of final SOCs and desired SOCs.

to the behaviour of drivers, Table 3.4 tabulates the range of initial SOCs, the range of final SOCs and the range of capacity of EVs. Meanwhile, four electricity price coefficients (δ_1, δ_2, δ_3 and δ_4) are set as well.

3.5 Results and Discussions

In this section, the simulations are performed by the proposed charging algorithm and the results are presented for the car parks with sizes of M = 100, 200, 300, 400, 500 parking lots. Fig. 3.9 compares the curves of desired and final SOCs. It can be seen that all of the EVs are charged to the desired SOCs prior to their departure times.

Three EVs (EV 17, EV 53 and EV 84) are chosen randomly to observe their SOCs and the variation of their SOCs along with the fluctuation of hourly electricity prices, as shown in Fig. 3.10. The electricity price is shown in on the right side (AUD/kWh). EV 53, which comes to the car park at 1:30 P.M. and leaves at 2:30 P.M., can only be discharged as set by the driver. It is parked for only 1 hour which includes only two time slots. During these two time slots, the curve of its SOC shows that it is discharged at a larger rate during the second time slot, which has a

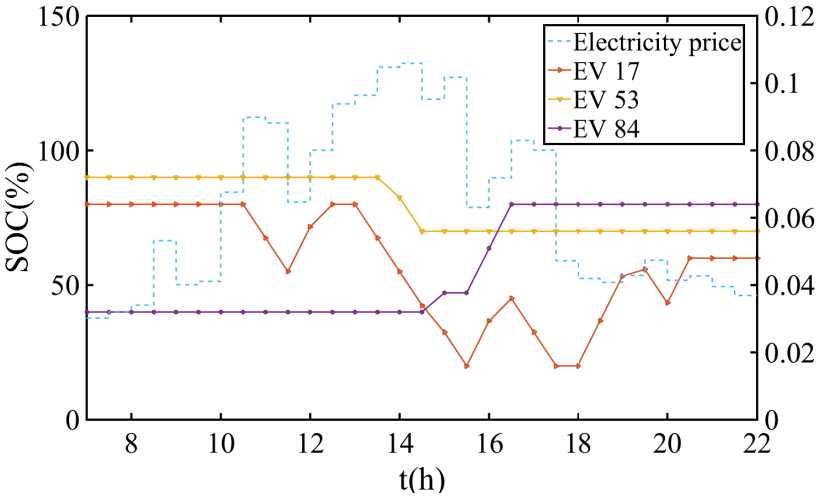

Figure 3.10 : Three EVs SOCs and hourly prices.

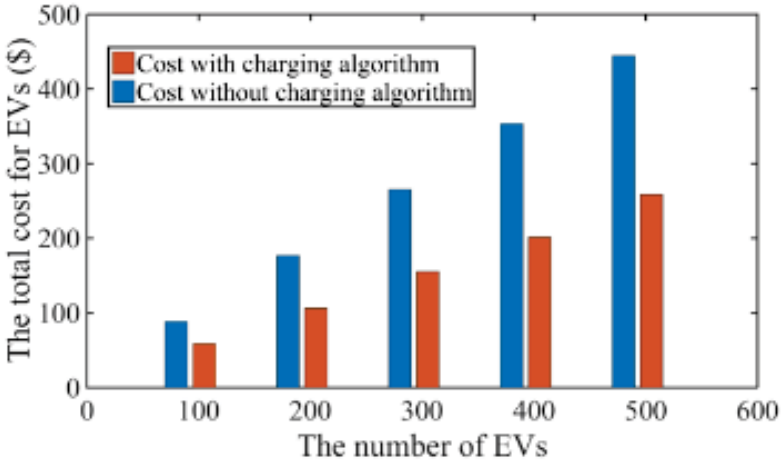

Figure 3.11 : Total costs for EVs.

higher price for selling the electricity than the first time slot.

Similarly, EV 84, which can only be charged, comes in at 2:30 P.M. and leaves at 4:30 P.M. During the parking periods, it is charged quickly from 3:30 P.M to its departure time, because the electricity price is much lower during this period. EV 17, with the charging type L set to zero, is set to be charged and discharged several times during the parking period and leaves at the desired SOC value. It is also set to be charged during low-price periods and be discharged during high-price periods.

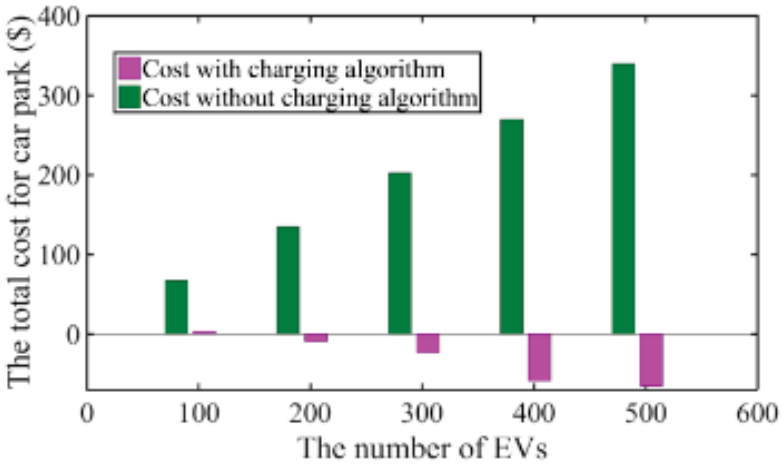

Figure 3.12 : Total costs for car park.

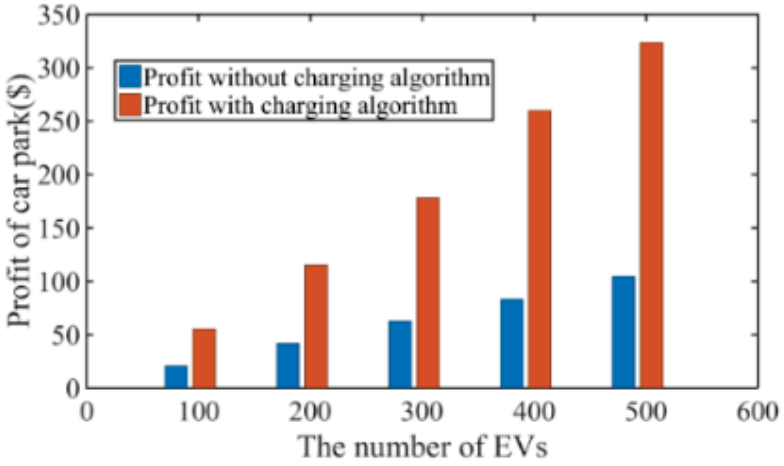

Figure 3.13 : Active power profits for car park.

An unregulated charging/discharging scheme is used for comparison with the proposed method. With this method, EVs will be charged/discharged with an average power rate during the parking hours. The power rate is calculated by using the expected charging/discharging energy divided by the parking time. It can be seen from Figs. 3.12 and 3.13 that the costs for EV customers and the car park owner with the charging scheme are much lower than the ones with the traditional scheme, respectively. Specifically, the costs for customers can be reduced by 47% on average, compared with the unregulated charging method.

Fig. 3.12 shows that the cost of the car park with the optimal scheme are negative, which means that the car park does not have to pay money to the power grid even though it takes energy from it. In Fig. 3.13, the profits for the car park using the proposed charging method are around 3 times of that obtained by unregulated charging with different car park sizes M.

3.6 Concluding Remarks

This chapter presents a smart electrical car park model involving the V2G and G2V technology, which enables bidirectional power flow. In order to calculate the optimal charging/discharging power rates, the real hourly electricity price is collected and analysed. An optimal charging scheme has been proposed. It aims at making profits for the car park owner and minimizing the cost to EV customers. The simulation is performed in Matlab with the real-world parking information collected from an underground car park at UTS. Compared with the results of the conventional charging algorithm, the simulation results show that the benefit to the car park owner can be increased by approximately 300%. Also, the spending of EV customers is reduced by 47% on average. At the same time, the SOCs of EVs at their departure times can reach the expected values set by customers. Furthermore, this system can provide a near optimal solution, which can be of great benefit to customers, car park owners and the main grid simultaneously. The car park owners can make profits and the car drivers can reduce the cost for parking and charging their EVs.

Chapter 4

FOUR-QUADRANT OPERATIONS OF A BIDIRECTIONAL EV CHARGER

4.1 Introduction

With the integration of electrical vehicles (EVs), car parks located in office buildings and shopping malls have shown an enormous potential to incorporate EV batteries into the power grid. To exploit this commercial potential, a smart car park, where a large population of EVs can be parked, was proposed in the previous chapter [76]. The proposed smart car park system consists of bidirectional charging stations, a control centre and energy storage devices, as presented in Fig. 4.1. The central controller coordinates the power received among the EV batteries and the main grid.

As a critical component in electrified transportation, EV batteries support the main grid by charging or discharging the active power from or to the grid via on or off-board unidirectional or bidirectional chargers [79]. The unidirectional chargers only transmit the active power from the grid to the EV batteries at a unity power factor generally. In order to achieve a two-way delivery of the active power, bidirectional topologies have been studied [80, 81]. Apart from exchanging the active power between the EV batteries and the power grid, known as vehicle-to-grid (V2G) and grid-to-vehicle (G2V) operations, it is possible for the EV to produce or consume the reactive power in connection with the grid. This operation mode is known as the vehicle-for-grid (V4G) mode, where the EV batteries can be applied as static VAR compensators (SVCs). Currently, capacitor banks, SVCs and static synchronous compensators, etc. are used to compensate the reactive power in the

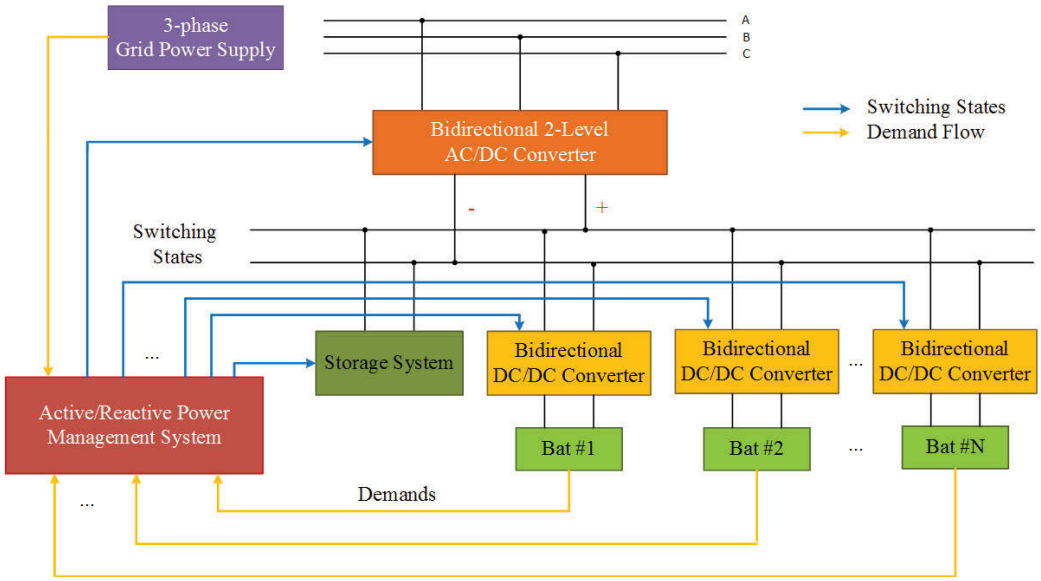

Figure 4.1 : Diagram of the smart car park system.

utility grid.

In [23], Kesler et al. proposed a V2G reactive power operation for a single-phase on-board EV charger, where the charger operates in G2V mode with or without exchanging the reactive power. The authors have also studied a three-phase off-board fast charger in [24] to work in the positive axis of active power, P, in the PQ plane. However, both papers focus on exchanging the reactive power only when the EVs are charged from the grid. Besides these operations, the operation V4G combined with V2G is considered and analysed. The system can work properly in all regions of the PQ plane. As an example, in [82], EVs are studied to provide reactive power to the main grid and compensate current harmonics in smart homes with a single-phase charger. Compared with the single-phase chargers used in smart homes, a three-phase two-stage bidirectional battery charger is more suitable for commercial applications. The proportional integral (PI) controllers and phase-locked loop (PLL) algorithms are used in these papers [23, 24, 82]. Their results show that it takes around 3 cycles or 60 ms in the case of 50 Hz to reach the new working condition. Adapted from direct torque control (DTC) for motor control, direct power control

(DPC) is another popular control scheme for power converters, which can have fast dynamic performance. A designed switching table is used to select an optimal switching state [83]. Unlike the PI controller, the DPC does not need the PLL, the internal current loop or modulators. However, this method introduces high power ripples, which leads to highly distorted grid currents.

In order to improve the dynamic and steady state performance and avoid using PLLs, in this chapter, a two-cascaded MPC is proposed to control the active and reactive power flows between the EV batteries and the power grid, simultaneously. Due to the ease of implementation and combination of multi-objectives, the MPC algorithm has attracted the recent attention of many researchers. Most of these papers use MPC to control a resistive load for unity power factor operation or DC-link voltage regulation, similar to that in [84] and [85]. The proposed MPC method in this project is designed to control an EV battery to achieve the bidirectional four-quadrant operation in the PQ plane.

PLLs are used to synchronize the grid current with the supply voltage and achieve the modulation by detecting the phase angle. The grid current magnitude is calculated from the active and reactive power commands through PI controllers in [23], [24] and [82]. Since MPC is free of modulation and no need of synchronization, the PLL algorithm is not required [86]. By controlling the active and reactive power directly by MPC, the PI controllers can also be avoided. The control strategies proposed in [24] and [82] take about 3 grid cycles (60 ms in the case of 50 Hz) to respond to new active or reactive power commands. With the proposed MPC scheme, a much faster dynamic response of about 2 ms can be achieved in controlling a two-stage off-board bidirectional charger. Since the system can reach a new working state much faster, the power quality can be significantly improved. Compared with the results from DPC, the proposed method can also improve the steady state performance by reducing the active and reactive power ripples and the current THD

dramatically.

The proposed two-level MPC scheme consists of a model predictive direct power control (MPDPC) for the grid-side and a model predictive direct current control (MPDCC) method for the EV battery-side. MPDPC is used to track the grid active and reactive power demands. The combination of the active and reactive power errors is designed as the cost function. MPDCC is proposed for the constant current charging of EVs. Both demands from the grid and EV customers can be met effectively using the proposed MPC strategy. To demonstrate the effectiveness of the proposed control method and validate the four-quadrant operations, experimental results obtained with a lab-developed two-stage off-board EV battery charger prototype are presented.

4.2 Description of EV Charger Topology

In this thesis, the charger is controlled to operate in the four quadrants of the PQ plane shown in Fig. 2.1, including the two axes, to track the active and reactive power flows between the battery and the main power grid. The proposed MPC method is used to achieve this objective, due to its ease of implementation and ability to fulfil multiple objectives. The classical topology in Fig. 2.3(b) is used for energy storage systems with the bidirectional power flow [87]. Note that this topology is essentially a boost converter which provides a limited voltage control range, i.e. the grid peak voltage to the maximum battery voltage [88] (this will be proved later in this chapter).

Since the common nominal battery voltage is between 100 and 600 V, a boost AC/DC converter of the typical topology is preferred in the rectification stage with a 120V/240V grid connection [24], [22]. As the chargers should be designed to operate under any charging and discharging commands, a DC/DC half bridge bidirectional converter is used as the second stage to track the battery voltage. With this DC/DC

converter, the charging/discharging range can be enlarged from the peak value of the grid voltage to 0 V, compared to the circuit connected with the battery directly in Fig. 2.3(b). This improved charging/discharging range makes the system topology available for different voltage level EV batteries. The DC/DC converter operates as a buck type converter when the battery is charged from the main grid. On the other hand, it can be controlled as a boost-type converter for V2G operation. Therefore, the off-board bidirectional charger prototype used in this research project is composed of a 2-level three-phase AC/DC converter and a DC/DC converter. The first stage, an AC/DC front-end converter, is connected to the three-phase grid voltage via a filter inductor (L) and resistor (R) in series. A filter capacitor (C) is connected on the DC-side to filter the DC voltage (V_{dc}). As for the second stage, the DC/DC rear-end converter consists of two insulated-gate bipolar transistor-diode switches (G_1 and G_2). It is used to interface with the EV battery through an output inductor (L_{dc}). A filter capacitor (C_{dc}) is connected in parallel with the EV battery.

The switching state of the three-phase AC/DC converter can be determined by gating signals S_a, S_b and S_c on each phase, which are defined as

$$S_k = \begin{cases} 1 & \text{upper switch on phase } k \text{ is on} \\ 0 & \text{lower switch on phase } k \text{ is on} \end{cases}, \tag{4.1}$$

where $k = a, b, c$. For example, $S_a = 1$ means that on the A-phase, S_1 is on and S_2 is off.

According to the space vector pulse width modulation (SVPWM), eight possible switch states can be written in a stationary two-axis reference frame ($\alpha\beta$ coordinate system) as

$$\mathbf{S}_{\alpha\beta} = \frac{2}{3} \begin{bmatrix} 1 & -\frac{1}{2} & -\frac{1}{2} \\ 0 & \frac{\sqrt{3}}{2} & -\frac{\sqrt{3}}{2} \end{bmatrix} \mathbf{S}_{\mathbf{abc}}, \tag{4.2}$$

Table 4.1 :

The converter voltage vectors in $\alpha\beta$ coordinate.

NO.	S_a	S_b	S_c	S_α	S_β	V_α	V_β	$\|V_\alpha+\mathrm{j}V_\beta\|$
0	0	0	0	0	0	0	0	0
1	1	0	0	$\frac{2}{3}$	0	$\frac{2V_{dc}}{3}$	0	$\frac{2V_{dc}}{3}$
2	1	1	0	$\frac{1}{3}$	$\frac{1}{\sqrt{3}}$	$\frac{V_{dc}}{3}$	$\frac{V_{dc}}{\sqrt{3}}$	$\frac{2V_{dc}}{3}$
3	0	1	0	$-\frac{1}{3}$	$\frac{1}{\sqrt{3}}$	$-\frac{V_{dc}}{3}$	$\frac{V_{dc}}{\sqrt{3}}$	$\frac{2V_{dc}}{3}$
4	0	1	1	$-\frac{2}{3}$	0	$-\frac{2V_{dc}}{3}$	0	$\frac{2V_{dc}}{3}$
5	0	0	1	$-\frac{1}{3}$	$-\frac{1}{\sqrt{3}}$	$-\frac{V_{dc}}{3}$	$-\frac{V_{dc}}{\sqrt{3}}$	$\frac{2V_{dc}}{3}$
6	1	0	1	$\frac{1}{3}$	$-\frac{1}{\sqrt{3}}$	$\frac{V_{dc}}{3}$	$-\frac{V_{dc}}{\sqrt{3}}$	$\frac{2V_{dc}}{3}$
7	1	1	1	0	0	0	0	0

where

$$\mathbf{S}_{\alpha\beta} = \begin{bmatrix} S_\alpha \\ S_\beta \end{bmatrix}, \quad \mathbf{S_{abc}} = \begin{bmatrix} S_a \\ S_b \\ S_c \end{bmatrix}.$$

Then the input voltage (V_{in}) of the three-phase AC/DC converter in the $\alpha\beta$ coordinate system can be expressed by using the switching matrix as

$$\mathbf{v}_{\alpha\beta} = \begin{bmatrix} v_\alpha \\ v_\beta \end{bmatrix} = \mathbf{S}_{\alpha\beta} V_{dc} = \begin{bmatrix} S_\alpha \\ S_\beta \end{bmatrix} V_{dc}. \tag{4.3}$$

These eight input voltage vectors of the converter can be obtained from the eight possible switching states, as listed in Table 4.1 and Fig. 4.2.

Assume that the reference voltage V_{ref} is located in sector 1 of the vector diagram presented in Fig. 4.2. Based on the parallelogram rule, V_{ref} can be obtained from

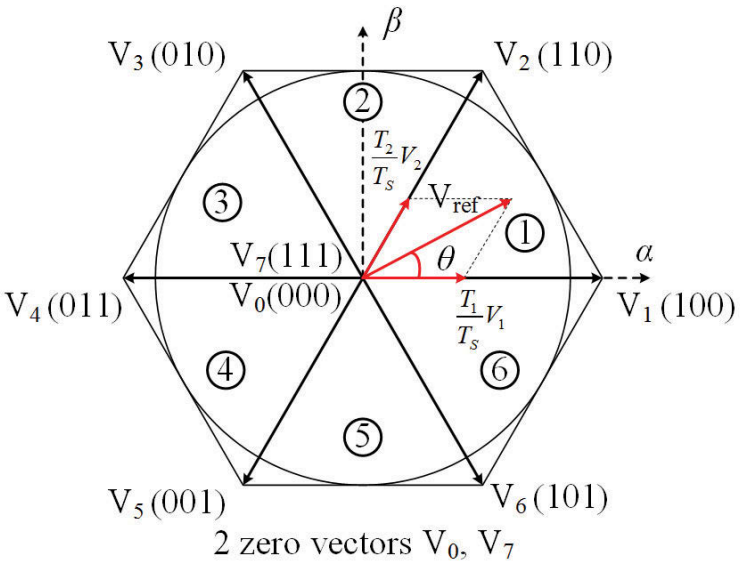

Figure 4.2 : Eight converter input voltage vectors.

the two closest voltage vectors (V_1 and V_2) by

$$\begin{cases} \frac{T_1}{T_s}V_1 + \frac{T_2}{T_s}V_2 = V_{ref} \\ T_1 + T_2 + T_0 = T_s \end{cases}, \tag{4.4}$$

where T_1, T_2 and T_0 are the action periods for the three basic voltage vectors V_1, V_2 and $V_{0,7}$, respectively.

In the $\alpha\beta$ coordinate system, the included angle between the reference value (V_{ref}) and the voltage vector (V_1) is denoted as θ. By the sine rule, the relationship among V_1, V_2 and V_{ref} can be expressed as

$$\frac{|V_{ref}|}{sin(\frac{2\pi}{3})} = \frac{|\frac{T_1}{T_s}V_1|}{sin(\frac{\pi}{3}-\theta)} = \frac{|\frac{T_2}{T_s}V_2|}{sin\theta}. \tag{4.5}$$

Since both the amplitudes of V_1 and V_2 are equal to $\frac{2V_{dc}}{3}$, (4.4) and (4.5) can be rewritten as

$$\begin{cases} T_1 = mT_s sin(\frac{\pi}{3}-\theta) \\ T_2 = mT_s sin\theta \\ T_0 = T_s - T_1 - T_2 \end{cases}, \tag{4.6}$$

where

$$m = \frac{\sqrt{3}|V_{ref}|}{V_{dc}}, \tag{4.7}$$

is the SVPWM modulation index.

In the space vector modulation, the following system constraint condition should be met

$$T_1 + T_2 \leq T_s. \tag{4.8}$$

Substituting (4.6) and (4.7) into (4.8), one can express the system constraint

$$|V_{ref}| \leq \frac{V_{dc}}{\sqrt{3}sin(\frac{\pi}{3} + \theta)}. \tag{4.9}$$

In order to satisfy (4.9) for any included angle θ, it can be deduced that

$$V_m = |V_{ref}| \leq \frac{V_{dc}}{\sqrt{3}}, \tag{4.10}$$

or

$$V_{dc} \geq \sqrt{3}V_m = V_{ph-ph}, \tag{4.11}$$

where V_m is the amplitude of phase voltage and V_{ph-ph} the voltage between two phase lines, or the line-to-line voltage.

Therefore, the output DC-link voltage V_{dc} of the three-phase AC/DC converter has a minimum value. With the topology in Fig. 2.3(b), the range of the battery voltage is limited from the line voltage of the grid to the fully charged voltage of the battery. In order to achieve the full range charging/discharging from the minimum to the maximum battery voltage, a DC/DC bidirectional converter is used to interface with the battery, as described in Fig. 4.3.

4.3 Proposed MPC Scheme

4.3.1 Conventional DPC

Derived from DTC, DPC has now been widely used in controlling converters [89]. The basic principle of DPC is that the errors between the commands and cal-

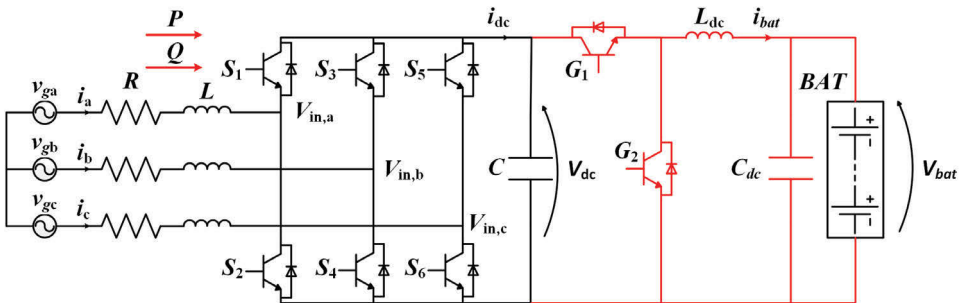

Figure 4.3 : Circuit topology of AC/DC converter connected with battery via a DC/DC converter.

culated values of active and reactive powers will produce two digitized error signals via two hysteresis comparators. The three-phase grid voltage is converted into a voltage vector in the $\alpha\beta$ plane. Based on the location of the voltage vector, the $\alpha\beta$ plane is divided into 12 sectors. The two error signals along with the pre-calculated sector location of the current grid voltage are transferred to a switching table. An optimal switching state is selected from the designed switching table to control the instantaneous active and reactive powers [90].

4.3.2 MPDPC for grid-side

The proposed two-cascaded model predictive control (MPC) scheme is shown in Fig. 4.4, including a model predictive direct power control (MPDPC) and model predictive direct current control (MPDCC) for AC/DC and DC/DC converters, respectively. The main working principle of the MPDPC scheme is to select an appropriate switching state to minimize the cost function. The cost function (g) is designed as the error between the predicted and reference values of the controlled variables. The appropriate switching state that minimizes the cost function is chosen for the next sample interval to track the commands.

It is assumed that a balanced three-phase grid power supply is provided in the system (in Fig. 4.3). Applying the Kirchoff's voltage law and the standard $\alpha\beta$

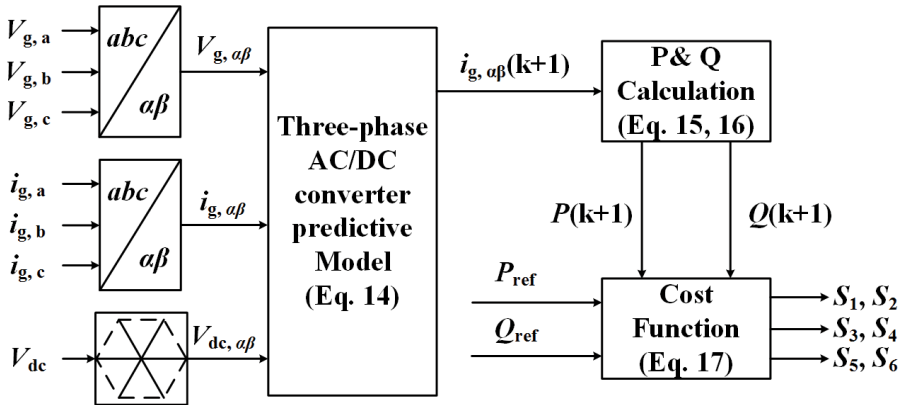

(a) Controller for AC/DC converter.

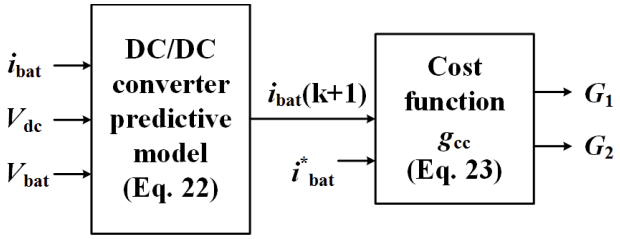

(b) Controller for DC/DC converter.

Figure 4.4 : Proposed MPC scheme for two-stage charger.

frame transformation, the input current dynamic of the charger's first stage can be expressed in the vector form as

$$L\frac{d\mathbf{i}_{\mathbf{g},\alpha\beta}}{dt} = \mathbf{v}_{\mathbf{g},\alpha\beta} - R\mathbf{i}_{\mathbf{g},\alpha\beta} - \mathbf{v}_{\alpha\beta}, \tag{4.12}$$

where $\mathbf{v}_{\mathbf{g},\alpha\beta}$ and $\mathbf{i}_{\mathbf{g},\alpha\beta}$ are the grid input voltage and current vectors in the $\alpha\beta$ frame, respectively, and can be calculated by

$$\mathbf{v}_{\mathbf{g},\alpha\beta} = \begin{bmatrix} v_{g,\alpha} \\ V_{g,\beta} \end{bmatrix} = \frac{2}{3}\begin{bmatrix} 1 & -\frac{1}{2} & -\frac{1}{2} \\ 0 & \frac{\sqrt{3}}{2} & -\frac{\sqrt{3}}{2} \end{bmatrix}\begin{bmatrix} v_{g,a} \\ v_{g,b} \\ v_{g,c} \end{bmatrix},$$

$$\mathbf{i}_{\mathbf{g},\alpha\beta} = \begin{bmatrix} i_{g,\alpha} \\ i_{g,\beta} \end{bmatrix} = \frac{2}{3}\begin{bmatrix} 1 & -\frac{1}{2} & -\frac{1}{2} \\ 0 & \frac{\sqrt{3}}{2} & -\frac{\sqrt{3}}{2} \end{bmatrix}\begin{bmatrix} i_{g,a} \\ i_{g,b} \\ i_{g,c} \end{bmatrix}.$$

Based on the forward Euler approximation, the derivative of the input currents in the continuous-time model can be represented with a sampling period T_s as

$$\frac{d\mathbf{i}_{\mathbf{g},\alpha\beta}}{dt} = \frac{\mathbf{i}_{\mathbf{g},\alpha\beta}(k+1) - \mathbf{i}_{\mathbf{g},\alpha\beta}(k)}{T_s}. \tag{4.13}$$

The grid current (4.12) can then be expressed in the discrete-time domain as

$$\mathbf{i}_{\mathbf{g},\alpha\beta}(k+1) = \frac{T_s}{L}(\mathbf{v}_{\mathbf{g},\alpha\beta}(k) - R\mathbf{i}_{\mathbf{g},\alpha\beta}(k) - \mathbf{v}_{\alpha\beta}(k)) + \mathbf{i}_{\mathbf{g},\alpha\beta}(k) \tag{4.14}$$

Eight future instantaneous power transmitting from the grid to the battery at the $(k+1)$th instant can be predicted on the basis of the eight predicted input currents as

$$\begin{aligned} P(k+1) &= \frac{3}{2} Re\left\{\mathbf{v_g}\mathbf{i}_\mathbf{g}^*\right\} \\ &= \frac{3}{2}(v_{g,\alpha}(k+1)i_{g,\alpha}(k+1) + v_{g,\beta}(k+1)i_{g,\beta}(k+1)) \end{aligned} \tag{4.15}$$

$$\begin{aligned} Q(k+1) &= \frac{3}{2} Im\left\{\mathbf{v_g}\mathbf{i}_\mathbf{g}^*\right\} \\ &= \frac{3}{2}(v_{g,\beta}(k+1)i_{g,\alpha}(k+1) - v_{g,\alpha}(k+1)i_{g,\beta}(k+1)) \end{aligned} \tag{4.16}$$

where $v_{g,\alpha}(k+1)$, $v_{g,\beta}(k+1)$, $i_{g,\alpha}(k+1)$ and $i_{g,\beta}(k+1)$ are the predicted grid voltage and current values at the $(k+1)$th instant in the $\alpha\beta$ coordinate system. Among the eight future values of the active and reactive powers obtained from the eight possible switching states, a cost function is defined to select an optimal switching state as

$$g = \sqrt{(P_{ref} - P(k+1))^2 + (Q_{ref} - Q(k+1))^2}. \tag{4.17}$$

In the smart carpark system, the power commands (P_{ref} and Q_{ref}) are determined by the centre controller to satisfy the requirements of the power grid and the EV customers.

4.3.3 MPDCC for EV-side

To avoid short-circuiting, the switches G_1 and G_2 are operated in a complementary manner. Therefore, the switching state G is defined as

$$G = \begin{cases} 1 & \text{upper switch } G_1 \text{ is on} \\ 0 & \text{lower switch } G_2 \text{ is on} \end{cases}. \tag{4.18}$$

This means that when G_1 is on and G_2 is off, the switching state G is equal to 1. Otherwise, G is 0.

Based on Kirchhoff's voltage law (KVL), when G is controlled to be 1, the DC-link voltage can be expressed as

$$V_{dc} = L\frac{di_{bat}}{dt} + V_{bat}, \tag{4.19}$$

where V_{dc} is the DC capacitor voltage, and V_{bat} and i_{bat} are, respectively, the instantaneous values of voltage and current of the EV battery.

Similarly, when the switching state G is 0, the KVL of the DC/DC converter can be expressed as

$$0 = L\frac{di_{bat}}{dt} + V_{bat}. \tag{4.20}$$

Combining (4.19) and (4.20), one can express the mathematical model of the DC/DC bidirectional converter as

$$GV_{dc} = L\frac{di_{bat}}{dt} + V_{bat}. \tag{4.21}$$

Then, the battery current can be calculated in the discrete time domain as

$$i_{bat}(k+1) = i_{bat} + \frac{T_s}{L}(GV_{dc} - V_{bat}). \tag{4.22}$$

For constant current charging, the cost function g_{cc} is defined as

$$g_{cc} = (i_{bat} - i^*_{bat})^2, \tag{4.23}$$

where i^*_{bat} is the reference value of the battery current.

Neglecting the power loss in the transmission, the grid active power reference (P_{ref}) can be calculated as

$$P_{ref} = \sum_{n=1}^{N} P^*_{bat\#n} + P_{stor} = \sum_{n=1}^{N} V_{bat\#n} i^*_{bat\#n} + P_{stor}, \tag{4.24}$$

where $P^*_{bat\#n}$, $V_{bat\#n}$ and $i^*_{bat\#n}$ are the charging power reference, voltage and expected charging current of the nth EV battery, respectively, N is the total number of the parked EVs, and P_{stor} the power delivered to the storage system. In this paper, as an example, N is selected as 1 and neglecting the storage system, which leads to $P_{ref} = P^*_{bat} = V_{bat} i^*_{bat}$.

4.4 Proposed Modified MPC

Fig. 4.3 shows the topology of the two-level three-phase off-board bidirectional charger. Based on the system model analysed in (4.12), the complex apparent power $\mathbf{S}$ can be calculated by

$$\mathbf{S} = P + jQ = \frac{3}{2} \mathbf{i_g}^* \mathbf{v_g}, \tag{4.25}$$

where P and Q are the active and reactive power, respectively, flowing from the grid side to the EV battery.

Taking the derivative with respect to time on both sides of (4.25), one obtains

$$\frac{d\mathbf{S}}{dt} = \frac{3}{2}(\mathbf{v_g} \frac{d\mathbf{i}^*}{dt} + \mathbf{i}^* \frac{d\mathbf{v_g}}{dt}). \tag{4.26}$$

For a balanced power supply, the derivative of grid voltage ($\mathbf{v_g}$) can be calculated by

$$\frac{d\mathbf{v_g}}{dt} = \frac{d|\mathbf{v_g}| v_g^{jwt}}{dt} = jw|\mathbf{v_g}| v_g^{jwt} = jw\mathbf{v_g}. \tag{4.27}$$

According to the system model in (4.12), the derivative of grid current ($\mathbf{i_g}$) can be obtained as

$$\frac{d\mathbf{i_g}}{dt} = \frac{1}{L}(\mathbf{v_g} - \mathbf{v} - R\mathbf{i_g}). \tag{4.28}$$

Substituting (4.27) and (4.28) into (4.26) yields

$$\frac{d\mathbf{S}}{dt} = \frac{3}{2L}(|v_g|^2 - v_g v^*) + (jw - \frac{R}{L})\mathbf{S}. \tag{4.29}$$

The discrete-time model of the complex apparent power at the (k+1)th instant for a sample time T_s can be expressed as

$$\mathbf{S^{k+1}} = \mathbf{S^k} + \frac{d\mathbf{S^k}}{dt}. \tag{4.30}$$

In order to track the active and reactive references, the cost function for this stage can be designed as the square of the magnitude of the apparent power error, expressed as

$$\begin{aligned} F_1 &= |\mathbf{S^{ref}} - \mathbf{S^{k+1}}|^2 \\ &= (P^{ref} - P^{k+1})^2 + (Q^{ref} - Q^{k+1})^2, \end{aligned} \tag{4.31}$$

where P^{ref} and Q^{ref} are the reference values of the active and reactive power, respectively. Ignoring the power loss during the transmission, P^{ref} is equal to the power charged or discharged by the battery, calculated by the battery current reference timing the DC voltage V_{dc}. Q^{ref} can be controlled to meet the requirement of the main grid.

The mathematical model of the second-stage DC/DC half bridge can be written as

$$GV_{dc} = L\frac{di_{bat}}{dt} + V_{bat}, \tag{4.32}$$

where i_{bat} and V_{bat} are the battery current and voltage, respectively, and G is the switching state. G equals 1, when G_1 is on and G_2 is off. Otherwise, it is set to be zero.

The predicted current for the next sampling time can be calculated by

$$i_{bat}^{k+1} = i_{bat}^k + \frac{T_s}{L}(GV_{dc}^k - V_{bat}^k). \tag{4.33}$$

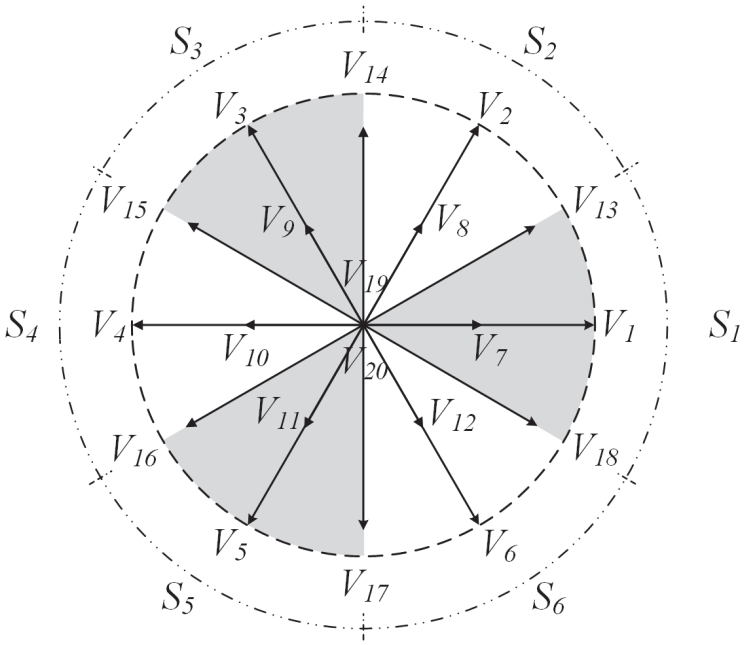

Figure 4.5 : Basic and extended voltage vectors

To achieve the constant current charging for the EV battery, the cost function for the second stage is defined as

$$F_2 = |i_{bat}^{ref} - i_{bat}^{k+1}|, \tag{4.34}$$

where i_{bat}^{ref} is the reference value of the battery current.

4.4.1 Modulation of the extended voltage vectors

Twenty voltage vectors are created in the proposed MMPC method. Two adjacent basic active voltage vectors are modulated, which are selected from the eight possible voltage vectors, including 6 non-zero vectors $(V_1, V_2, \cdots, V_6)$ and 2 zero vectors (V_{19} and V_{20}). The duty ratios for the two basic vectors are fixed as 0.5. The extended voltage vectors along with the corresponding switching states are listed in Table 4.2. For example, the extended voltage V_7 is modulated by V_1 and V_{19}. Both of these two basic voltage vectors operate half period during one sampling time. Since V_{19} is a zero voltage vector, the new voltage vector V_7 is half magnitude of the basic voltage vector V_1 and has the same direction as V_1. The $\alpha\beta$ plane is

Table 4.2 :

Modulation of the extended voltage vectors

Vector Type	Vector No.	Modulated by	Switching state (d = 0.5)
	V_1		1, 0, 0
	V_2		1, 1, 0
Non-zero basic	V_3		0, 1, 0
active vectors	V_4		0, 1, 1
	V_5		0, 0, 1
	V_6		1, 0, 1
	V_7	$V_1 + V_{19}$	d, 0, 0
	V_8	$V_2 + V_{20}$	1, 1, d
	V_9	$V_3 + V_{19}$	0, d, 0
	V_{10}	$V_4 + V_{20}$	d, 1, 1
	V_{11}	$V_5 + V_{19}$	0, 0, d
Extended	V_{12}	$V_6 + V_{20}$	1, d, 1
voltage	V_{13}	$V_1 + V_2$	1, d, 0
	V_{14}	$V_2 + V_3$	d, 1, 0
	V_{15}	$V_3 + V_4$	0, 1, d
	V_{16}	$V_4 + V_5$	0, d, 1
	V_{17}	$V_5 + V_6$	d, 0, 1
	V_{18}	$V_6 + V_7$	1, 0, d
Zero basic	V_{19}		0, 0, 0
active vectors	V_{20}		1, 1, 1

divided into six sectors, S_1, S_2, $\cdots$, S_6. In each sector, there are six voltage vectors, including 4 non-zero vectors and 2 basic zero vectors, as shown in Fig. 4.5.

4.4.2 Pre-selection algorithm

In the conventional cost function, 20 voltage vector candidates should be considered to get the 20 predicted values of active and reactive power, and the conjugate of the converter input vector in (4.29) is also required to be calculated. To reduce the computing time and complexity of the scheme, a cost function for the first-stage charger by using the negative conjugate of the complex apparent power is defined as

$$F_3 = |(-\mathbf{S}^*)^{\mathbf{ref}} - (-\mathbf{S}^*)^{\mathbf{k+1}}|^2. \tag{4.35}$$

From (4.25), the first-derivation of conjugate of complex power can be calculated by

$$\begin{aligned}\frac{d\mathbf{S}^*}{dt} &= \frac{d(\frac{3}{2}\mathbf{i_g}\mathbf{v_g^*})}{dt} \\ &= \frac{3}{2}(\mathbf{v_g^*}\frac{d\mathbf{i_g}}{dt} + \mathbf{i_g}\frac{d\mathbf{v_g^*}}{dt}).\end{aligned} \tag{4.36}$$

Substituting (4.28) into (4.36) yields

$$\begin{aligned}\frac{d\mathbf{S}^*}{dt} &= \frac{3}{2}(\frac{1}{L}(\mathbf{v_g} - \mathbf{v} - R\mathbf{i_g})\mathbf{v_g^*} - jw\mathbf{v_g^*}\mathbf{i_g}) \\ &= \frac{3}{2L}(|v_g|^2 - \mathbf{v}\mathbf{v_g}) - \frac{1}{L}(R\mathbf{S}^* + jwL\mathbf{S}^*).\end{aligned} \tag{4.37}$$

The predicted value of $(-\mathbf{S}^*)^{k+1}$ can be expressed as

$$\begin{aligned}(-\mathbf{S}^*)^{k+1} &= (-\mathbf{S}^*)^k + T_s\frac{d(-\mathbf{S}^*)^k}{dt} \\ &= (-\mathbf{S}^*)^k - T_s\{\frac{3}{2L}(|v_g|^2 - \mathbf{v}\mathbf{v_g}) - \frac{1}{L}(R + jwL)(\mathbf{S}^*)^{\mathbf{k}}\}.\end{aligned} \tag{4.38}$$

Substituting (4.38) into (4.35), the cost function can be rewritten as

$$\begin{aligned}F_3 &= |\mathbf{err} - \frac{3T_s}{2L}\mathbf{v_g}\mathbf{v}|^2, \\ &= |\mathbf{err} - \frac{3T_s}{2L}|v_g|\angle\theta_{v_g}\mathbf{v}|^2,\end{aligned} \tag{4.39}$$

where the introduced error, **err**, between the predicted and expected values can be calculated by

$$\mathbf{err} = (-\mathbf{S}^*)^{ref} - (-\mathbf{S}^*)^k + \frac{T_s}{L}(\frac{3}{2}v_g^2 - (R + jwL)(\mathbf{S}^*)^k). \tag{4.40}$$

Based on the analysis, to minimize the cost function (4.39) is to find the voltage vector nearest to **err**. There are two steps for this control scheme. Firstly, one optimal sector S_n (from S_1, S_2, $\cdots$, S_6) where **err** is located should be selected. Then, an optimal switching state from the six switching states located in the selected optimal sector S_n is chosen to minimize the cost function F_3. Since the sampling frequency (8 kHz) is very high compared to the grid frequency 50 Hz, it can be assumed that the grid voltage is is relatively constant during the sampling period and is slow changing. This means that the amplitude of grid voltage v_g in the time instant k is the same as that in the next time instant $k+1$. The grid voltage angle θ_{v_g} should be added to the angle of **err** to synchronize with the input voltage vector **v**. Once the optimal sector S_n is selected, one optimal switching state located in the selected sector S_n is selected to minimize the cost function F_3. As an example, if **err** is located in the first sector S_1, as illustrated in Fig. 4.5, it would be better to use the vectors in sector S_1. This pre-selection algorithm helps reduce the complexity by using 6 vectors instead of 20 vectors. In each sector, there are six voltage vector candidates, as summarized in Table 4.3. The control algorithm of the proposed MMPC method is shown in Fig. 4.6.

4.5 Simulation Results

To verify the effectiveness of the proposed MPC and the improved MMPC methods, these control schemes are numerically simulated in the environment of MATLAB/Simulink on a bidirectional two-level off-board EV charger. Firstly, a system with the real power level connected with a lithium-ion battery is tested using the

Table 4.3 :

Pre-select algorithm

Sector	Vectors					
S_1	V_1	V_7	V_{13}	V_{18}	V_{19}	V_{20}
S_2	V_2	V_8	V_{14}	V_{13}	V_{19}	V_{20}
S_3	V_3	V_9	V_{15}	V_{14}	V_{19}	V_{20}
S_4	V_4	V_{10}	V_{16}	V_{15}	V_{19}	V_{20}
S_5	V_5	V_{11}	V_{17}	V_{16}	V_{19}	V_{20}
S_6	V_6	V_{12}	V_{18}	V_{17}	V_{19}	V_{20}

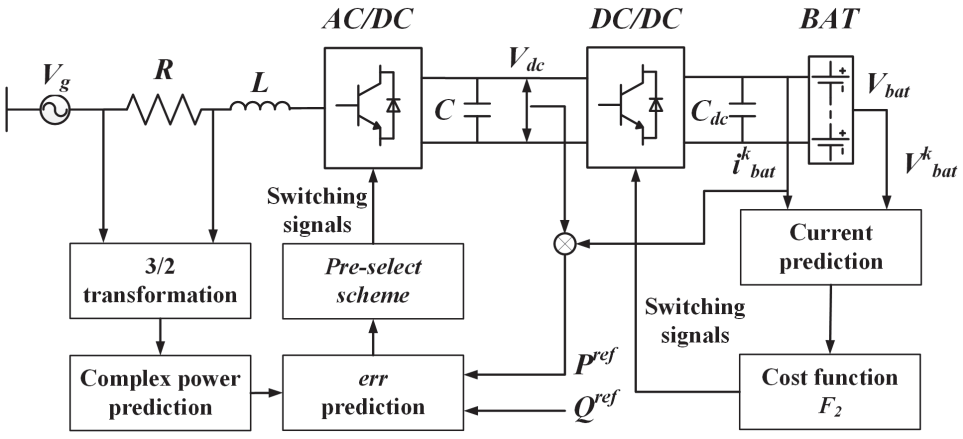

Figure 4.6 : Control diagram for the MMPC method

MPC method. To be consistent with the experimental results, a scaled-down system using the conventional PI, DPC, MPC and MMPC methods are simulated under various operation conditions.

4.5.1 Real power level system

A real power level system for this off-board charger using MPC is simulated in the MATLAB/Simulink. A lithium-ion battery with a nominal voltage at 400 V is used as the EV battery. The nominal current for the battery is set to be 30 A. The grid voltage is 240 V (RMS) on the first stage. The EV charger power is equal to around 12 kW, which would take 4 $\sim$ 8 hours to fully charge a 60 $\sim$ 70 kWh EV battery. The sampling frequency for this simulation is 20 kHz. Three AC filter inductors (16 mH) are connected on the grid side. Firstly, we investigate the battery current tracking during the inductive V4G operation. The reactive power is positive under this condition, i.e. Q_{ref} = 8 kVAR. It can be seen from Fig. 4.7(a) that the system can track the battery current effectively. The battery can be charged or discharged as commanded. The battery voltage is around 430 V. Fig. 4.7(b) shows the active and reactive powers provided from the grid. During the first second, the battery current is 30 A and the battery voltage is approximately 430 V. Therefore, the transferred power is equal to 12.9 kW. It is -12.9 kW during the discharging mode. The reactive power is controlled to the expected value, 8 kVAR. The grid voltage and current on the A-phase are presented in Fig. 4.7(c). Since the reactive power is positive, the current is always lags its associated voltage.

Another operation condition where the reactive power is transferred from the load side to the grid is simulated using the same system parameters. The battery charging/discharging current is also set to 30 A/-30 A. From Fig. 4.8, it can be seen that the system works effectively during the charging and discharging operations. The current reference values can be followed with the MPC method. The reactive

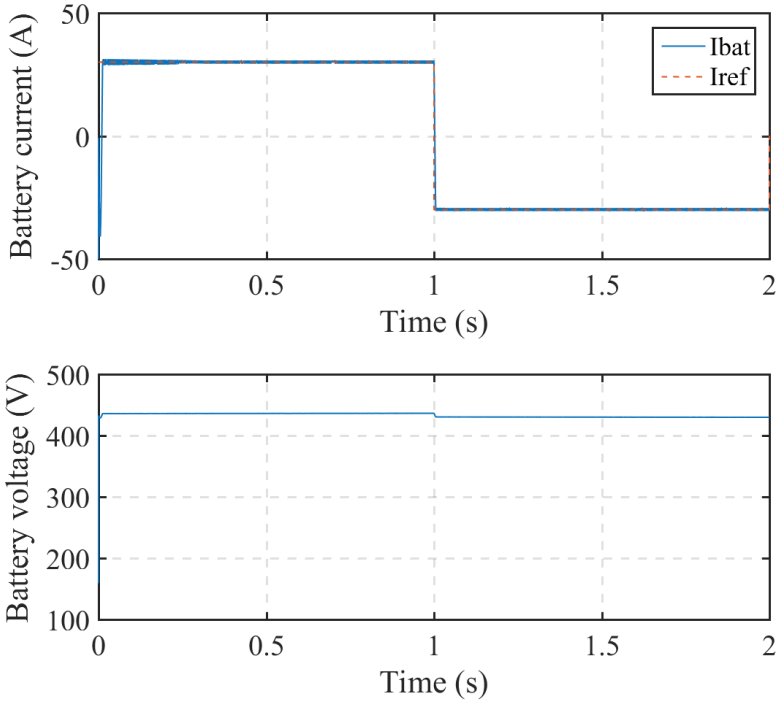

(a) Battery current and voltage performance

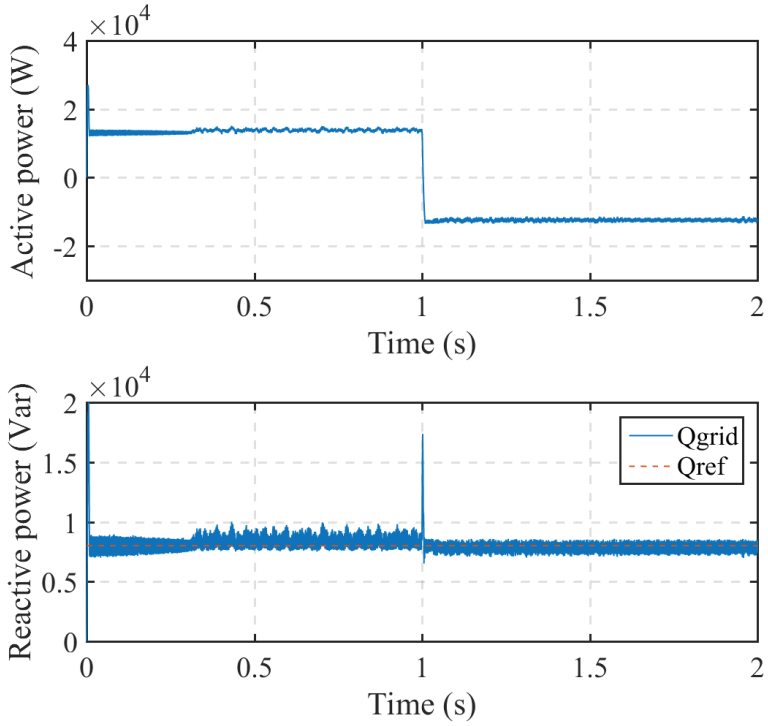

(b) Active and reactive power performance

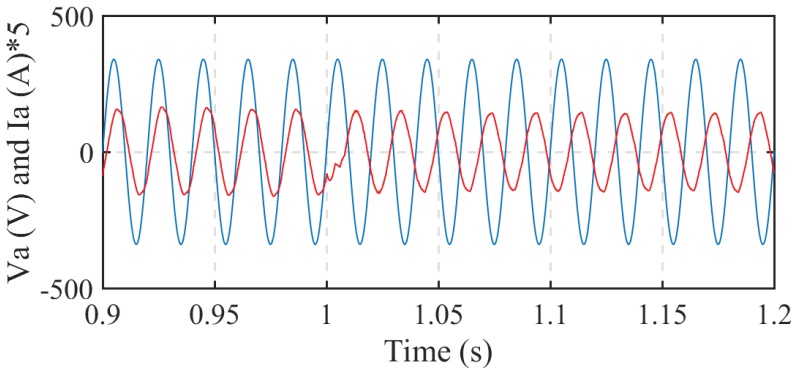

(c) Grid voltage and current performance

Figure 4.7 : Simulation results for real system providing the reactive power.

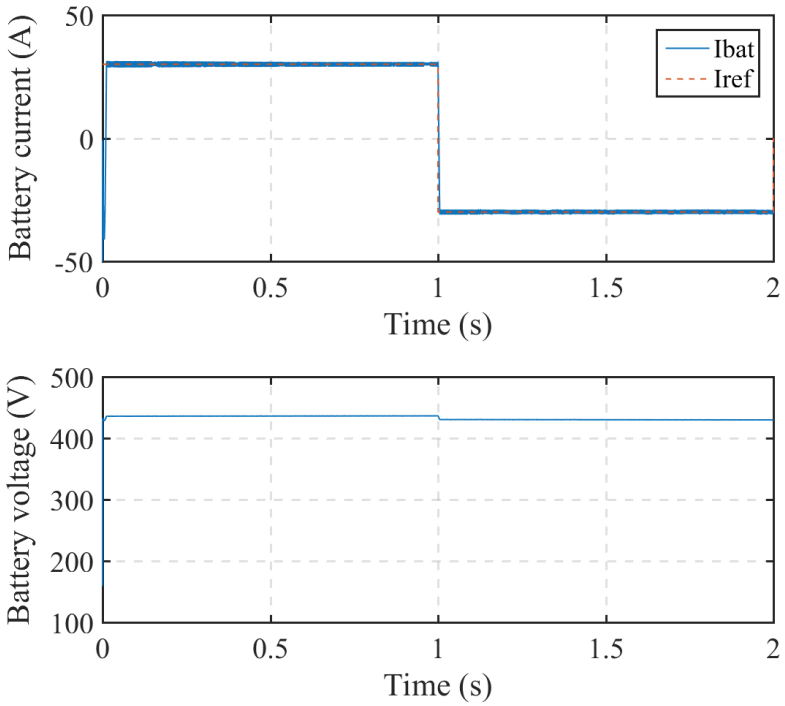

(a) Battery current and voltage performance

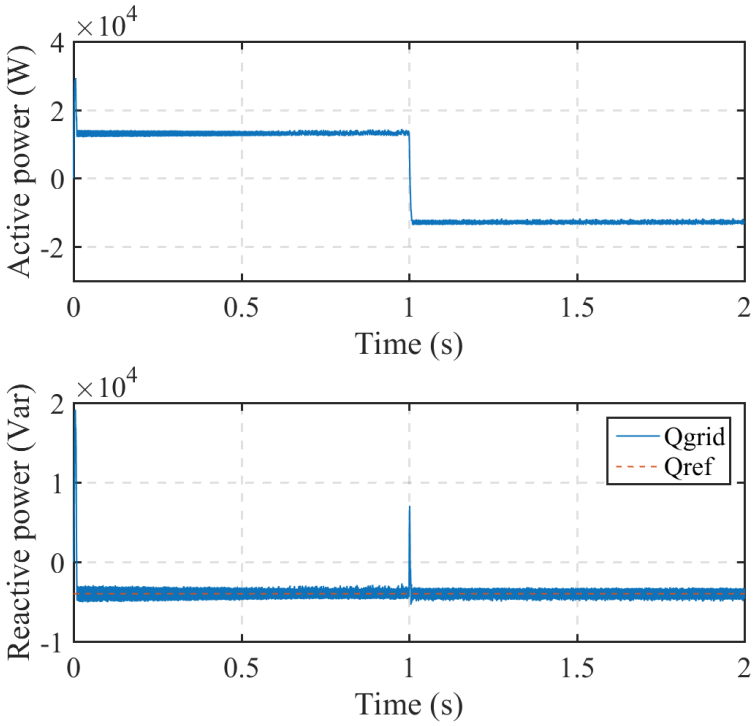

(b) Active and reactive power performance

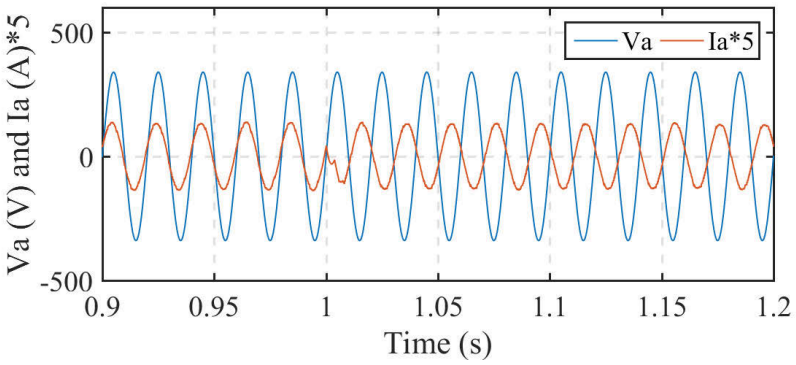

(c) Grid voltage and current performance

Figure 4.8 : Simulation results for real system consuming the reactive power.

power can be controlled to the -4 kVAR. With the negative reactive power, the grid current leads its associated voltage, as shown in Fig. 4.8(c).

4.5.2 Scaled-down system

In [24], Metin, et al. used a PI controller for V2G reactive power operation with an off-board charger. With the proposed system controller, the reactive power reference can be tracked effectively while charging the EV battery. However, it took around 3 grid cycles (60 ms in the case of 50 Hz) to respond to a new command.

By using the proposed MPC method for the system in [24] under the same transient simulation operation, the response time can be reduced dramatically. From the zoomed version of the active and reactive power in Fig. 4.9(a), it can be seen that the response time for the system changing from a unity power factor operation to a 0.4-pf (leading) operation is less than 2 ms. Compared with the 3 cycles (60 ms in the case of 50 Hz) response time in [24] and [82], the response speed is improved significantly. The grid current in Fig. 4.9(b) can also reach the new commanded operation within 2 ms.

Because of the capacity limitation to the experimental setup in the lab, a scaled-down bidirectional EV charger system is used in the experimental test, as shown in Table. 4.4. The simulations for this system using the conventional DPC, proposed MPC and improved MMPC methods are presented. Two working scenarios are designed to observe the EV charger system working under the bidirectional four-quadrant operations, as depicted in Fig. 2.1.

Two simulation scenarios were designed as follows:

(1) This scenario was developed to show the performance under G2V, V2G, and V4G (inductive or capacitive) independent operations. The system only exchanges the active or reactive power between the EV battery and the grid. The charging

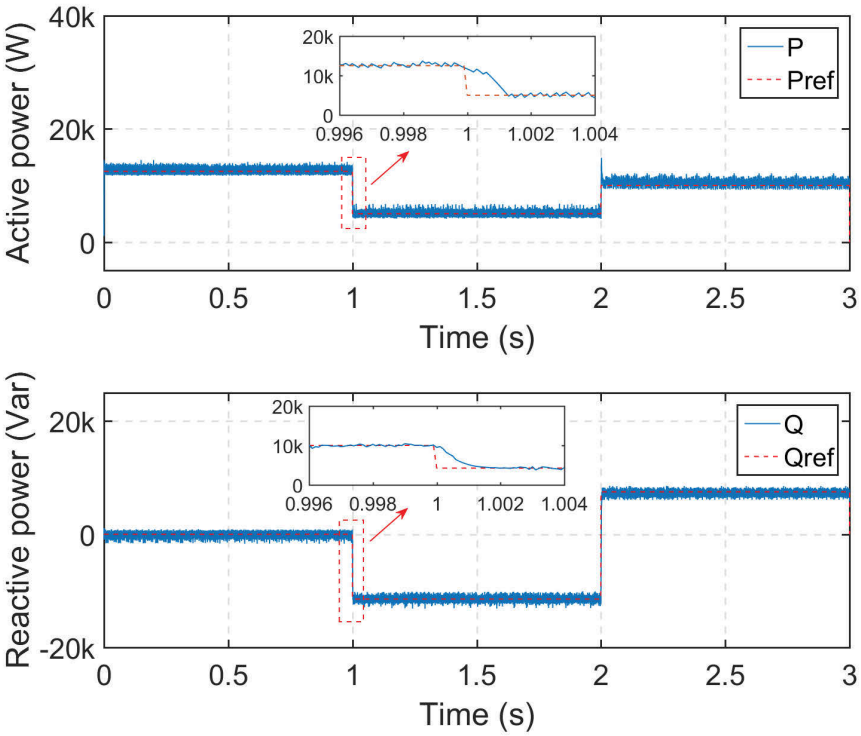

(a) Active and reactive power performance

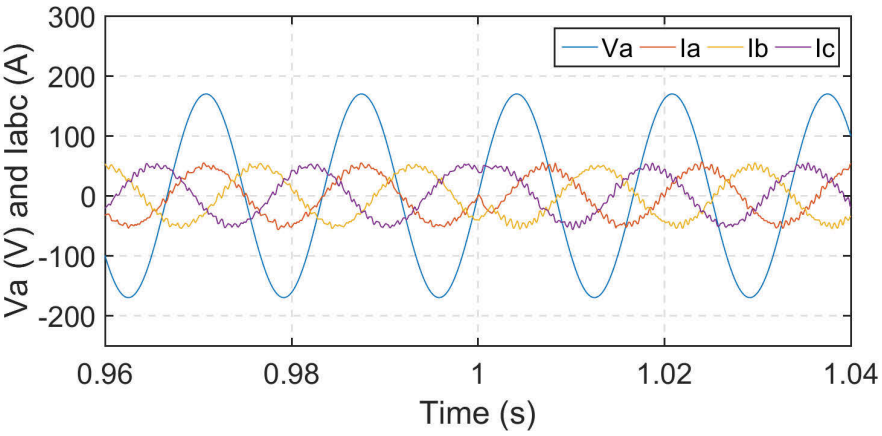

(b) Grid voltage and current performance

Figure 4.9 : Performance by using MPC for system in Ref. [24].

Table 4.4 :

System parameters for simulation and experiment

Symbol	Quantity	Value
L	AC filter inductor	16 mH
C	AC filter capacitor	680 μF
L_{dc}	Output inductor	35 mH
C_{dc}	Output capacitor	68 μF
V_{LL}	Grid line-line voltage (RMS)	100 V
f	Grid frequency	50 Hz
T_s	Sample time	100 μs
V_{bat}	Battery rated voltage	144 V

current i^*_{bat} is varied from 2 A to -2 A at $t = 1\ s$, which leads to the active power reference P_{ref} dropping from around 320 W to -320 W. Then, it steps up to 0 A at $t = 2\ s$, and keeps constant until the end of the experiment. Meanwhile, the reactive power reference keeps 0 VAR during the V2G and G2V operation modes. Then it rises to 400 VAR at $t = 2\ s$ and drops to -400 VAR at $t = 3\ s$ to meet the grid commands.

(2) The second scenario describes the system when it operates in V2G or G2V combined with V4G (inductive or capacitive) modes. Both the active and reactive power are transferred during this scenario. The charging current i^*_{bat} is decreased from 2 A to -2 A at $t = 1\ s$, which means the active power reference P_{ref} is reduced from 315 W to -315 W, and after that, it is restored to 2A at $t = 2\ s$. Then it steps down to -2 A with P_{ref} equal to around -315 W. During each charging or discharging operation, the reactive power reference is reduced from 400 VAR to -400 VAR.

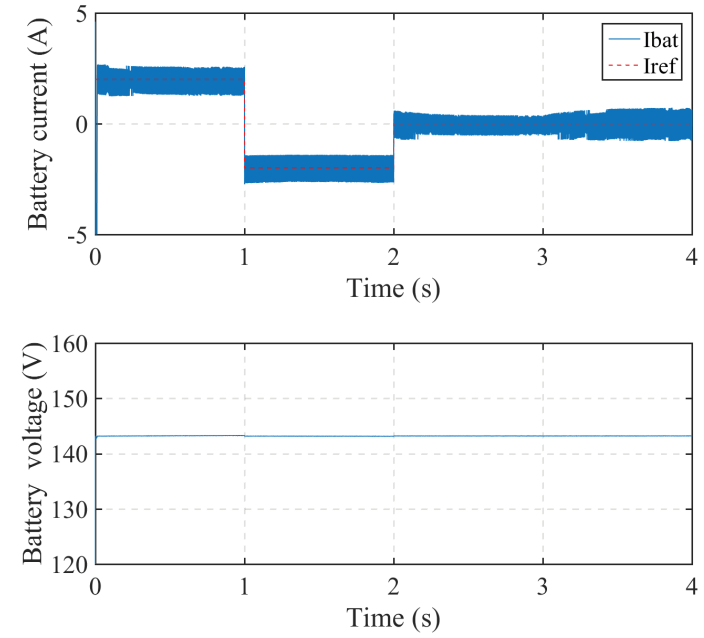

(a) Battery current and voltage performance

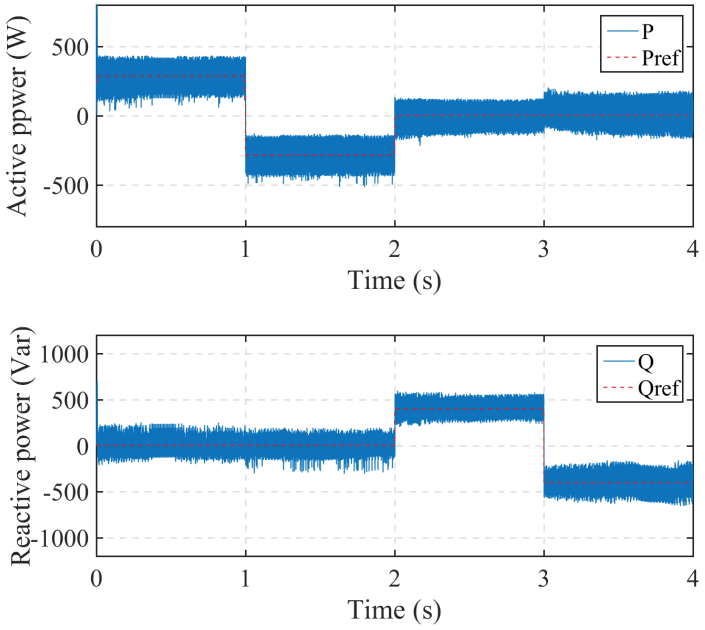

(b) Active and reactive power performance

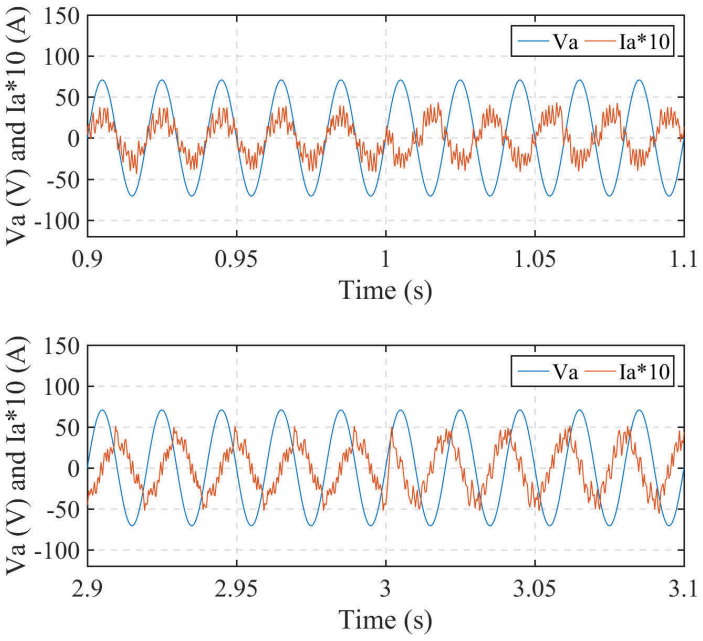

(c) Grid voltage and current performance

Figure 4.10 : Simulation results from DPC during first scenario.

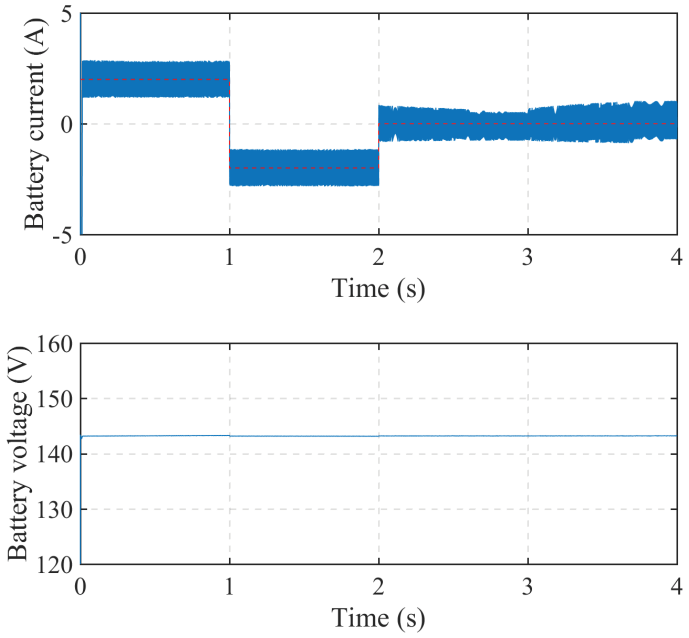

(a) Battery current and voltage performance

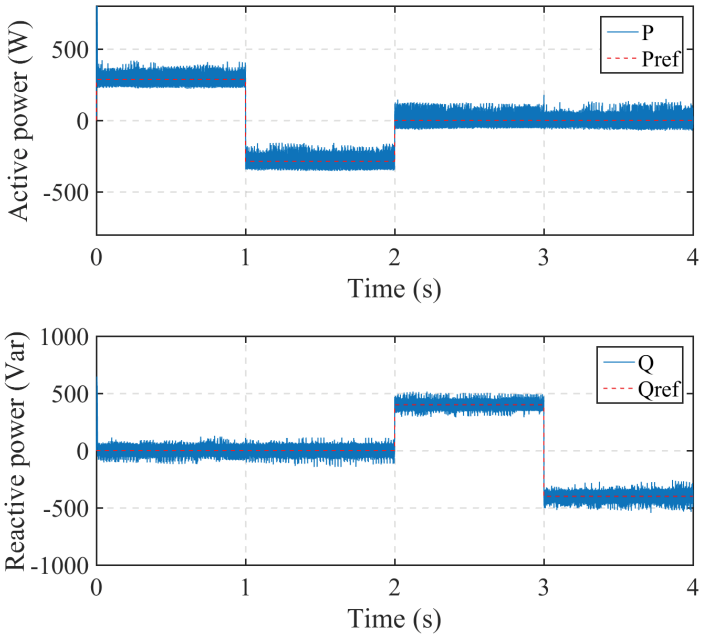

(b) Active and reactive power performance

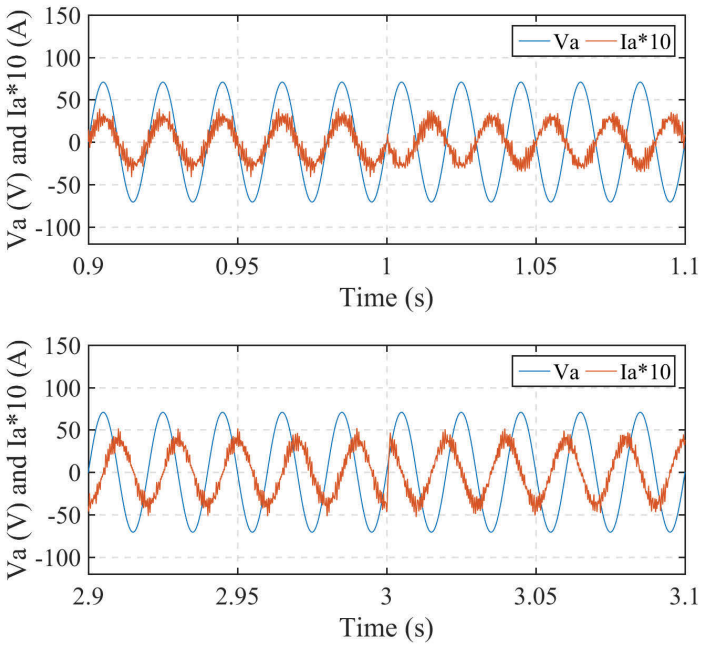

(c) Grid voltage and current performance

Figure 4.11 : Simulation results from MPC during first scenario.

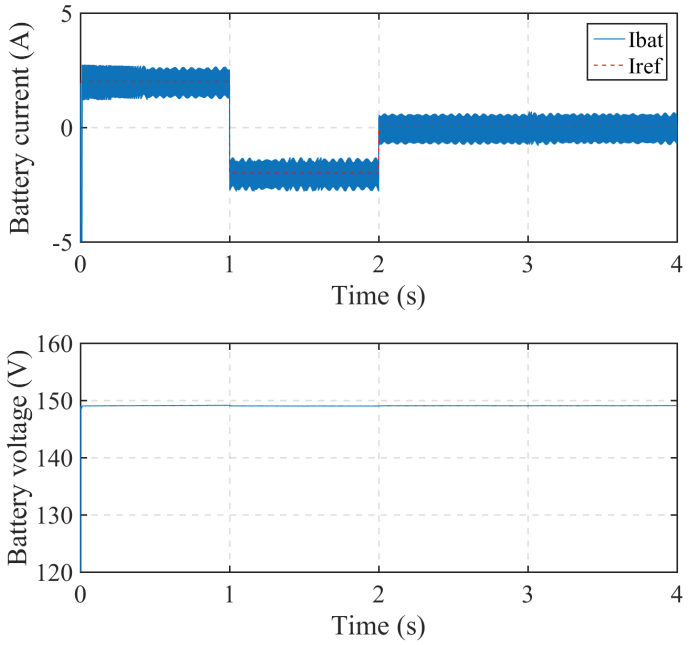

(a) Battery current and voltage performance

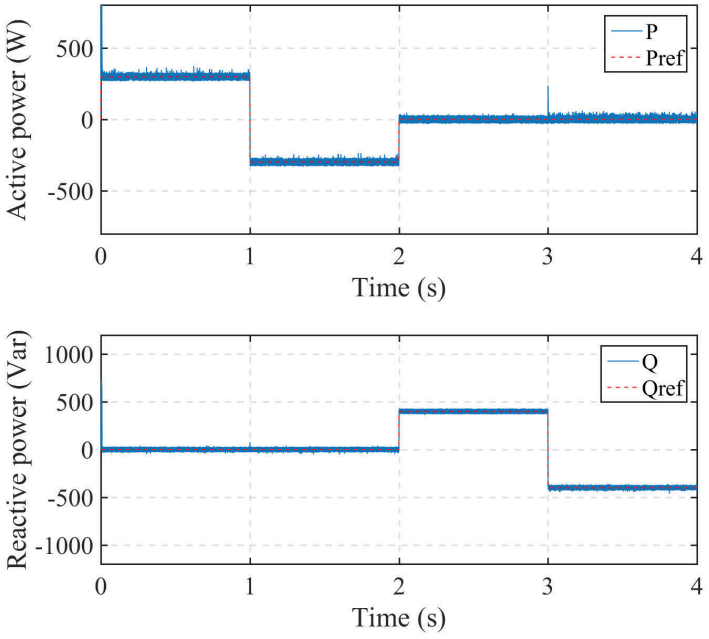

(b) Active and reactive power performance

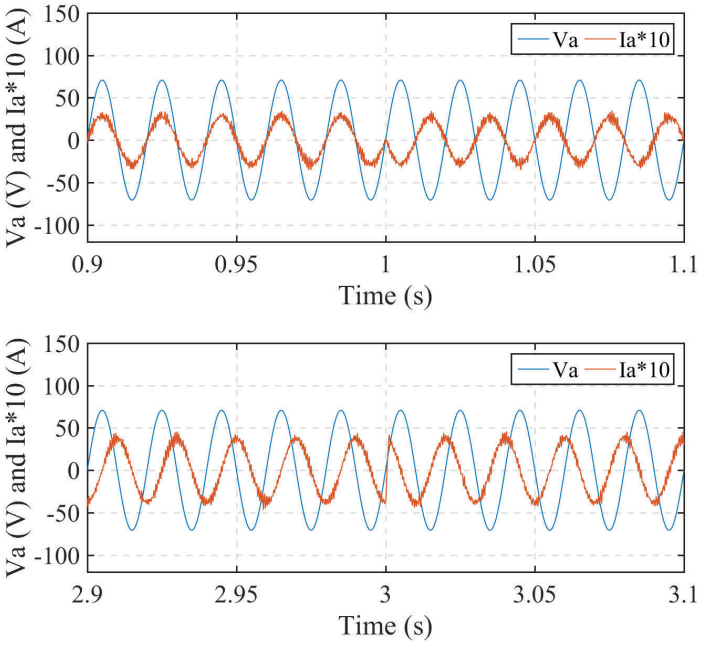

(c) Grid voltage and current performance

Figure 4.12 : Simulation results from MMPC during first scenario.

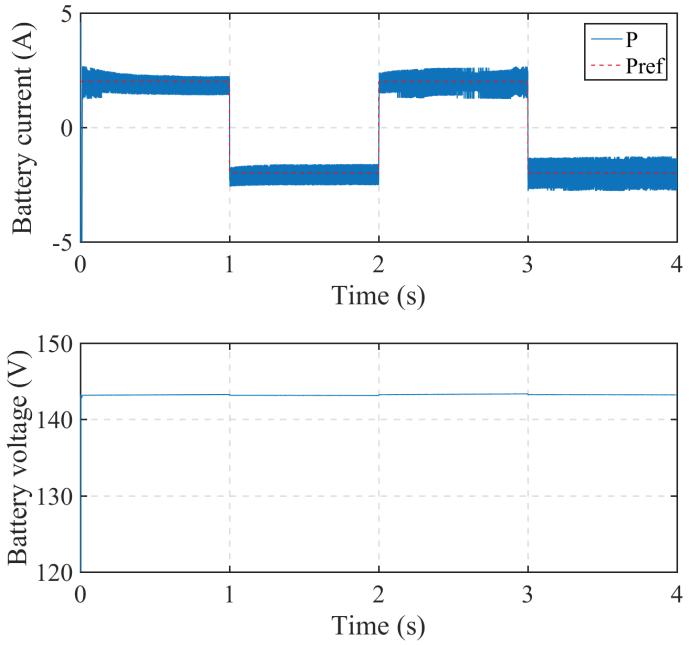

(a) Battery current and voltage performance

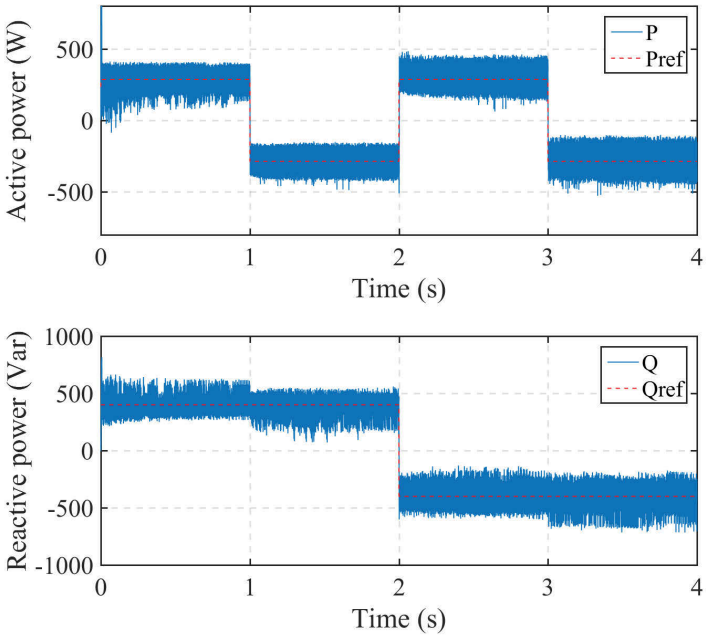

(b) Active and reactive power performance

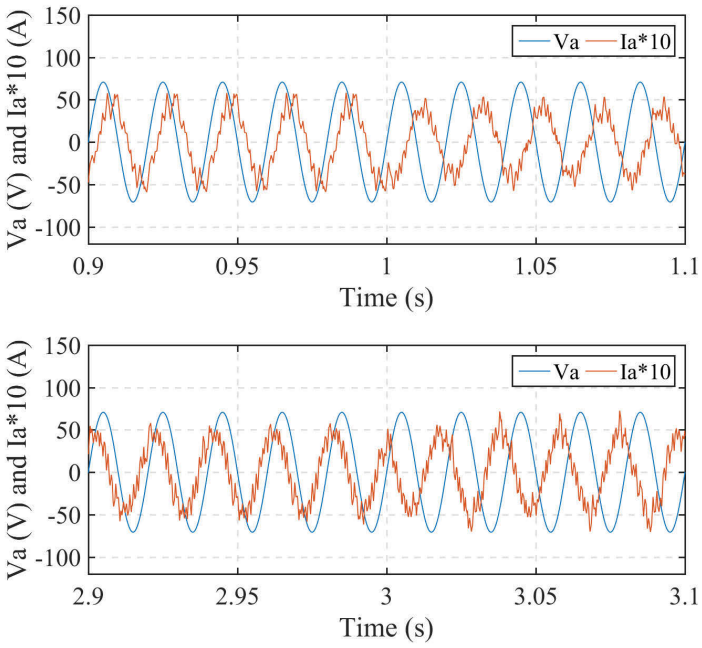

(c) Grid voltage and current performance

Figure 4.13 : Simulation results from DPC during second scenario.

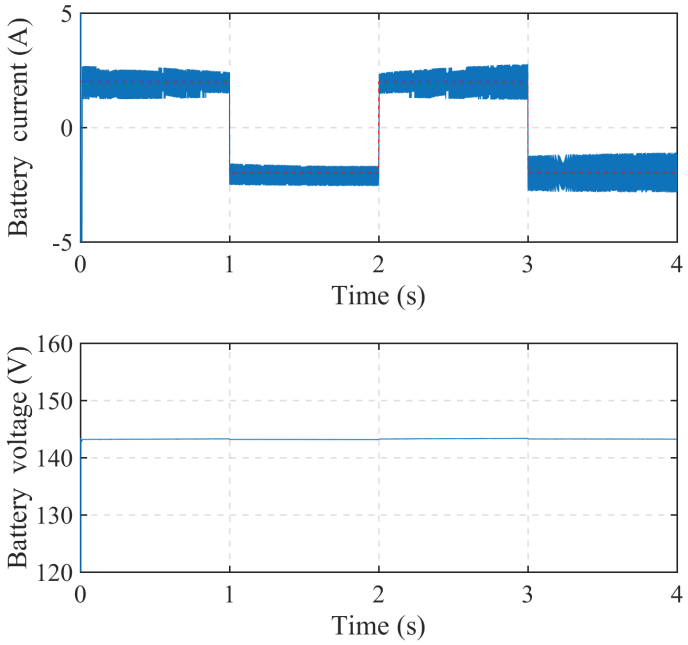

(a) Battery current and voltage performance

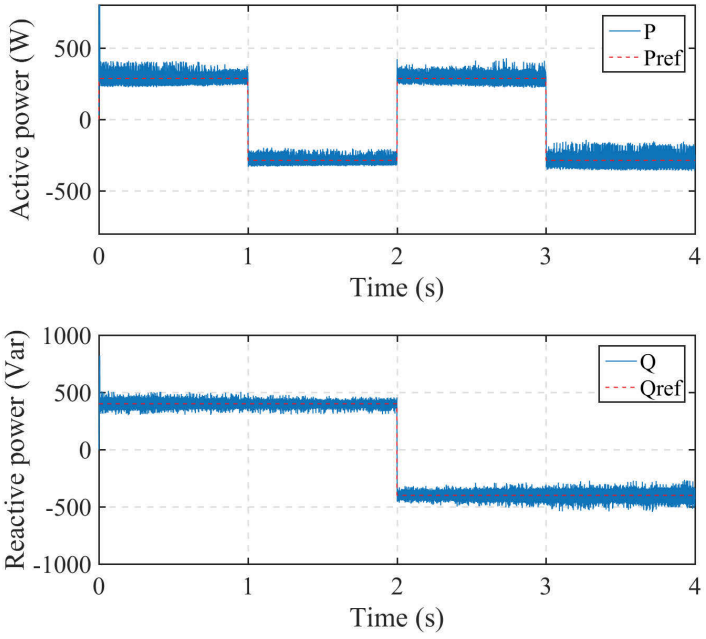

(b) Active and reactive power performance

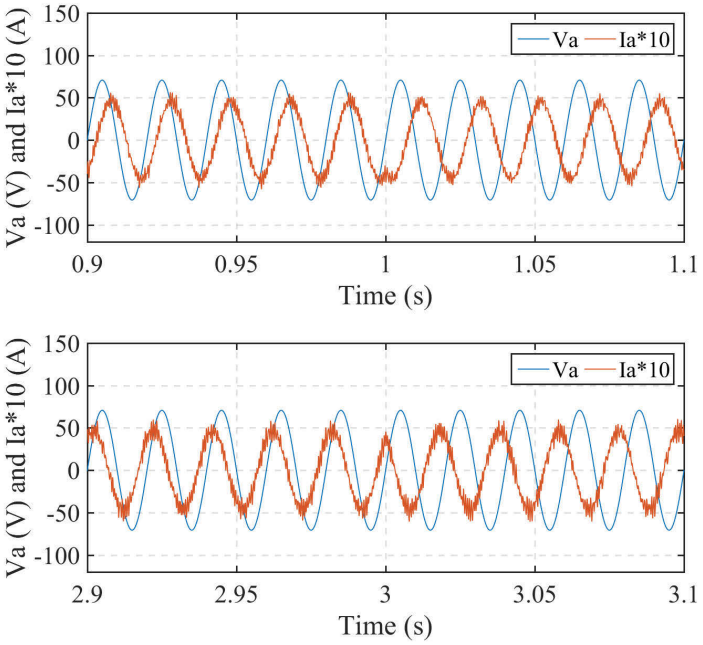

(c) Grid voltage and current performance

Figure 4.14 : Simulation results from MPC during second scenario.

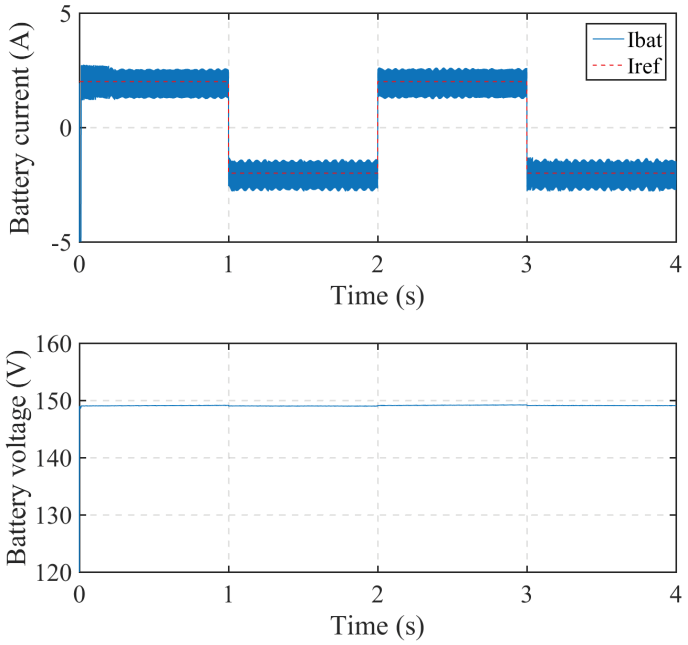

(a) Battery current and voltage performance

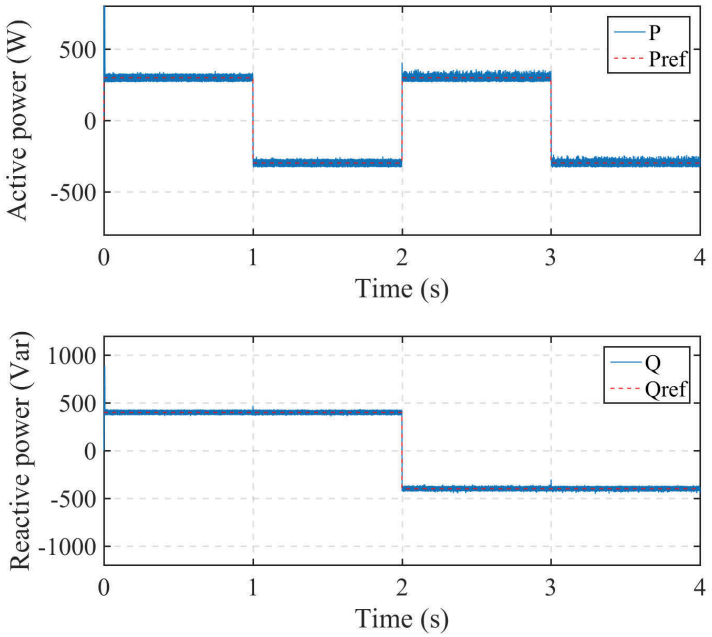

(b) Active and reactive power performance

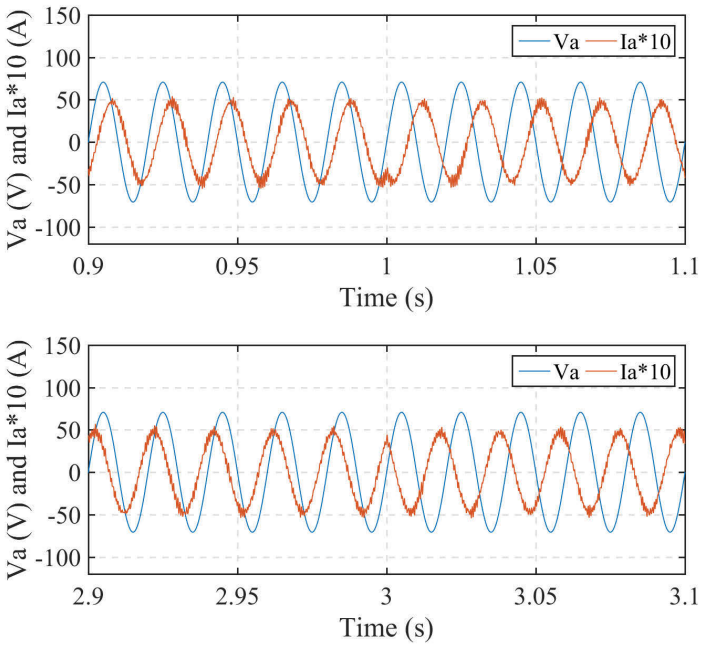

(c) Grid voltage and current performance

Figure 4.15 : Simulation results from MMPC during second scenario.

Figs. 4.10, 4.11 and 4.12 show the performances of EV charger system working under the first scenario by using the conventional DPC, proposed MPC and improved MMPC, respectively. During this operation, the system exchanges the active or reactive powers with the main grid separately. The system can work effectively with the above mentioned three methods. The battery current demand and the grid reactive requirement can be satisfied. From Figs. 4.10(b), 4.11(b) and 4.12(b), it can be seen that the active and reactive power ripples can be reduced by using the MPC and MMPC method instead of using the conventional DPC method. The ripples in the MMPC scheme are the smallest among the three methods. The grid current performance can also be improved by using the MPC and MMPC methods, as depicted in Figs. 4.10(c), 4.11(c) and 4.12(c). Since only the active power is transferred from the grid to the EV battery during the first second, the grid current is in phase with its voltage. Then the transmission direction of the active power is changed from the EV battery to the grid. Therefore, the grid current is out of phase with its voltage. During the third second, the reactive power is delivered from the grid to EV battery, which causes the grid current lagging the voltage by 90°. When the reactive power flow direction changed, the current leads its voltage by 90°.

It has been further verified through the numerical simulation when the system working under the second scenario. All the results obtained from the conventional DPC, proposed MPC and improved MMPC are shown in Figs. 4.13, 4.14 and 4.15, respectively. With these three control methods, both the battery current and grid reactive power can be controlled to track the expected values. Compared with the results from DPC, the performances of the active and reactive power and grid current are improved by using the proposed MPC and MMPC. This conclusion is in accordance with that from the previous simulation results in the first scenario.

4.6 Experimental Results

The proposed control strategy was validated by a downsized experimental setup, as shown in Fig. 4.16. The setup consists of an insulated-gate-bipolar-transistor (IGBT)-based three-phase two-stage bidirectional converter, three AC filter inductors and DC power sources. Twelve 12V24Ah sealed lead-acid batteries are connected in series to act as the EV battery. Therefore, the nominal voltage and the capacity of this sealed battery are 144 V and 24 Ah, respectively. The experimental conditions are the same as those of the simulated system, as listed in Table 4.4. The AC filter inductor was 12 mH in the experiment. The control algorithm was implemented on a dSPACE DS1104 processor board. The system was operated at 8 kHz. All the measured parameters are viewed through the dSPACE control desk. Note that during the experimental test, the battery contactors were closed prior to turning on the main power on the AC-side. Otherwise, a current spike would occur due to the difference between the IGBT output voltage (V_{dc}) and the battery voltage (V_{bat}). The conventional DPC method was applied to compare its performance with that obtained by the proposed MPC scheme. Two experimental scenarios were designed to be the same as the numerical simulation tests. One operation was that the system exchanges the active or reactive power with the main grid separately, known as the first scenario. The other working condition was that both the active and reactive power were delivered simultaneously, as in the experimental test of the second scenario.

The results in Figs. 4.17, 4.18 and 4.19 show how the system exchanges the active and reactive powers with the power grid in an independent operation of G2V, V2G and (capacitive/inductive) V4G separately. Both the active and reactive power demands can be tracked effectively by the conventional DPC, proposed MPC and MMPC schemes. In Modes I and II, since no reactive power is transferred in this

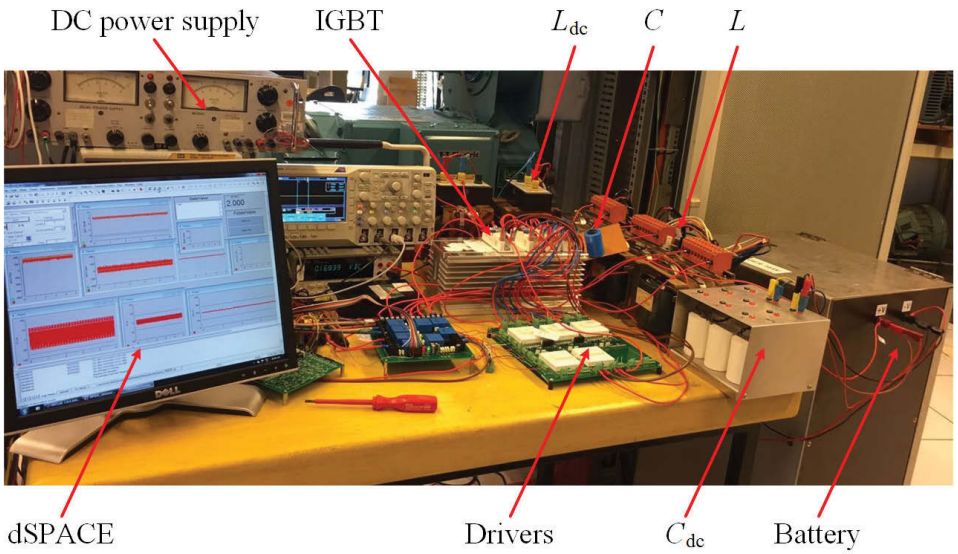

Figure 4.16 : Experimental setup.

operation, the bidirectional charger works in G2V and V2G modes, separately. As in the G2V operation mode, the grid current is in phase with the main grid voltage, which means the active power flows from the grid to the EV battery. In V2G mode, the current is out of phase with the voltage, discharging the stored energy from battery to the power grid.

In Modes III and IV, the converter compensates the reactive power to the grid without any energy transmission (V4G operation). Since there is no active power transferred, when the reactive power is delivered from the grid to the battery, the grid current is 90° lagging behind the grid voltage. Otherwise, it is 90° leading, as shown in Figs. 4.17(c), 4.18(c) and 4.19(c). The bidirectional charger responded to the new active and reactive power commands is less than one-fifth of the grid cycle in all three methods. However, the active and reactive power ripples and the current performance can be improved significantly by using the proposed MPC and MMPC, in comparison with the conventional DPC method. The MMPC scheme shows the best performance among these three methods.

The second experiment was performed to show the system dynamic and steady

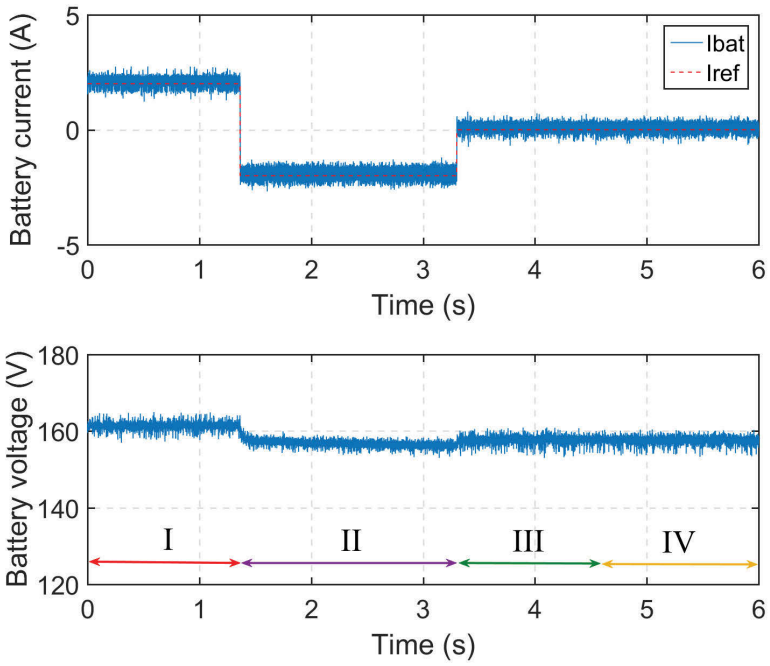

(a) Battery current and voltage performance

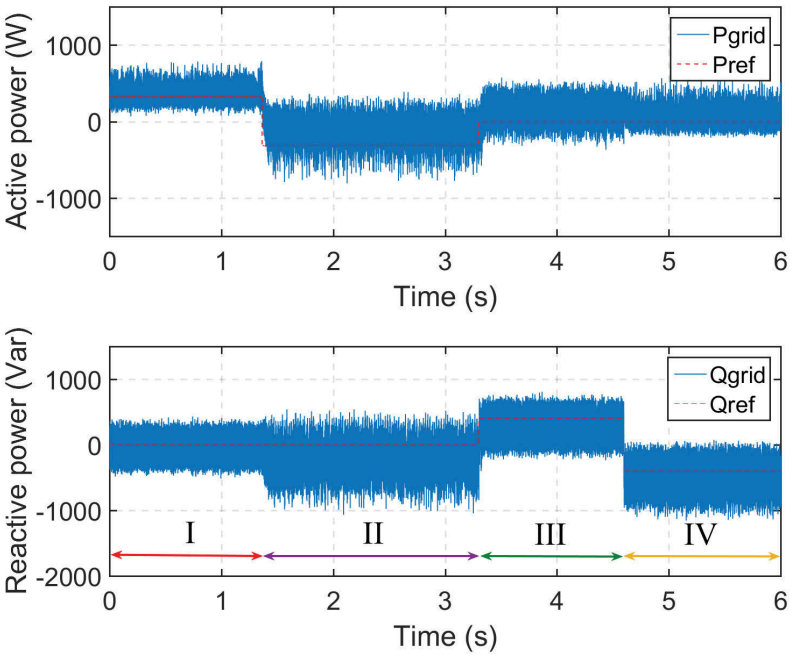

(b) Active and reactive power performance

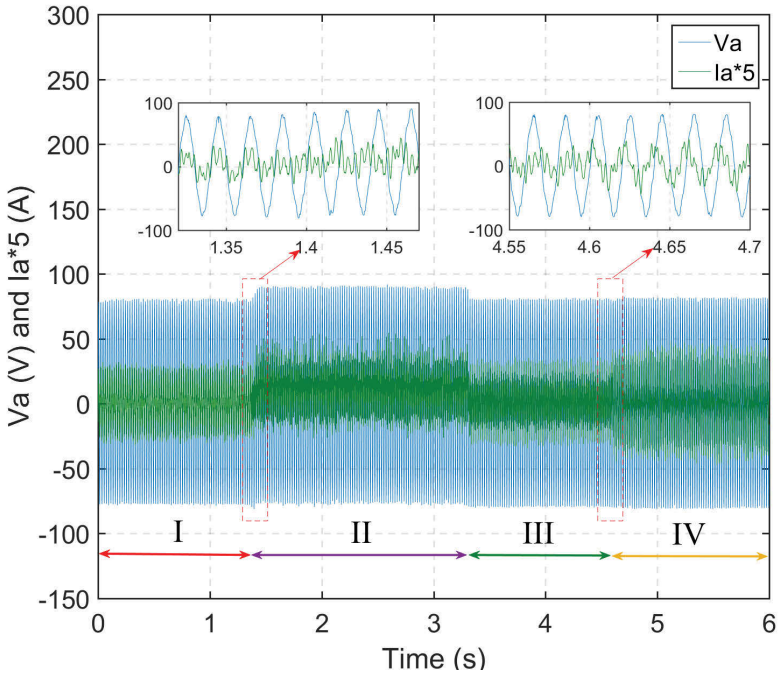

(c) Grid voltage and current performance

Figure 4.17 : Conventional DPC under exchanging active and reactive power separately operation.

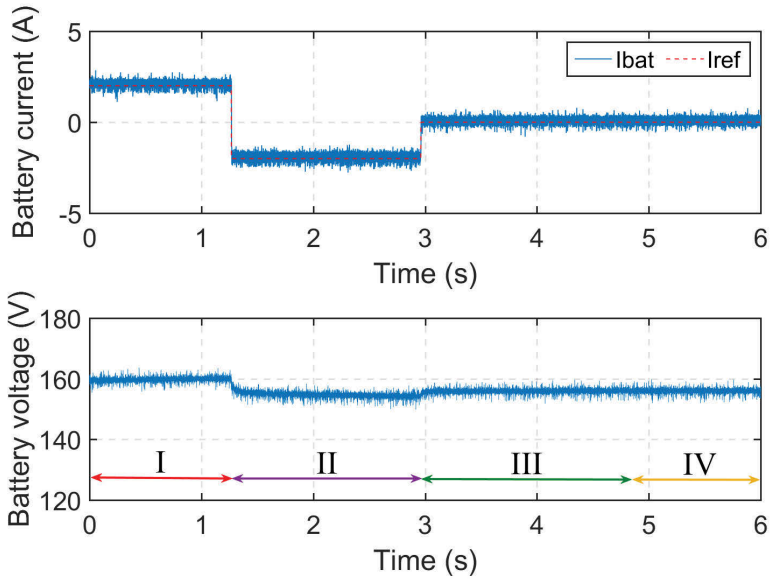

(a) Battery current and voltage performance

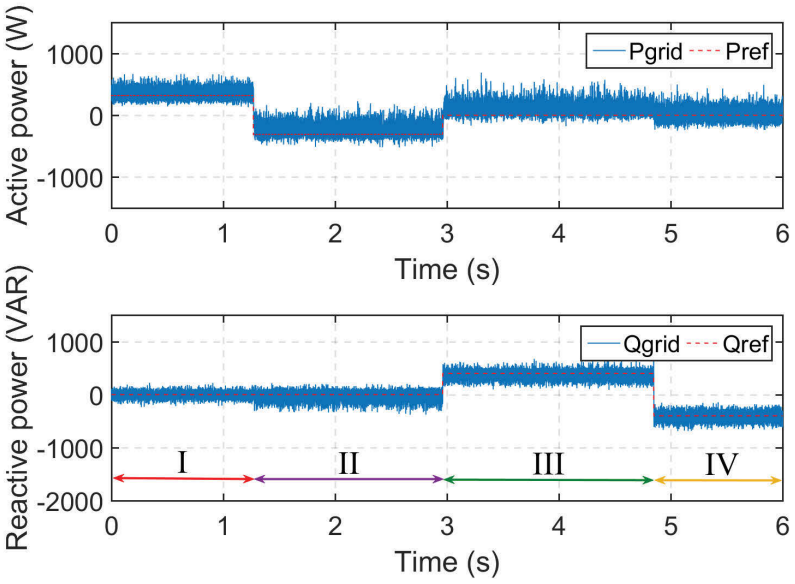

(b) Active and reactive power performance

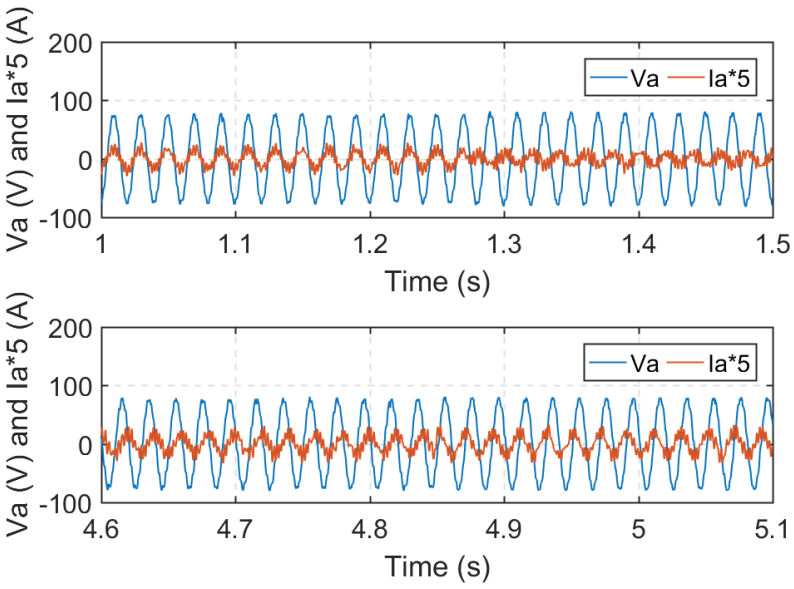

(c) Grid voltage and current performance

Figure 4.18 : Proposed MPC under exchanging active and reactive power separately operation.

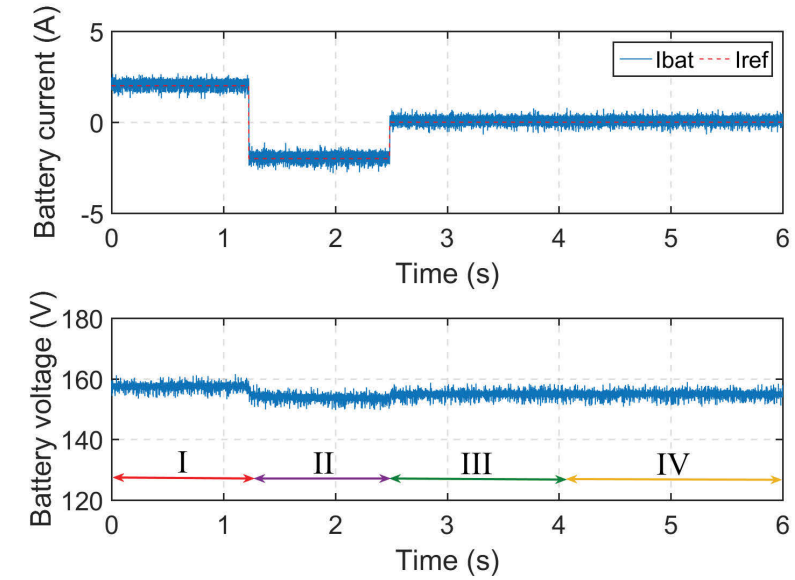

(a) Battery current and voltage performance

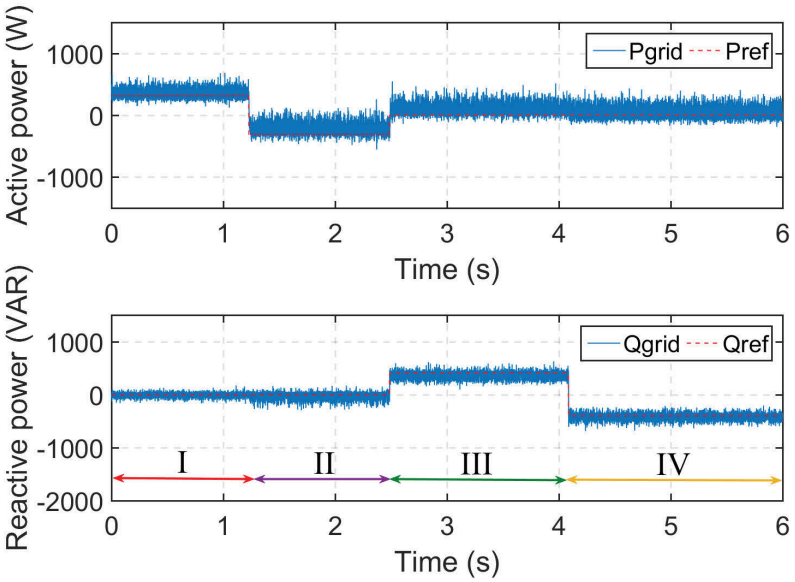

(b) Active and reactive power performance

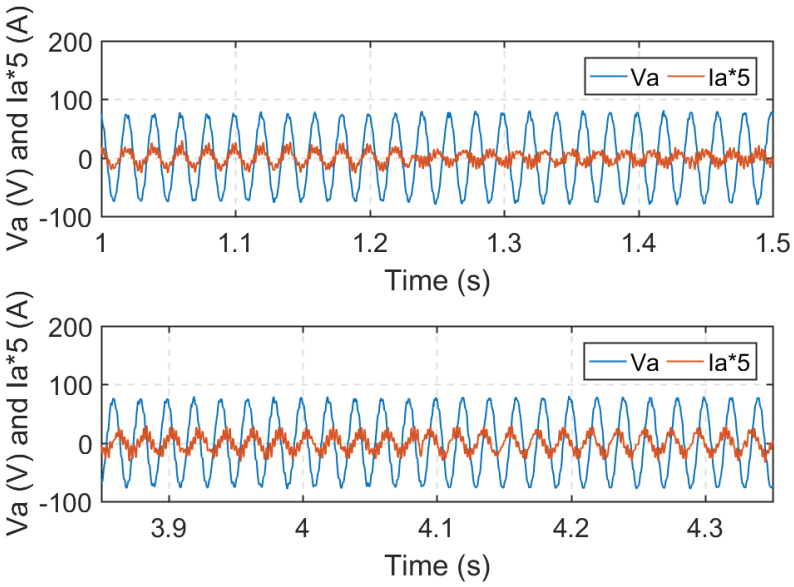

(c) Grid voltage and current performance

Figure 4.19 : Proposed MMPC under exchanging active and reactive power separately operation.

state performance in the rest regions of the PQ plane. Besides exchanging the active power, the reactive power can be supported from the charger system. As described in Figs. 4.20, 4.21 and 4.22, it can be observed clearly that all methods work effectively. The system can track the references of the active and reactive power at the same time. Figs. 4.20(a), 4.21(a) and 4.22(a) show that the battery was charged or discharged according to the EV commands with the conventional DPC, proposed MPC and MMPC methods, respectively. However, the active and reactive power ripples by using DPC are much larger than those obtained by using the proposed MPC and MMPC methods, as shown in Figs. 4.20(b), and 4.21(b) and 4.22(b).

The performance of the grid voltage and current of phase A are compared in Figs. 4.20(c), 4.21(c) and 4.22(c). In Mode V, where the charger operates in the G2V mode with inductive V4G operation, the main power grid provides the positive active and positive reactive power to the load. The grid current lags its voltage by

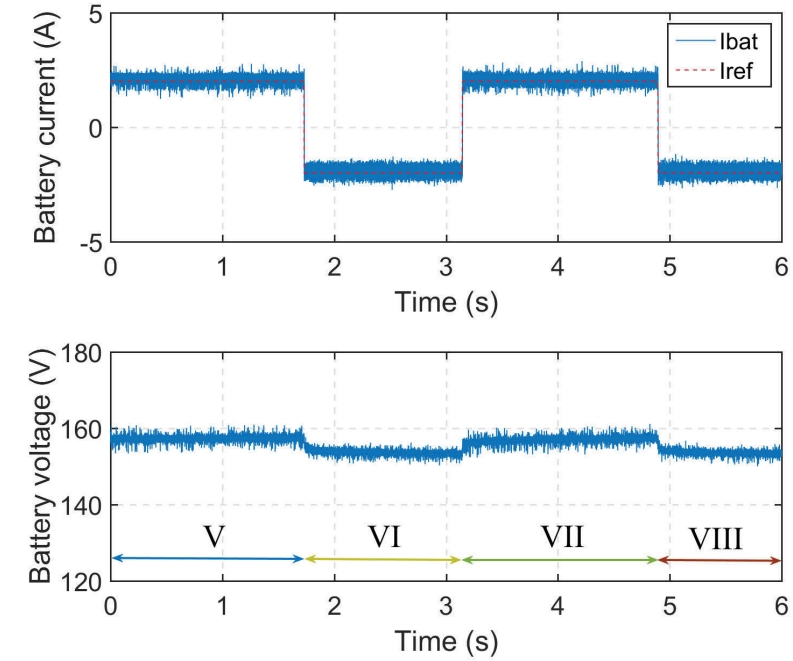

(a) Battery current and voltage performance

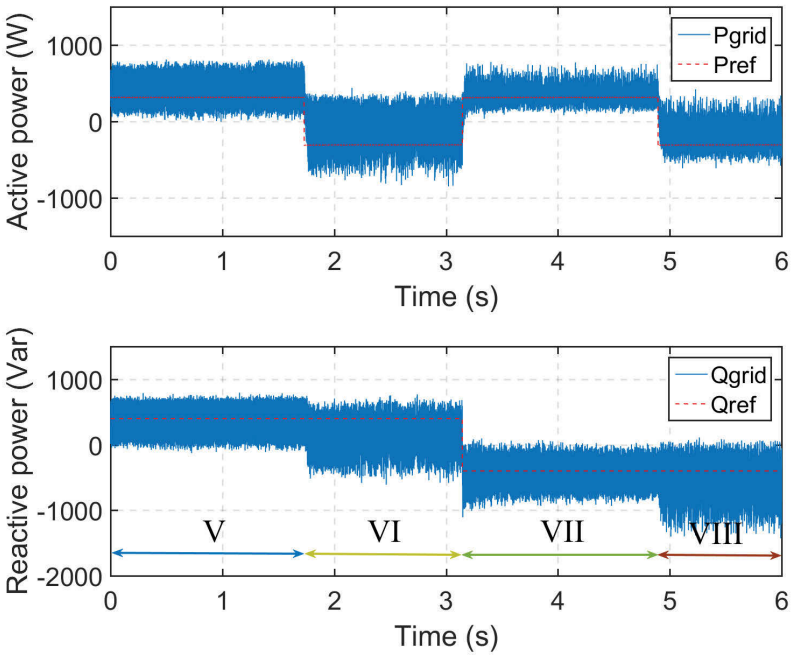

(b) Active and reactive power performance

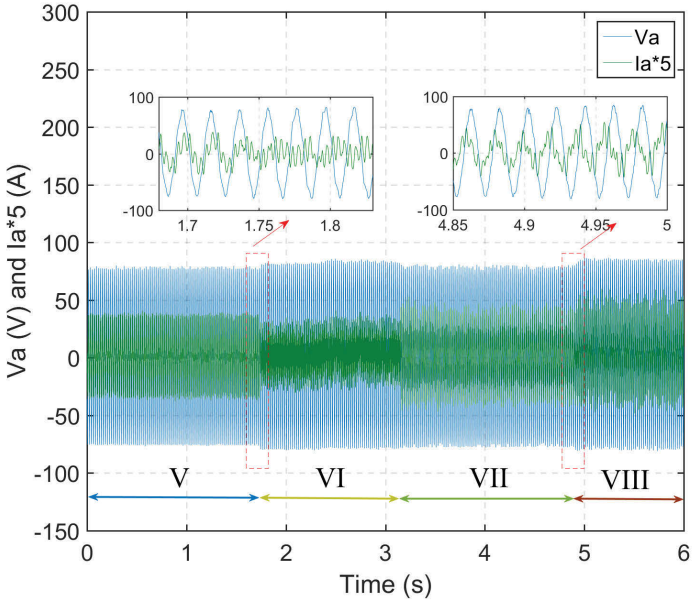

(c) Grid voltage and current performance

Figure 4.20 : Conventional DPC under exchanging active and reactive power simultaneously operation.

about 50°. When the system operates in Mode VI, delivering the active power from the EV battery to the power grid, the grid current lags its voltage by about 140°. The EV battery can be regarded as an energy storage device. With an increasing number of EVs parking, the car park can be treated as a energy storage system to support the grid. EVs are no longer a burden for the grid.

During Modes VII and VIII, the system serves as a static VAR generator to compensate the reactive power in V2G or G2V with capacitive V4G operations. The grid current i_a leads the voltage v_a by about 50° and 140° in Modes VII and VIII, respectively. The battery is charged and discharged with the specified current while producing the reactive power to the grid in this scenario. Overall, the EV charger quickly reaches the new operation points with a short dynamic response equal to approximately 2 ms with the proposed MPC method. It has been further

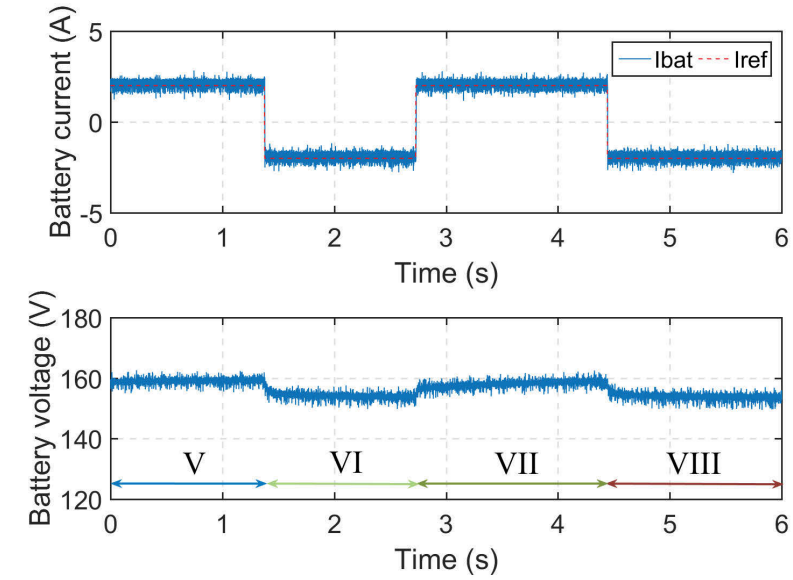

(a) Battery current and voltage performance

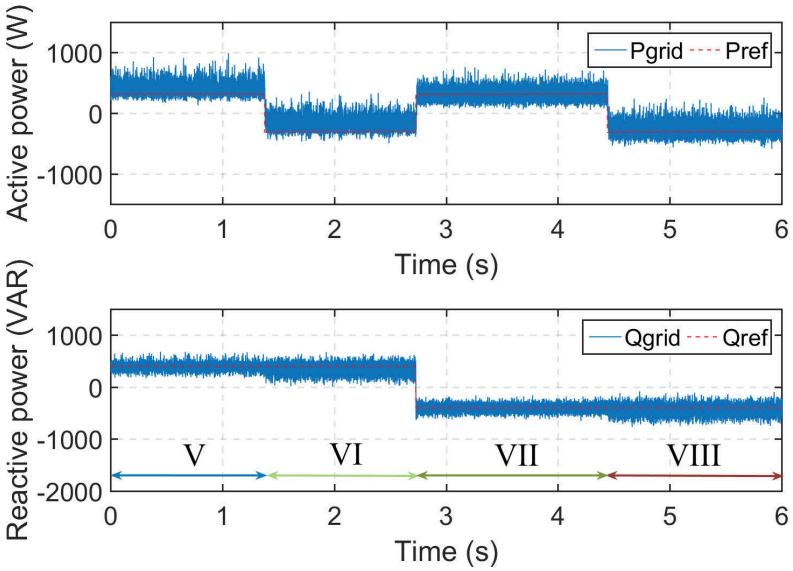

(b) Active and reactive power performance

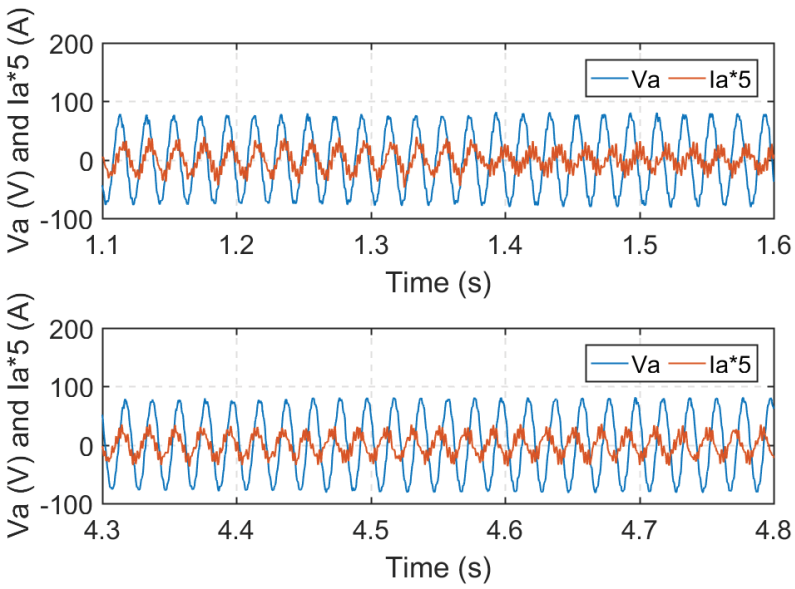

(c) Grid voltage and current performance

Figure 4.21 : Proposed MPC under exchanging active and reactive power simultaneously operation.

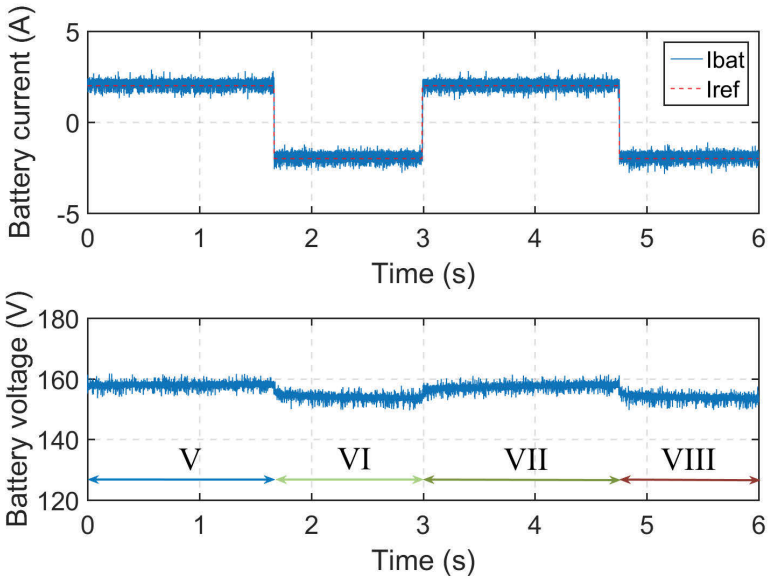

(a) Battery current and voltage performance

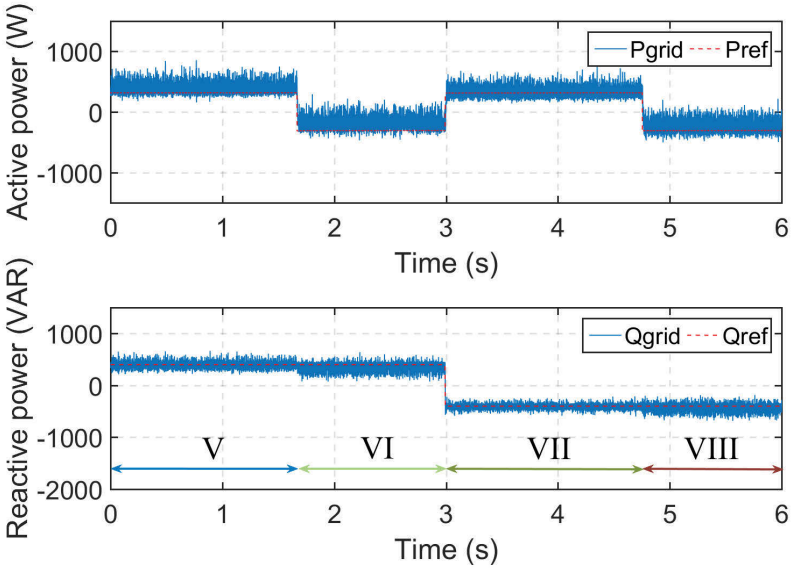

(b) Active and reactive power performance

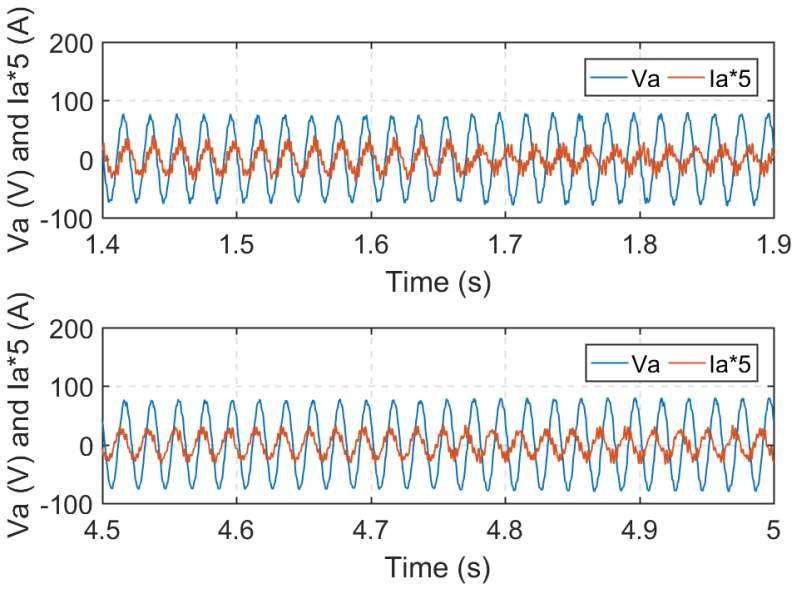

(c) Grid voltage and current performance

Figure 4.22 : Proposed MMPC under exchanging active and reactive power simultaneously operation.

verified that less active and reactive power ripples and better grid currents can be achieved with the proposed MMPC scheme.

4.7 Concluding Remarks

This chapter proposes a two-level MPC method (in four-quadrant operations) for the bidirectional battery chargers to be deployed in smart car parks. The basic operation mode includes the independent G2V, V2G and V4G operation modes, in which the EV battery can exchange active and reactive powers with the grid individually. Four innovative cooperating operation modes are proposed, namely, G2V with inductive V4G mode, V2G with inductive V4G mode, G2V with capacitive V4G mode, and V2G with capacitive V4G mode. During these operation modes, both active and reactive powers can be delivered to the grid at the same time, which means EV batteries can function as a static VAR generator while charging or discharging the batteries with the power from or to the grid.

The proposed system MPC controller receives the discharging and charging currents from the EV charging stations and active and reactive power references from the grid. A laboratory bidirectional EV battery charger prototype was developed to compare the proposed method with the conventional schemes. Compared with the PI and conventional DPC controller, the bidirectional two-stage charger using the proposed MPC method responded to the active and reactive power commands in less than one fifth of a grid cycle (around 4 ms in the case of 50 Hz). The active and reactive power ripples and the distortion of the grid current can be reduced effectively.

Then, a predictive control method with extended 20 voltage vectors, named the MMPC method, has been presented. To reduce the complexity and computational time, a pre-selection method was proposed in the MMPC scheme. As evidenced by the simulation results, both the conventional and modified MPC have a fast dynamic

performance. In terms of the steady-state performance, the proposed MMPC exhibits less ripples in the active and reactive powers and better current performance. Key experimental results were presented to validate the better stable steady-state stability and fast dynamic performance under the aforementioned operation modes.

Chapter 5

MODEL PREDICTIVE SLIDING MODE CONTROL

5.1 Introduction

Three-phase switching AC/DC converters have recently attracted significant attention because of their abilities to achieve bidirectional power flow, low harmonic line current, controllable power factor, and good DC-link voltage regulation [24]. They are the preferred converter topology in many industrial power systems [91], and have found extensive applications, such as railway electrification systems [92], renewable energy systems (wind power generation) [93], smart micro grids [94], and DC transmission systems [95]. Various advanced converter control strategies for three-phase AC/DC converters have been proposed [96, 97]. Remarkably stable and efficient schemes are employed to improve the power quality and reduce the effects caused by unexpected disturbances [98, 99]. Some good examples are voltage oriented control (VOC), direct power control (DPC) and model predictive control (MPC) which have been extensively and systematically studied.

Based on a converter system model in the rotational frame ($d-q$ coordinate), the classic VOC method applies the PWM to control the active and reactive powers to track their references asymptotically [100]. Since most pulse width modulation (PWM) methods ensure the harmonics on the output side, the converter input current ripple might be introduced, as well as the power ripples [101, 102]. A voltage outer loop and a current inner loop are also included in this scheme, and proportioanl integral (PI) controllers are used in these two loops because of their simple

structures. However, another drawback of this strategy is that the corresponding performances are highly dependent on the PI parameters and the current loop [103]. The stability and dynamic performance will be limited by the fixed PI parameters during disturbances. Controlling the active and reactive power through a switching table, the DPC scheme does not require the internal current control loop and PWM modulator block [104]-[105]. Due to the difficulty in constructing a perfect heuristic table, the DPC method is also susceptible to producing large power ripples which would impact the system steady state performance [106].

Compared with the above two methods, the MPC method is a model-based control technique which provides fast demand tracking speed and low power ripples [107, 108]. This method has several advantages, such as: it is free of modulation, and has simple inclusion of system parameters, constraints and demands in the algorithm [109]. For a 2-level converter, MPC is devised to select an optimal switching state from eight possible states to obtain an optimal voltage vector. Based on the system model, a cost function is designed to minimize the errors between the references and the real-time acquisitions of the controlled variables. In a standard MPC strategy, a PI controller is used to generate the active power reference which will be transferred to the cost function. The PI controller gains by this model predictive PI control (MPPIC) scheme should be tuned and adjusted in an ad-hoc manner to satisfy the latest system demands and unknown disturbances. However, the PI parameters are constant and fixed during the operation. It is hard for them to be tuned automatically according to the latest system objectives and the updated load demand.

In order to solve this problem, a sliding mode control (SMC) scheme is considered to improve both the dynamic and steady state performances. SMC is known for its excellent dynamic response and strong robustness to disturbances and uncertainties, such as unknown variations of control variables and system parameters [110, 111,

112]. As an effective nonlinear control technique, a control signal is employed to guide the system trajectory points onto a surface, known as the sliding surface or hyper plane. All the trajectory points will be forced to the vicinity of the sliding surface within a finite time and towards the system equilibrium point thereafter [113]. During the operation of unknown uncertainties, a control law is designed to maintain the control variables on the sliding surface [114]. In addition, SMC is simple to implement and execute. Since the system parameters are required in designing the controller and the controller law, system parameter identification plays a vital role in the SMC. When controlling a complex system, it might be difficult to get highly accurate system parameters. The system performance, including the dynamic response and steady state error, will then be affected by these incorrect or inaccurate parameters. This problem mainly occurs in some complex systems or topologies where accurate system models or parameters are hard to get or predict. The system studied in this chapter, an AC/DC three-phase two-level converter connected with a resistive load, as shown in Fig. 5.1, is a simple system whose parameters can be accurately measured. Also, because of the use of space voltage vectors, the switching frequency of MPC is not constant.

This chapter presents an MPC scheme cooperating with a SMC strategy, named the model predictive sliding mode control (MPSMC), to compensate for the weakness of the standard MPC method using a PI controller. The SMC technique is employed to track the active power reference to improve system dynamic and robustness performance.

5.2 System Model

Fig. 5.1 illustrates the power circuit of a three-phase AC/DC converter, consisting of six IGBT switches, S_i (i = 1, 2, $\cdots$, 6). The main grid adopts the symmetrical three-phase three-wire system, connected with this IGBT full bridge through three

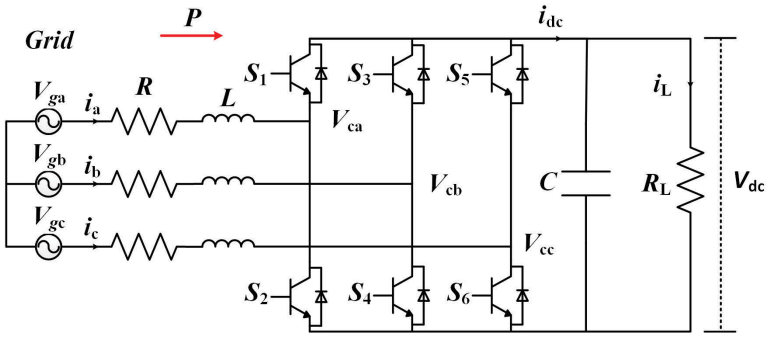

Figure 5.1 : Topology of a three-phase AC/DC converter.

series filter inductors with the same value, L, and resistors with the same value, R. A capacitor, C, is connected on the DC side to filter the voltage harmonics.

The mathematical model of the AC/DC converter in the *abc* frame can be expressed as

$$\begin{bmatrix} L\frac{di_a}{dt} \\ L\frac{di_b}{dt} \\ L\frac{di_c}{dt} \\ C\frac{dV_{dc}}{dt} \end{bmatrix} = \begin{bmatrix} -R & 0 & 0 & 0 \\ 0 & -R & 0 & 0 \\ 0 & 0 & -R & 0 \\ S_a & S_b & S_c & -1 \end{bmatrix} \begin{bmatrix} i_a \\ i_b \\ i_c \\ i_L \end{bmatrix} + \begin{bmatrix} v_{ga} - v_{ca} \\ v_{gb} - v_{cb} \\ v_{gc} - v_{cc} \\ 0 \end{bmatrix}, \tag{5.1}$$

where v_{ga}, v_{gb}, and v_{gc} are the grid phase voltages; i_a, i_b, and i_c the input currents of the converter; v_{ca}, v_{cb}, and v_{cc} the converter input voltages; v_{dc} is the DC output voltage; i_L the load current; S_a, S_b, and S_c stand for the switching state of the switches, respectively, and

$$S_k = \begin{cases} 1, & \text{upper switch on phase k is on} \\ 0, & \text{upper switch on phase k is off} \end{cases}. \tag{5.2}$$

For example, $S_a = 1$ means S_1 on and S_2 off.

The switching state can be expressed in the two-phase stationary $\alpha\beta$ orthogonal

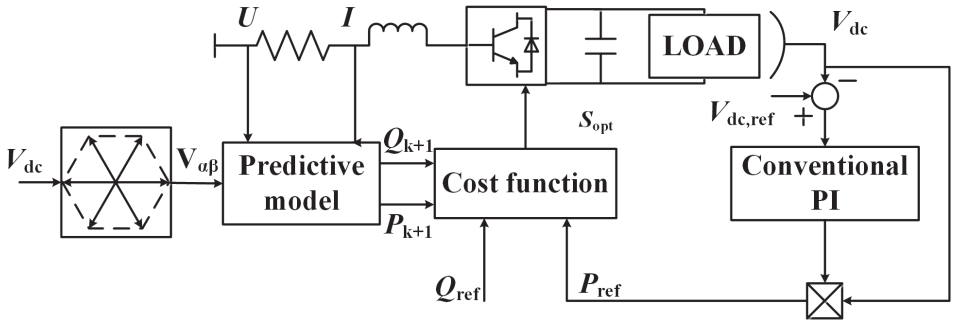

Figure 5.2 : Basic principle of MPPIC method.

coordinate system as

$$\mathbf{S}_{\alpha\beta} = \begin{bmatrix} S_\alpha \\ S_\beta \end{bmatrix} = \frac{2}{3} \begin{bmatrix} 1 & -\frac{1}{2} & -\frac{1}{2} \\ 0 & \frac{\sqrt{3}}{2} & -\frac{\sqrt{3}}{2} \end{bmatrix} \begin{bmatrix} S_a \\ S_b \\ S_c \end{bmatrix}. \tag{5.3}$$

Based on the analysis in Chapter 4, the dynamic model of the AC/DC converter can be expressed with $\alpha\beta$-axes components, as

$$\begin{bmatrix} v_{g,\alpha} \\ v_{g,\beta} \end{bmatrix} = \begin{bmatrix} L & 0 \\ 0 & L \end{bmatrix} \begin{bmatrix} \frac{di_{g,\alpha}}{dt} \\ \frac{di_{g,\beta}}{dt} \end{bmatrix} + \begin{bmatrix} R & 0 \\ 0 & R \end{bmatrix} \begin{bmatrix} i_{g,\alpha} \\ i_{g,\beta} \end{bmatrix} + \begin{bmatrix} v_\alpha \\ v_\beta \end{bmatrix}. \tag{5.4}$$

5.3 Model Predictive Control

The main purpose of MPC used in this chapter is to control the active and reactive power flow to the desired values and in the desired directions, in addition to the output voltage regulation. In the MPPIC scheme, a PI controller is applied to track the DC-link voltage to generate the active power reference, as shown in Fig. 5.2.

In the form of a space vector equation, (5.4) can be rewritten as

$$\dot{\mathbf{X}} = A\mathbf{X} + Bv_{g,\alpha\beta} + Dv_{\alpha\beta}. \tag{5.5}$$

where

$$\mathbf{X} = \mathbf{i}_{\mathbf{g},\alpha\beta} = \begin{bmatrix} i_{g,\alpha} \\ i_{g,\beta} \end{bmatrix}, A = \begin{bmatrix} -\frac{R}{L} & 0 \\ 0 & -\frac{R}{L} \end{bmatrix}, B = \begin{bmatrix} \frac{1}{L} \\ 0 \end{bmatrix}, D = \begin{bmatrix} -\frac{1}{L} \\ 0 \end{bmatrix}.$$

The discrete-time model of the grid current at (k+1)th instant for a sample time T_s can be expressed as

$$\mathbf{i}_{\mathbf{g},\alpha\beta}(k+1) = \frac{T_s}{L}(\mathbf{v}_{\mathbf{g},\alpha\beta}(k) - R\mathbf{i}_{\mathbf{g},\alpha\beta}(k) - \mathbf{v}_{\alpha\beta}(k)) + \mathbf{i}_{\mathbf{g},\alpha\beta}(k). \tag{5.6}$$

Then, the active and reactive powers of this system can be calculated by

$$\begin{cases} P = \frac{3}{2}\mathrm{Re}\{v_g i_g^*\} = \frac{3}{2}(v_{g,\alpha} i_{g,\alpha} + v_{g,\beta} i_{g,\beta}), \\ Q = \frac{3}{2}\mathrm{Im}\{v_g i_g^*\} = \frac{3}{2}(v_{g,\beta} i_{g,\alpha} - v_{g,\alpha} i_{g,\beta}). \end{cases} \tag{5.7}$$

For the active and reactive power control, the cost function J can be defined with a measurement of predicted input error, as

$$J = \sqrt{(P - P_{ref})^2 + (Q - Q_{ref})^2}, \tag{5.8}$$

where P_{ref} and Q_{ref} are the active and reactive power references, respectively.

It can be seen from (5.6) that the eight voltage vectors of the converter input voltage result in eight vectors of line current $i_{g,\alpha\beta}$. Substituting (5.6) into (5.7), one can deduce eight possible values for the active and reactive powers. The cost function is employed to select the optimal voltage space vector that yields the P and Q with the minimum value of cost function J, and this optimal switching vector (S_{opt} in Fig. 5.2) is then applied for the next step switching.

5.4 Proposed MPSMC Scheme

The traditional PI controller has only one single set of unchangeable controller parameters during the operation. The system will suffer from slow dynamic performance when the system parameters and demands vary. On the contrary, the SMC

has excellent dynamic performance since the controller and the control law are both based on the system model. Taking advantage of this feature, the proposed MPSMC method applies a sliding model controller to replace the PI controller. The control problem is to detect an appropriate control law so that the system state can track the expected active power and desired DC-link voltage.

From Fig. 5.1, the instantaneous power (P_i) conservation equation is used to describe the dynamic process of DC-link voltage, which is

$$P_i = V_{dc} i_{dc} = C V_{dc} \frac{dV_{dc}}{dt} + \frac{V_{dc}^2}{R_L}. \tag{5.9}$$

By the principle of power equilibrium, the input instantaneous power of the converter is equal to its instantaneous output power. The converter power loss is neglected in this thesis. In the steady state, the instantaneous power is equal to the active power, which is proportional to the voltage on the DC side. Therefore, in order to control the active power, the objective of the SMC can be converted to control the DC-link voltage.

5.4.1 Active power sliding surface

The control problem in the converter is to find a suitable control law so that the control variable V_{dc} can track the expected demand $V_{dc,ref}$ accurately. To achieve this control target, the tracking error e_v can be defined as

$$e_v = V_{dc} - V_{dc,ref}. \tag{5.10}$$

To design the sliding surface, methods include a proportional of the error and a combination of the proportional and integral of the error. In this chapter, to control the steady state error to be zero, a linear combination of proportional error and the integral of the designed voltage error is selected as the sliding surface [115]-[117], that is

$$S_v = k_1 e_v + k_2 \int e_v dt = \lambda e_v + \int e_v dt = 0, \tag{5.11}$$

where λ ($\lambda = k_1/k_2$) is a positive constant related to the time constant of the output voltage. Therefore, the response speed increases as λ is decreased, an idea originaing from [118] but modified for the proposed controller. With such a relationship, a proper λ can be selected to optimize the dynamic and steady state performances of the control system, such as the settling time, overshoot/undershoot, steady state error, and control robustness.

Taking the derivative of S_v with respect to time and substituting (5.10) into (5.11), one obtains

$$\dot{S}_v = \lambda(\dot{V}_{dc} - \dot{V}_{dc,ref}) + V_{dc} - V_{dc,ref}. \tag{5.12}$$

5.4.2 Active power control law

According to the inherent uncertainty with respect to the active power in this system, the control law can be designed as

$$u = \begin{cases} P_{dc}^{+}(t), & S_v > 0, \\ P_{dc}^{-}(t), & S_v \leq 0. \end{cases} \tag{5.13}$$

where u is the control law, and $P_{dc}^{+}(t)$ and $P_{dc}^{-}(t)$ represent the instantaneous power when the sliding variable reaches different sides of the sliding-mode surface S_v, respectively. Fig. 5.3 depicts the control block diagram of the proposed MPSMC scheme.

According to (5.9) and (5.13), the first-order derivative of DC-link voltage versus time can be expressed as

$$\dot{V}_{dc} = \frac{u}{CV_{dc}} - \frac{1}{R_L C}V_{dc} + \delta, \tag{5.14}$$

where δ is called the uncertainty disturbance on V_{dc}.

Here, the bound of the uncertainty disturbance, ρ, is assumed to be $|\delta| \leq \rho < 1$, i.e. ρ is a given positive constant.

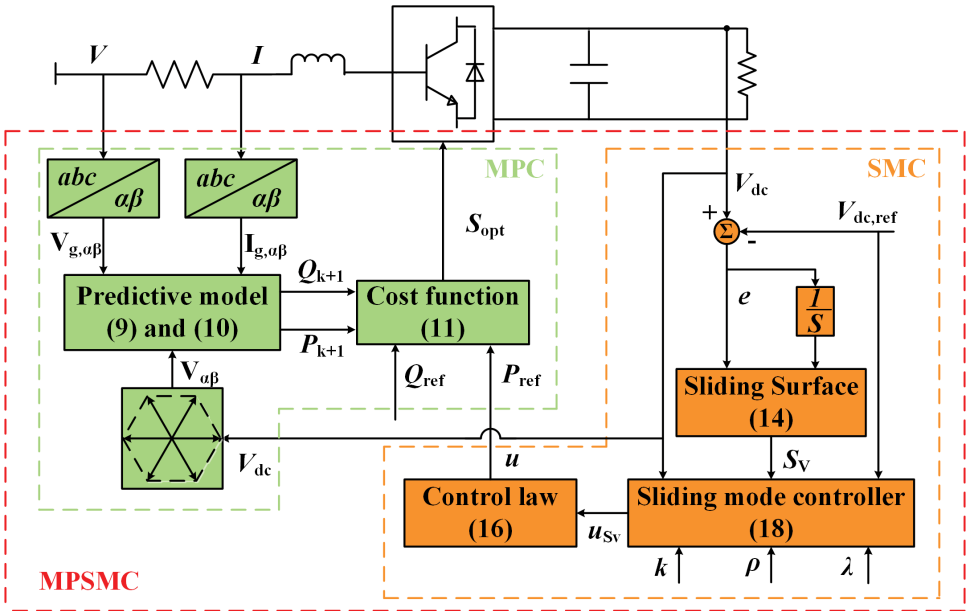

Figure 5.3 : Basic principle of the proposed MPSMC method.

Based on the aforementioned analysis, the controller can be designed as

$$u_{S_v} = CV_{dc}\left[(\frac{1}{R_L C} - \frac{1}{\lambda})V_{dc} + \frac{1}{\lambda}V_{dc,ref} - (\rho + k)\text{sign}(S_v)\right], \tag{5.15}$$

where $k > 0$ represents a suitable control gain.

5.4.3 Proof of existence condition

All the trajectory points in the vicinity of the sliding surface should reach to the designed sliding surface within a finite time [117, 119]. To guarantee this existence condition, one only needs to show that

$$\lim_{S_v \to 0} S \cdot \dot{S} < 0. \tag{5.16}$$

Substituting (5.14) and (5.15) into (5.12) yields

$$\dot{S}_v = -\lambda\left[(\rho + k)\text{sign}(S_v) - \delta\right]. \tag{5.17}$$

Multiplying S_v by (5.17), one obtains the sliding-mode existence condition as

follows

$$\begin{aligned} S_v\dot{S}_v &= S_v(-\lambda((\rho+k)\text{sign}(S_v)-\delta)) \\ &= -\lambda k|S_v| - \lambda S_v(\rho\text{sign}(S_v)-\delta). \end{aligned} \tag{5.18}$$

Therefore, the existence condition of the sliding mode can be satisfied with the following two cases [120].

Case 1: If the reaching point is in a positive position in the neighbourhood field of the created switching surface S_v, i.e., $S_v > 0$,

$$\begin{aligned} S_v\dot{S}_v &= -\lambda k|S_v| - \lambda S_v(\rho\text{sign}(S_v)-\delta) \\ &= -\lambda k|S_v| - \lambda S_v(\rho-\delta) \\ &< -\lambda k|S_v| \\ &< 0. \end{aligned} \tag{5.19}$$

This leads to

$$\lim_{S_v\to 0^+} S_v\dot{S}_v < 0. \tag{5.20}$$

Case 2: If the reaching point is in a negative position in the neighborhood field of the created switching surface S_v, i.e., $S_v < 0$,

$$\begin{aligned} S_v\dot{S}_v &= -\lambda k|S_v| - \lambda S_v(\rho\text{sign}(S_v)-\delta) \\ &= -\lambda k|S_v| + \lambda S_v(\rho+\delta) \\ &< -\lambda k|S_v| \\ &< 0. \end{aligned} \tag{5.21}$$

This results in

$$\lim_{S_v\to 0^-} S_v\dot{S}_v < 0. \tag{5.22}$$

From (5.20) and (5.22), one can conclude that (5.16), the existence condition, can be satisfied by selecting the proper sliding coefficients, λ and k.

5.4.4 Proof of tracking condition

The tracking condition of the sliding mode can be derived by applying the Lyapunov stability analysis [87, 114]. For this analysis, a Lyapunov function candidate is designed as

$$V_{S_v}(V_{dc}) = \frac{S_v^2}{2}. \tag{5.23}$$

It is positive for any reaching points, except for the equilibrium point $V_{dc} = V_{dc,ref}$. Only when the sliding variable reaches the equilibrium point, will the Lyapunov function V_{S_v} be zero. Hence, the proposed Lyapunov function V_{S_v} is positive definite.

Based on (5.20) and (5.22), the derivative of V_{S_V} with respect to time can be obtained as

$$\dot{V}_{S_v}(V_{dc}) = S_v \dot{S}_v < 0. \tag{5.24}$$

Therefore, the derivative of V_{S_v} is negative definite.

Theorem: If a Lyapunov function V is positive definite and its derivative is negative definite, the system is asymptotically stable at the equilibrium point.

As a result, the designed Lyapunov function V_{S_v} complies with the robustness of Lyapunov stability analysis. Moreover, the system stabilises at the equilibrium point ($V_{dc,ref}$), which can be expressed as

$$P_{ac} = P_{dc} = V_{dc} I_{dc} = \frac{V_{dc,ref}^2}{R_L}. \tag{5.25}$$

Substituting (5.15) into (5.14) reveals that when the system trajectory points reach the sliding surface, i.e., $S_v = 0$, the uncertainty disturbance is equal to zero as well, i.e., $\delta = 0$. Then, the first-order derivative of the voltage error with respect to time can be rewritten as

$$\dot{e}_v = \dot{V}_{dc} - \dot{V}_{dc,ref} = -\frac{1}{\lambda}(V_{dc} - V_{dc,ref}). \tag{5.26}$$

According to (5.26), as long as the sliding coefficient λ is positive, the trajectory points can keep stable at the sliding surface theoretically. However, as the AC/DC converter is a nonlinear system, a positive λ can hardly guarantee all the reaching points satisfy the stability condition, except for those points from the vicinity of the stability field. By applying the MPC and SMC schemes simultaneously in this system, all the trajectory points can hit and remain stable at the designed sliding surface only when λ is chosen from an inherent range of the analyzed set, i.e., $\lambda > 0$.

Based on the aforementioned analysis, the nonlinear criteria to choose the switching state should be as follows,

(1) $V_{dc} > V_{dc,ref} \Rightarrow \dot{V}_{dc} < 0 \Rightarrow$ choose a switching state suitable to decrease V_{dc},

(2) $V_{dc} < V_{dc,ref} \Rightarrow \dot{V}_{dc} > 0 \Rightarrow$ choose a switching state suitable to increase V_{dc},

(3) $V_{dc} = V_{dc,ref} \Rightarrow \dot{V}_{dc} = 0 \Rightarrow$ choose a switching state which does not significantly change V_{dc}.

5.5 Numerical Simulation

5.5.1 Converter parameters

This section provides the simulation results obtained from the standard MPPIC and the proposed MPSMC schemes. The simulations have been carried out in a MATLAB/Simulink environment with a detailed AC/DC converter configuration, as shown in Fig. 5.4. Table 5.1 shows the simulation operation and electric parameters of the converter. It should be noted that when the desired DC-link voltage is 150 V and the resistance load is 140 , it leads to an active power equal to 161 W. The reference of the reactive power Q_{ref} is set to be 0 VAR during all the simulation testing to ensure a unity power factor operation. Note that taking the overshoot and response time into consideration, a properly paired PI parameters is chosen in the following simulation and experimental tests.

Table 5.1 :

Electric parameters of the AC/DC converter.

Symbol	Quantity	Value
L	Filter inductance	20 mH
C	Filter capacitor	680 μF
R_L	Load resistance	140 Ω
V_{LL}	Grid line-line voltage (RMS)	50 V
f	Grid frequency	50 Hz
V_{dc}	DC output voltage	150 V
T_s	Sample time	50 μs

5.5.2 Start-up dynamic and steady state performance

Fig. 5.4 shows the start-up and steady-state responses of the converter by the MPSMC and MPPIC methods, respectively, to regulate the DC-link voltage at 150 V. As shown in Fig. 5.4(a), both methods can control the voltage to the reference value as required, but the converter controlled by MPSMC can track the reference voltage much faster than that controlled by MPPIC. The settling time, which is defined as the time required to reach zero steady state error, is about 0.03 s under MPSMC, which is only 8.57% of 0.35 s, the settling time under MPPIC. Compared with the 9.13% output voltage overshoot obtained by the conventional MPPIC scheme, the output voltage overshoot can be almost eliminated by using MPSMC.

As also shown in Fig. 5.4(b), the active power under MPSMC responds much

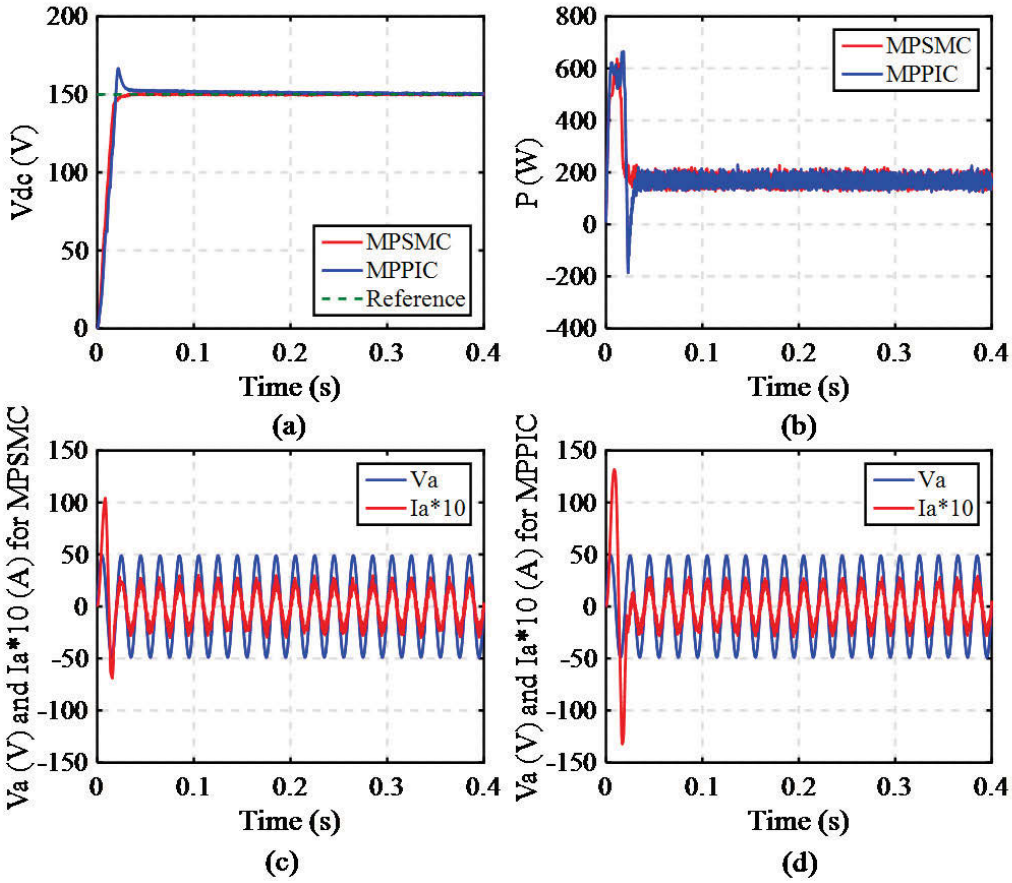

Figure 5.4 : Steady and dynamic performances, where (a) DC voltage, (b) Active power, (c) Instantaneous voltage and current of phase A in MPSMC, and (d) Instantaneous voltage and current of phase A in MPPIC.

faster than that under MPPIC, and has almost no undershoot, while both MPSMC and MPPIC deliver similar steady performance. Figs. 5.4(c) and (d) illustrate the performances of phase A grid current under MPSMC and MPPIC, respectively. The AC current under MPSMC takes around one cycle time to reach the steady state, whereas the conventional MPPIC algorithm uses about 1.50 cycle time to reach steady state with an overshoot much bigger than that under MPSMC. The AC current responding speed has been increased by approximately one third.

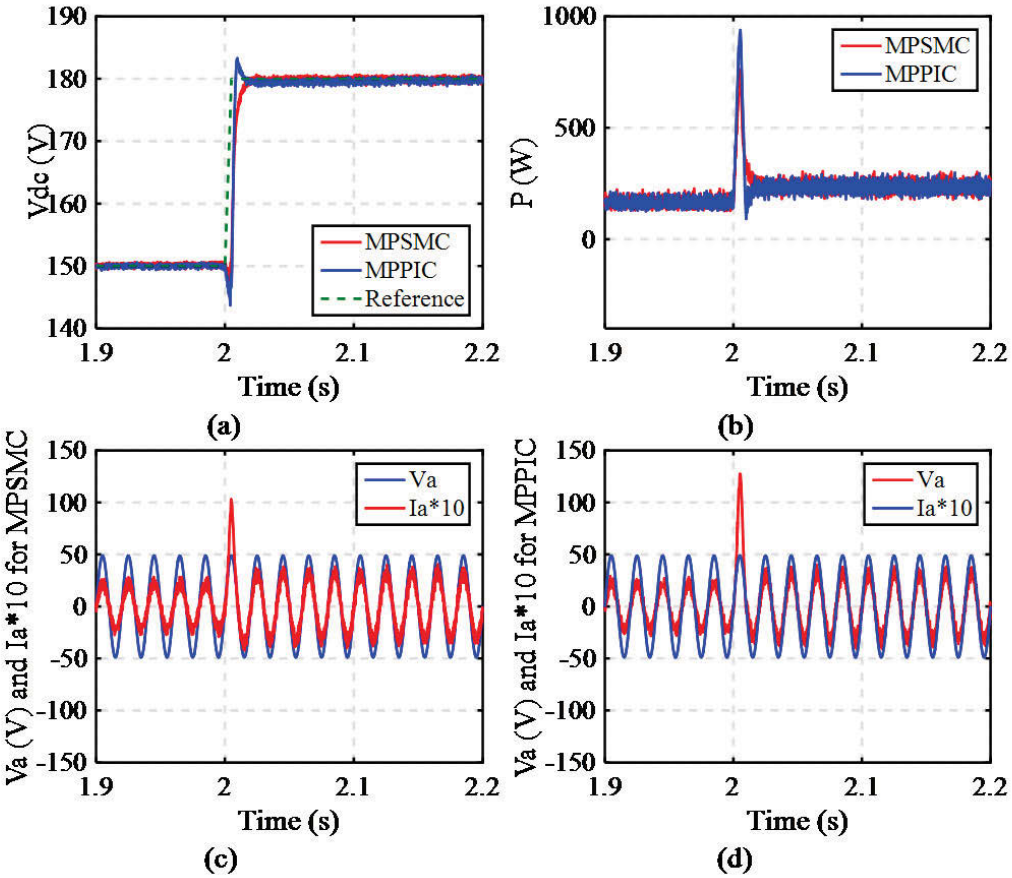

Figure 5.5 : Unexpected DC Voltage demand increase condition, where (a) DC voltage, (b) Active power, (c) Instantaneous voltage and current of phase A in MPSMC, and (d) Instantaneous voltage and current of phase A in MPPIC.

5.5.3 Operation under load voltage demand variation

Fig. 5.5 shows the dynamic performances to an unexpected increase of DC voltage demand under MPSMC and MPPIC, separately. The DC-link voltage is stepped up from 150 to 180 V at t = 2 s. As shown in Fig. 5.5(a), under the standard MPPIC, it takes 0.10 s to reach the new operation state with no steady state error, which is almost three times longer than that under the proposed MPSMC. On the other hand, the DC-link voltage tracks the reference value with almost no overshoot under MPSMC, while under MPPIC there is an apparent overshoot of 1.78%.

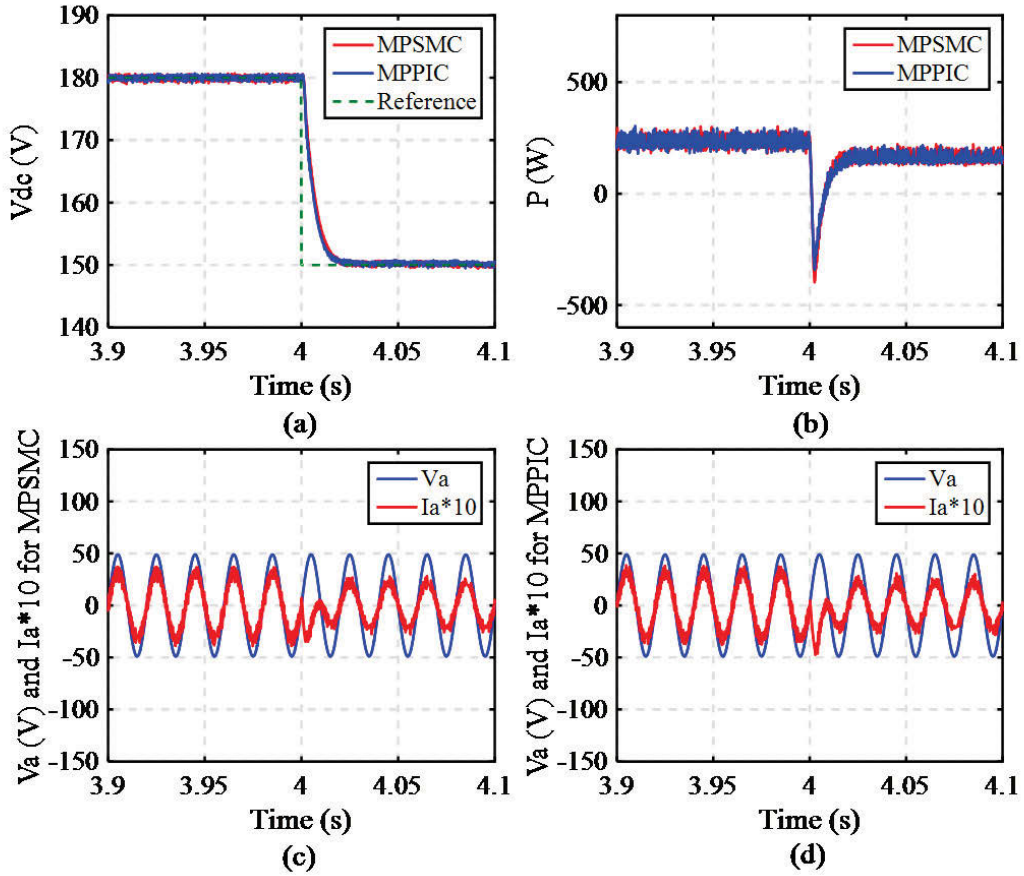

Figure 5.6 : Unexpected DC Voltage demand decrease condition, where (a) DC voltage, (b) Active power, (c) Instantaneous voltage and current of phase A in MPSMC, and (d) Instantaneous voltage and current of phase A in MPPIC.

Fig. 5.5(b) shows the much faster active power dynamic response before reaching the steady state value of 131 W under MPSMC than that under MPPIC. Figs. 5.5(c) and (d) present similar dynamic and steady state performances of AC currents obtained from both algorithms, respectively.

Compared to the response when a step change is applied to the DC voltage, similar dynamic and steady state performances can also be achieved when a sudden drop in voltage is imposed. In Figs. 5.6(a) and (b), both the DC voltage and active power obtained from the proposed MPSMC and the standard MPPIC schemes can

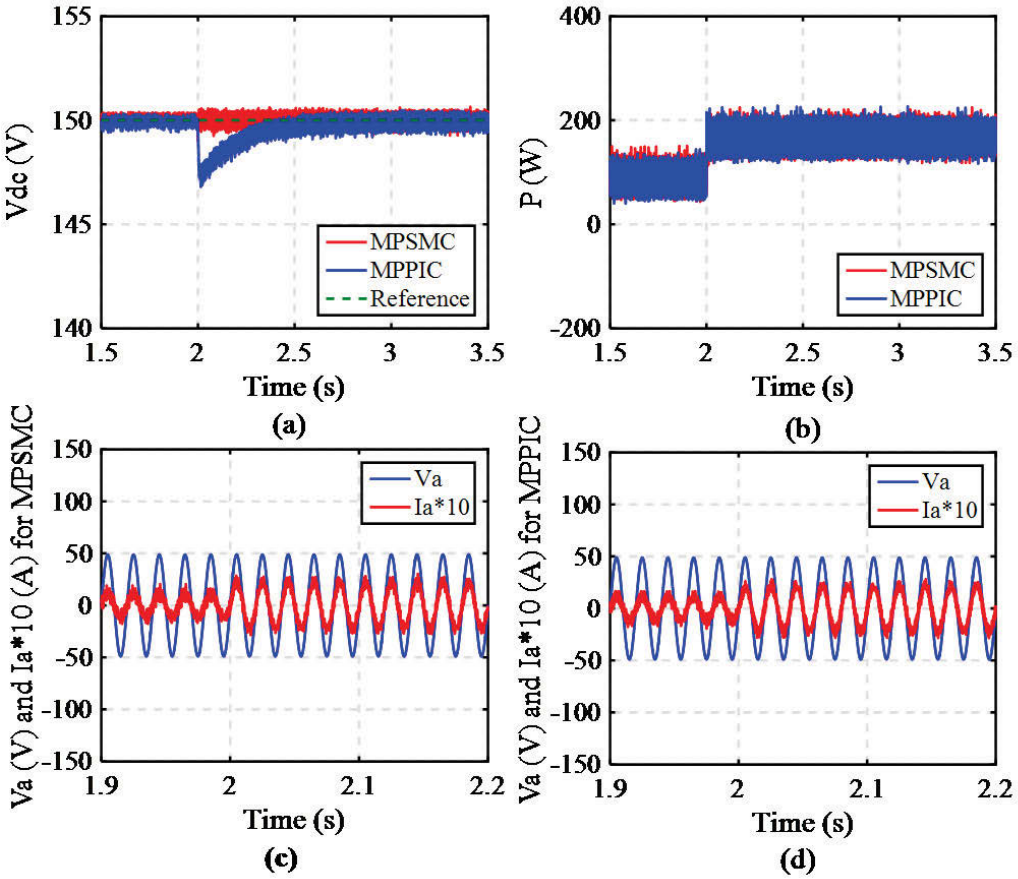

Figure 5.7 : Unexpected load variation condition, where (a) DC voltage, (b) Active power, (c) Instantaneous voltage and current of phase A in MPSMC, and (d) Instantaneous voltage and current of phase A in MPPIC.

track the reference values and reach the updated steady states. Figs. 5.6(c) and (d) show the similar dynamic performances of grid currents obtained from the two strategies, respectively.

5.5.4 Operation under load resistance variation

A sharp load resistance decrement from 280 Ω to 140 Ω at time instant 2 s is applied to the system, as illustrated in Fig. 5.7. By following the designed control law based on the system model, the output voltage can avoid excessive distortion in MPSMC. Although the MPPIC can recover to the original voltage

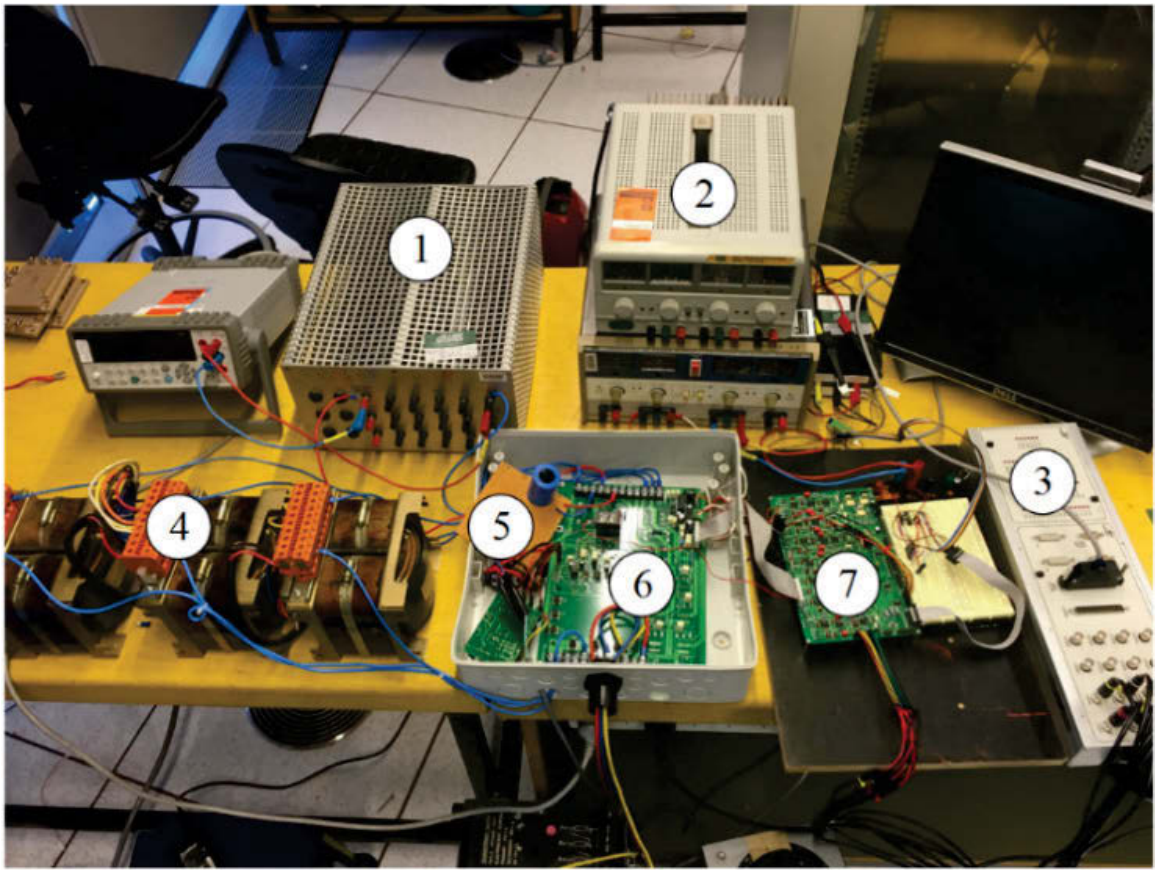

Figure 5.8 : Experimental setup of the AC/DC converter, where the labelled numbers are ① DC resistive load, ② DC power supply, ③ dSPACE, ④ inductors, ⑤ DC capacitor C, ⑥ AC/DC converter, and ⑦ control unit.

within a finite time length, the settling time, equal to 0.6 s, is much longer than the proposed method and the undershoot, equal to 2%, can hardly be avoided. The proposed MPSMC performance exhibits a fast response with no undershoot on the load voltage, as well as the active power, as illustrated in Figs. 5.7(a) and (b). Note that the transient currents on the grid side obtained from the MPSMC and MPPIC strategies present similar performance in Figs. 5.7(c) and (d), respectively.

5.6 Experimental Testing

A laboratory prototype of the AC/DC converter, as shown in Fig. 5.8, was developed for the verification of the proposed MPSMC and the MPPIC schemes. A three phase variac was used to achieve a 50 V / 50 Hz power supply voltage. A 6MBP50RA-060-55 Three-Phase IGBT Module from Fuji Electric was used as the three-phase AC/DC converter. A 680 μF DC capacitor and a 140 Ω resistance load with a current limitation of about 1.5 A are connected in parallel on the DC side. The experimental parameters are the same as the simulation parameters, presented in Table 5.1. Four LEM voltage sensors (LEM LV 25-P) and three LEM current sensors (LEM LA 25-NP) were used to measure the DC-link voltage, grid voltages and grid currents, respectively.

The experimental tests of the proposed MPSMC and the conventional MPPIC methods are carried out by applying the real-time interface system dSPACE with a DS1104 control desk. This control desk works together with MATLAB/Simulink-R2009. Both control schemes are implemented in C language, and the computations are performed on the dSPACE DS1104 controller board. The sampling frequency is 10 kHz in the experimental tests. The data recording and reference values were observed and set via the dSPCE ControlDesk environment. The obtained experimental results are shown in Figs. 5.12, 5.13 and 5.14 for both MPSMC and MPPIC schemes during various disturbance operations. The reactive power is set to 0 Var to achieve a unit power factor. Since it takes a long time for the system to reach the new operation with no steady state error by using the conventional MPPIC method, the response time for the MPPIC scheme in the following experimental results is realistically defined as the time for the system to reach a new operating condition within a 1% steady state error.

5.6.1 Selection of PI parameters for MPPIC scheme

In order to choose the best MPPIC method performances to compare with MPSMC, the standard rule of designing the PI controller proportional and integral parameters, denoted as K_p and K_i, respectively, is used in this chapter [121].

A parameter z defined as

$$z = \frac{V_{dc}^2}{2}, \tag{5.27}$$

is introduced to analysis the system plant.

Then the first-order derivation of z can be written as

$$\dot{z} = V_{dc}\dot{V}_{dc}. \tag{5.28}$$

Equation (5.9) can then be rewritten as

$$P_{ref} = C\dot{z} + \frac{2z}{R_L}. \tag{5.29}$$

The system plant can be expressed as

$$G(s) = \frac{z}{P_{ref}} = \frac{\frac{R_L}{2}}{\frac{R_L C}{2}s + 1}. \tag{5.30}$$

Based on the standard rules in Table 4.5 in [121], the rate of K_p/K_i is calculated by using

$$\frac{K_p}{K_i} = \frac{\xi^2 R_L^2 C}{(1 + \frac{R_L}{2})^2}, \tag{5.31}$$

where ξ is the damping ratio of the system, and recommended to be set as 0.707.

Based on this design principle, the PI parameters K_p and K_i are fine tuned for each specific operation condition. The selection process is analysed and the obtained DC-link voltage performances with different controller parameter values are compared.

Fig. 5.9 shows the different voltage performances with varying K_p values and a constant K_i. With the same reference, the overshoot and response time will be

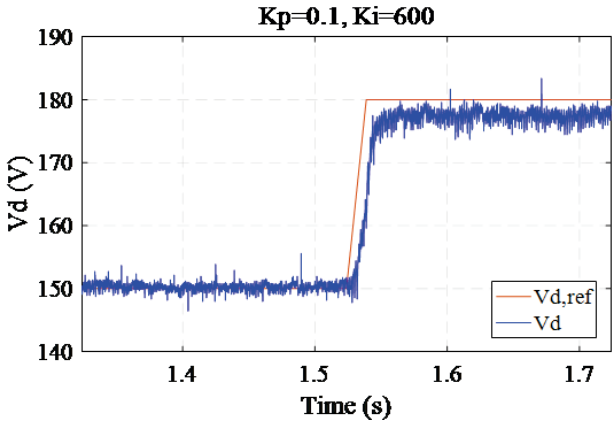

(a)

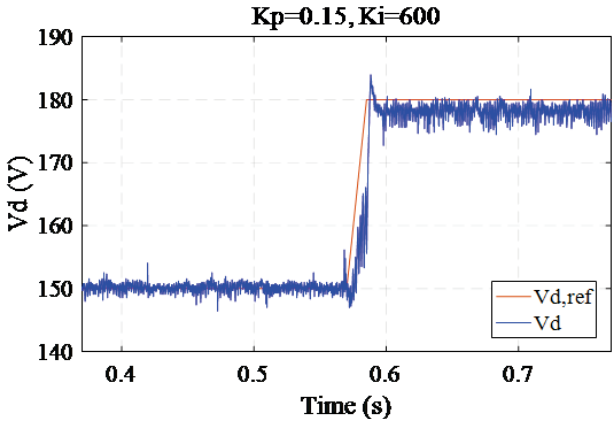

(b)

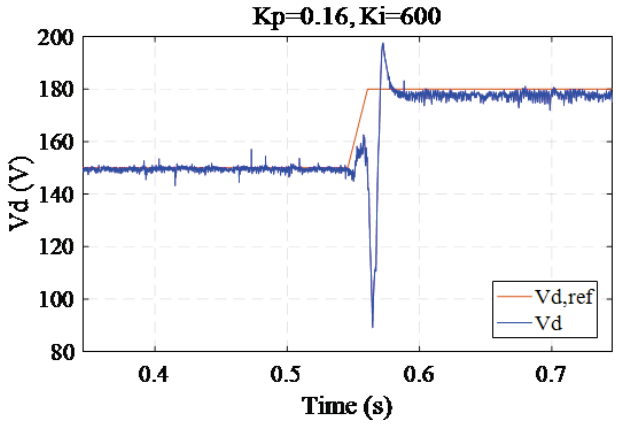

(c)

Figure 5.9 : V_{dc} performances with different K_p gains for voltage variation operations.

affected by the gains of PI controller. As shown in Fig. 5.9, the output voltage can reach the reference value much faster with a larger proportional part. On the other hand, this increased K_p leads to an overshoot on the voltage. Taking both the overshoot and response times into consideration, an appropriate K_p, which equals 0.15, was selected for this test.

Once the gain of K_p is adopted, the integral parameter K_i is chosen based on the steady state error and the oscillation. It can be observed from Fig. 5.10 that the DC voltage is able to achieve the target under different K_i gains. The steady state error keeps within 2% of the expected value. However, when the K_i is small, as shown in Fig. 5.10(b), the output keeps increasing to reach the reference without any error. This takes a long settling time for the system. While with a larger value of K_i in Fig. 5.10(c), this yields a faster response, but also a larger amplitude of oscillation. Considering these two factors, a K_i coefficient with 600 is devised for this system. Therefore, a PI controller with K_p and K_i, equal to 0.15 and 600, respectively, was designed for voltage variation operations.

It is noticeable that if the same parameters are used in load variation operations, as described in Fig. 5.11(a), the undershoot is comparatively large, which is not the best performance for MPPIC. From Fig. 5.11, it can be seen that the larger coefficient K_p the system has, the less undershoot the DC-link voltage will perform, as long as the system is stable. Therefore, $K_p = 0.3$ was tuned manually to get better performances in the load variation comparison study. Based on the above analysis, it can be seen that automatic tuning is significant and necessary for the PI controller to achieve better steady and dynamic performances.

The oscillations that are observed in Figs. 5.9-5.11 are due to the background noise, analogue-to-digital conversion error, limited vectors in the MPC method, and certain uncontrollable practical factors.

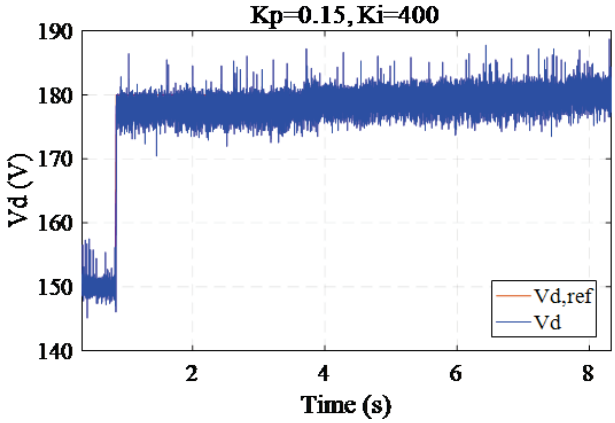

(a)

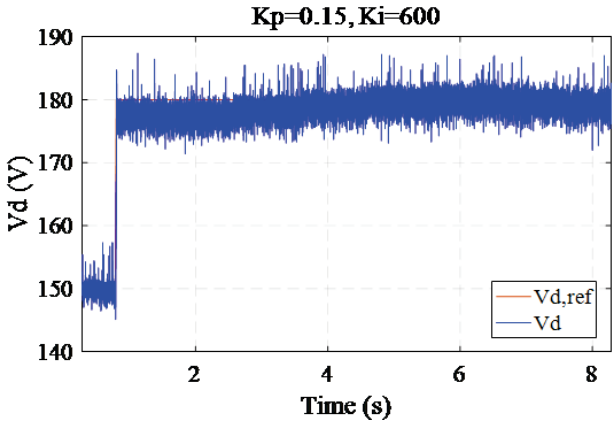

(b)

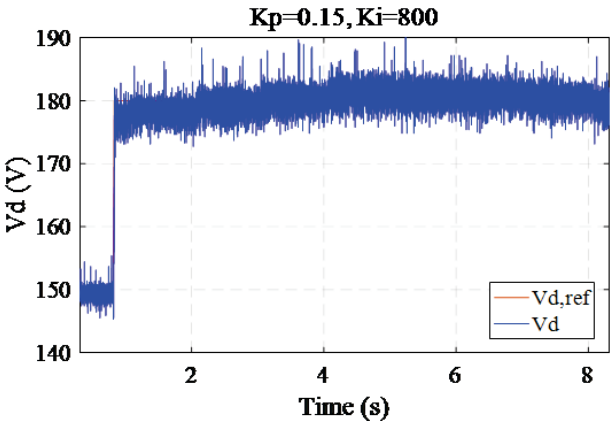

(c)

Figure 5.10 : V_{dc} performances with different K_i gains for voltage variation operations.

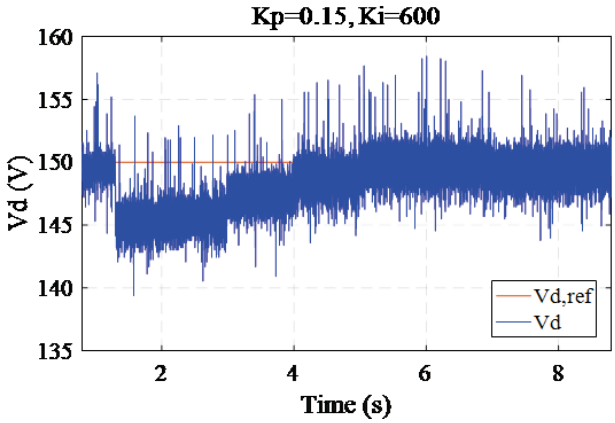

(a)

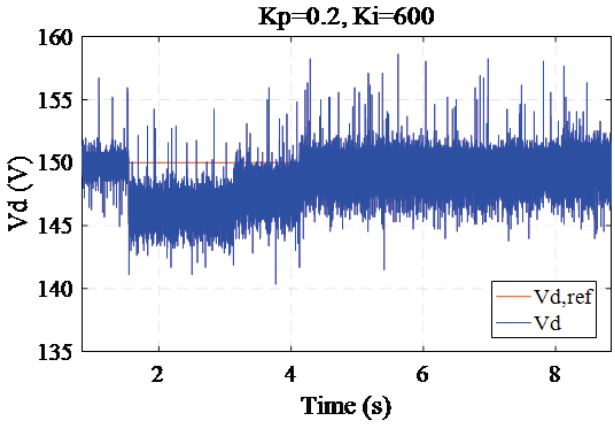

(b)

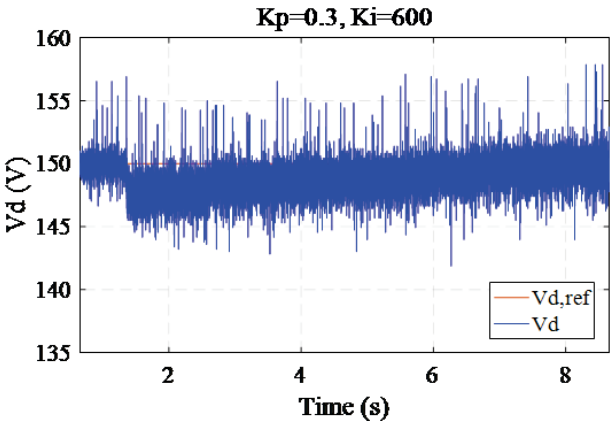

(c)

Figure 5.11 : V_{dc} performances with different K_p gains for the load variation operation.

5.6.2 Comparison of MPSMC and MPPIC schemes

The dynamic performances of the standard and proposed methods with the DC-link voltage demand variations are experimentally compared in Figs. 5.12 and 5.13. It can be seen clearly that the output DC-link voltage can be regulated to the desired value for both proposed MPSMC and traditional MPPIC methods. The DC voltage reference steps from 150 V to 180 V at 0.3374 s. It takes 0.0177 s for the system controlled by the proposed MPSMC method to reach the new steady state, which is much shorter than 0.0253 s by the conventional MPPIC scheme with 1% steady state error. The response time has been reduced by 30%. From Fig. 5.12(b), it can be observed that there is an obvious overshoot of DC-link voltage by using the traditional method. Similar performances of active power and reactive power for both schemes are illustrated in Figs. 5.12(c) and (d), respectively. For both two algorithms, an overshoot is introduced on the active power and the PQ coupling cannot be eliminated. When the active power increases, there is an obvious spike on the reactive power obtained from the MPPIC strategy. Figs. 5.12(e) and (f) depict the grid currents of phase A for two control strategies. The current dynamic response obtained from MPSMC also presents a much faster speed than that from MPPIC. The grid current response time is similar to that for the DC voltage obtained from the corresponding scheme within 1% steady state error.

Fig. 5.13 presents the dynamic and steady performances of the two methods when a reduction in the voltage demand is applied. The DC voltage obtained from MPPIC has a steady state error of approximately 1.3% for the operating point while the error for MPSMC is zero. This means that a much longer response time is required for MPPIC to track the reference value without steady state error. The reason for this steady state error is that the PI control parameters are selected to ensure the system will operate effectively when a 180 V voltage reference is employed. During the operation, this pair of parameters is fixed and constant.

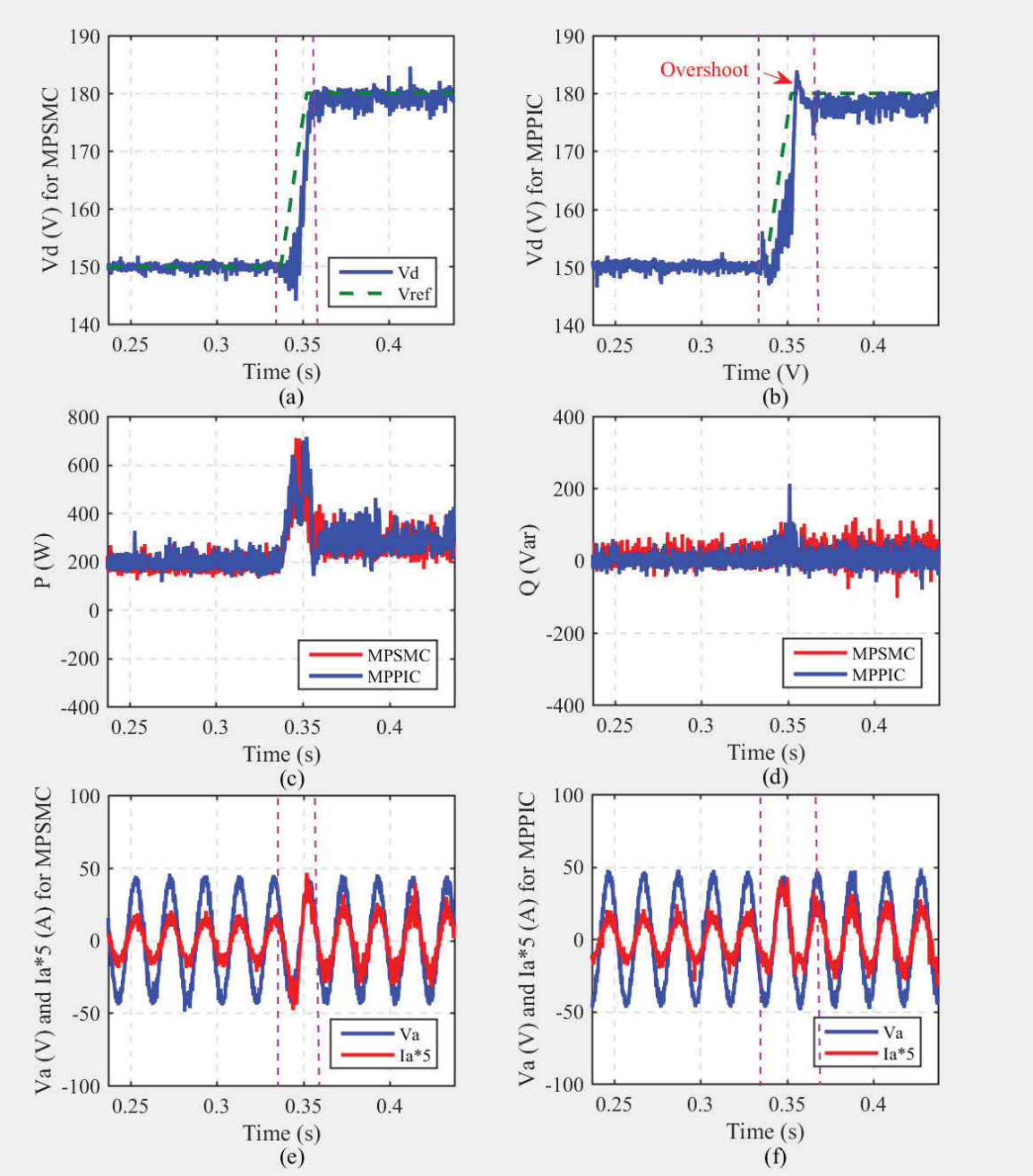

Figure 5.12 : Experimental results of sudden increase of DC voltage, where (a) DC voltage of MPSMC, (b) DC voltage of MPPIC, (c) Active power, (d) Reactive power, (e) Instantaneous voltage and current of phase A in MPSMC, and (f) Instantaneous voltage and current of phase A in MPPIC.

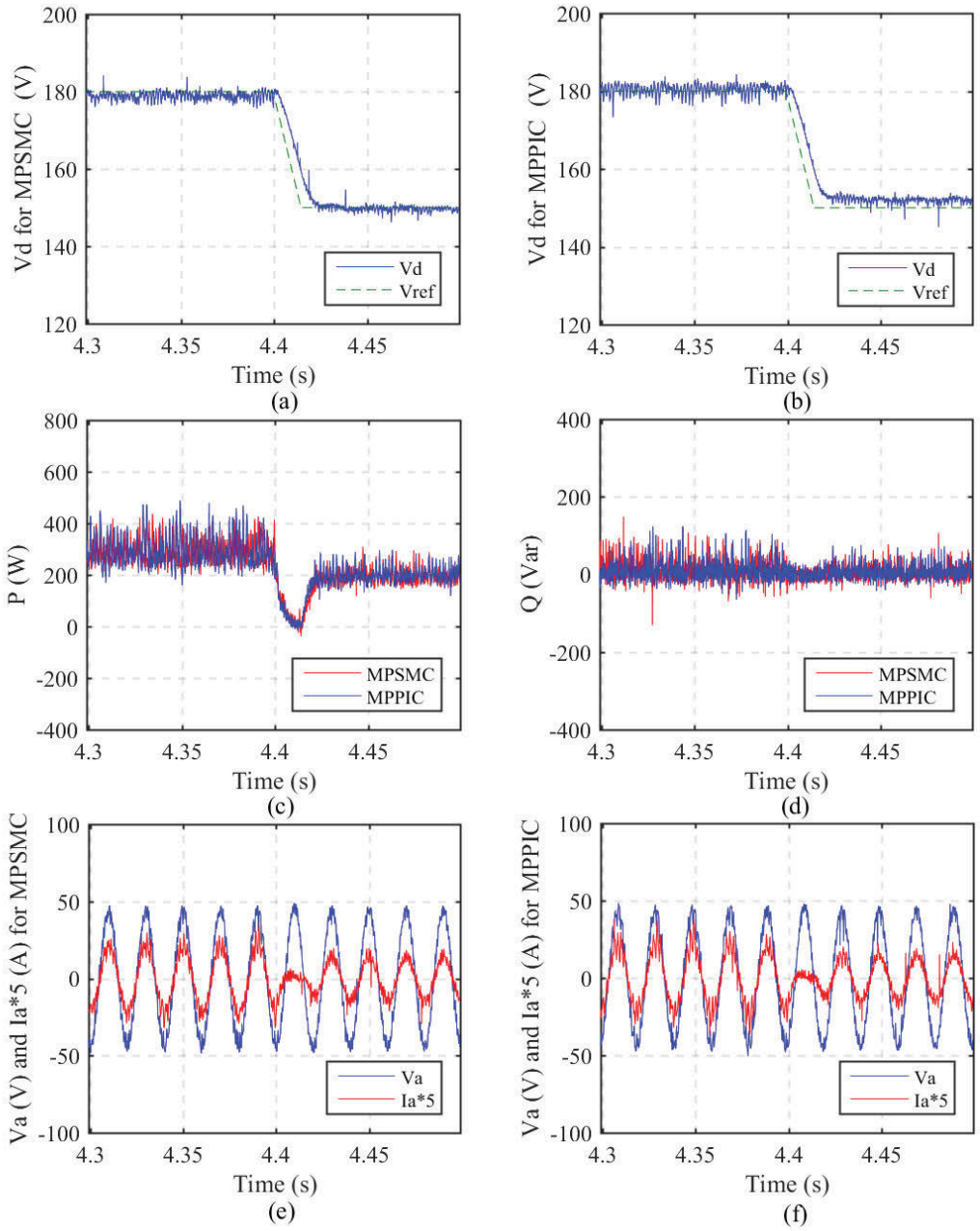

Figure 5.13 : Experimental results of unexpected decrease demand of DC voltage, where (a) DC voltage of MPSMC, (b) DC voltage of MPPIC, (c) Active power, (d) Reactive power, (e) Instantaneous voltage and current of phase A in MPSMC, and (f) Instantaneous voltage and current of phase A in MPPIC.

However, these selected parameters are not the best choice for the new working condition when the voltage reference is reduced to 150 V. It is impossible for them to be tuned automatically based on different operations, which leads to a long response time. Compared with the dynamic performances of MPPIC, similar performances of active power, reactive power and ac current are shown in Figs. 5.13(c), (d), (e) and (f), respectively. With the selected PI parameters, the system voltage inclines to decrease rather than increase, which yields no overshoot. Therefore, the current during the voltage drop operation is different from that during the voltage increase operation, which can also be proved in the simulation result.

The dynamic responses to the external load disturbance by applying MPSMC and MPPIC strategies are exhibited in Fig. 5.14, where the external load is suddenly changed from 280 Ω to 140 Ω at time instant 3.4 s. As the sliding surface is designed based on the model, the DC-link voltage can reach the new state almost immediately, as shown in Fig. 5.14(a). Fig. 5.14(b) is the experimental DC-link voltage waveform for the conventional MPPIC. It has an undershoot of the DC voltage and takes around 1.5 s to track the reference after the load variation. It can be verified that the control performance by using the proposed method is improved since the undershoot can be eliminated. Fig. 5.14(c), (d), (e) and (f) show that the dynamic performances for active power and grid current are much similar for both schemes, respectively.

5.6.3 Discussion

Table 5.2 summarizes the settling time of simulation and experimental tests by using the proposed MPSMC and MPPIC algorithms. The response time for the simulation results is from the starting point to the steady point when the output hits the reference with no steady state error. For the experimental results, due to the signal transmission and acquisition, the settling time with no steady state error

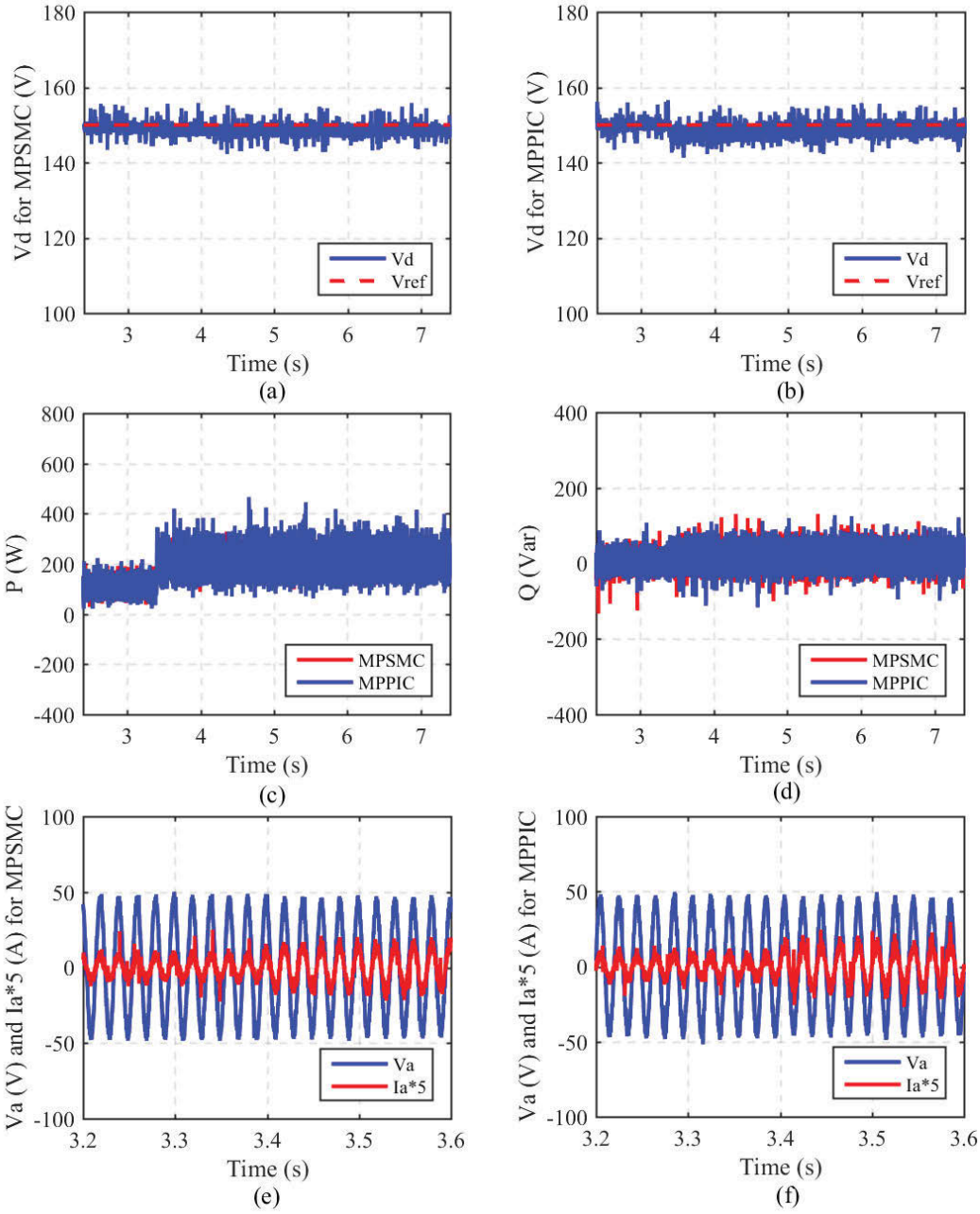

Figure 5.14 : Experimental results of unexpected change on load resistance, where (a) DC voltage of MPSMC, (b) DC voltage of MPPIC, (c) Active power, (d) Reactive power, (e) Instantaneous voltage and current of phase A in MPSMC, and (f) Instantaneous voltage and current of phase A in MPPIC.

is longer than the simulation results. In order to analyze the dynamic performance, the response time is defined from the starting point to the final point within 1% steady state error for voltage variation operations. Therefore, the results obtained from the experimental tests are much shorter than those from simulation tests during the voltage varying operation. It can be seen from Table 5.2 that the settling times obtained from MPSMC are much shorter than those from MPPIC for both simulation and experimental tests. For the load variation operation, in order to observe the steady state performance, the settling time is compared when the output hits the reference value with no error. As shown by both simulation and experimental results, the proposed MPSMC exhibits better performance than the traditional MPPIC. Due to the use of space voltage vectors, both the switching frequency for MPPIC and MPSMC methods are not constant.

There is an inrush current in the simulation results of MPSMC or MPPIC, as shown in Fig. 5.4. The reason is that the grid source with 50 V amplitude was connected all the time. When we started the system, there was an inrush current at the beginning. In the experiment, for safety reason, a variac is connected between the power grid and the system. The voltage increases slowly from 0 V to the expected value. By increasing the power supply slowly, the inrush current can be limited. However, since the actual system will be connected to the power grid directly, it will cause a large inrush current that may destroy or reduce the lifetime of the semiconductor as well as false-trigger the protection circuit in the AC power supply. Nevertheless, a by-pass diode or a soft-start procedure can be added in this situation to reduce and limit the inrush current.

5.7 Concluding Remarks

In this chapter, a novel model predictive sliding mode control technique named MPSMC was presented and implemented for an AC/DC converter. The proposed

Table 5.2 :

Settling time for simulation and experimental tests.

Operation	Control schemes	MPSMC (s)	MPPIC (s)
Voltage increase	Simulation results	0.03	0.35
	Experimental results (within 1% steady state error)	0.0177	0.0253
Voltage decrease	Simulation results	0.025	0.025
	Experimental results (within 1% steady state error)	0.02	0.03
Load variation	Simulation results	< 0.01	0.6
	Experimental results (steady state error is 0)	< 0.1	1.5

control method was compared and contrasted to a model-based control scheme called MPPIC, which is based on the system model and the designed cost function. According to the objectives and parameter references, it was possible to select an optimal switching state to achieve the target. The PI controller was applied to generate the active power reference in the control loop. During the operation, the system will encounter some transient disturbances, such as voltage and load demand variations. However, the parameter values of the PI controller are constant, which are hard to adjust along with system disturbances. MPSMC combines the main advantages of both MPPIC and SMC schemes, such as the ability to achieve multi objective control and simple implementation. The designed surface of the SMC is based on

the system model. This design can help it track the references and load resistance much more accurately and faster. The proposed MPSMC method was validated by extensive simulation and experimental testing in comparison with MPPIC. The results show that with the same demand variation, the MPSMC technique has a faster dynamic response and no steady state error of the DC-link voltage compared with the MPPIC scheme. The effect of improvements depends on the variations of different system disturbances and demands. On the other hand, the dynamic and steady state performances of active power, reactive power and grid currents obtained from the MPSMC were much better than those achieved from the MPPIC.

Chapter 6

SYSTEM CONTROL OF A SMART CAR PARK INTEGRATION WITH GRID

6.1 Introduction

Electrica vehicles (EVs) have been extensively used in a range of applications in transportation systems, such as public buses [122], personal vehicles [123], and railway trains [124]. Compared with the traditional gasoline cars, EVs have several advantages: the application of the clean energy, high efficiency, environmental protection and control over the charged or discharged energy [125]-[128].

With the widespread use of EVs, a larger number of EV batteries will be plugged into the grid or distributed systems. To take full advantage of the plugged EV batteries, bidirectional converters have attracted researchers attention [129]-[130]. Energy management system and optimization charging methods were proposed and reviewed in [126] and [131]. With effective control strategies, the EV batteries can exchange the energy with the main power grid. Generally, the grid provides the active power to charge the batteries, known as the grid-to-vehicle (G2V) technology. On the other hand, the EV batteries can operate as active power generators with the bidirectional control schemes, called the vehicle-to-grid (V2G) operation [80]. Apart from supporting the grid with the active power, nowadays, EVs have abilities to improve the power quality by compensating the reactive power, and this is called vehicle-for-grid (V4G) [5]. The works in [24] and [132] investigated the reactive power operation for EVs using off-board chargers while charging the batteries. Tanaka proposed a reactive power control strategy to reduce the capacity of smart

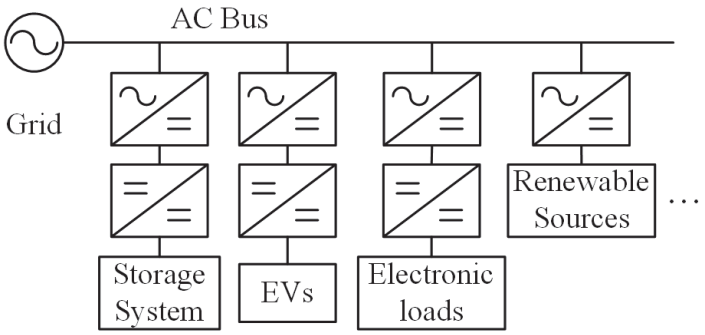

(a) AC bus structure.

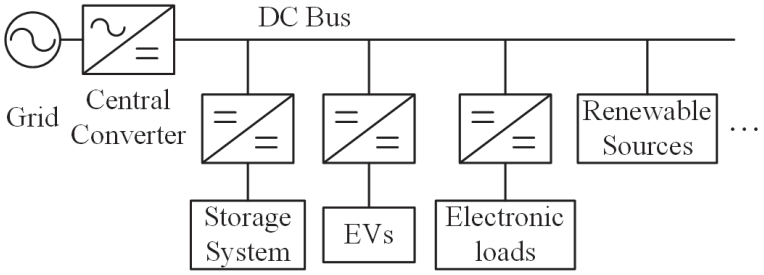

(b) DC bus structure.

Figure 6.1 : System block diagram for EV charging stations with (a) AC bus structure, and (b) DC bus structure.

chargers for EVs [133]. In most of these papers, EV chargers have been used as the SVCs. In this chapter, the proposed system operates in G2V, V2G and V4G modes to support the grid by exchanging both active and reactive powers simultaneously [102, 134].

For micro-grids, such as smart homes, smart buildings and smart car parks, DC bus and AC bus topologies are the two basic connections between the grid and numerous charging stations [135]. The EV charging station with the AC parallel solution is presented in Fig. 6.1(a). The topology has several interleaved AC/DC converters to connect the grid with loads. Each integrated charger is independent of the others, which improves the system stability. However, one of the disadvantages for this complex structure is that more components are required compared with

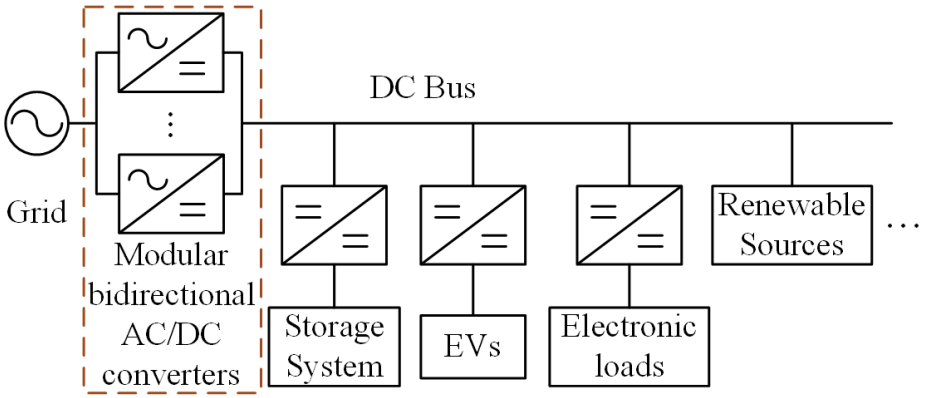

Figure 6.2 : DC bus topology with modular AC/DC converters.

the DC bus system. This serious problem leads to higher cost, larger size and more complex control strategies for this AC parallel topology. In a DC distribution system, shown in Fig. 6.1(b), a main central AC/DC converter with high power ratings is needed to interface the grid [136]. The main AC/DC converter is in series with the EV chargers, storage systems and other electronic loads via AC/DC converters. The reliability of the distributed system relies strongly on the central converter. Once unexpected faults occur in the AC/DC converter, the whole system will be affected and influenced. To solve this problem, an improved topology with modular bidirectional AC/DC converters is proposed in work [137] to replace the main central AC/DC converter, as shown in Fig. 6.2. Due to the DC structure, it is a viable solution for the nature of the loads [136]. However, since there is no zero-crossing point in the DC bus system, it has a great potential risk of the DC arcing fault [138]. Table 6.1 compares the pros and cons of the AC and DC buses structures from the users view.

To analyse the dissemination of EV batteries bidirectional power flow, a comparison of AC and DC buses systems for off-board EV charging stations is presented in this chapter.

Table 6.1 :

Features of AC and DC buses systems

Compare aspects	AC system	DC system
AC/DC converter	in parallel, independent and convenient	in series, dependent and high power ratings
System reliability	do not rely on AC/DC converters	rely on the main AC/DC converter
Cost	high	low
Size	larger	small
Others features	more complex control strategies are needed	no zero-crossing leads to DC arcing fault

6.2 Active and Reactive Power Controllers for AC and DC Buses

A smart car park consists of numerous charging stations, an aggregator and some storage devices, as proposed in the work [76]. Fig. 6.3 shows the smart car park system with a DC bus, which is composed of a central three-phase 2-level AC/DC converter and numerous bidirectional DC/DC converters interfaced with the EV batteries. Fig. 6.4 shows the smart car park system with an AC bus, where the EV batteries are connected with the main grid through a three-phase 2-level AC/DC converter and a bidirectional DC/DC converter. Each charging station is independent of the rest of the chargers.

Ignoring the power loss in the transmission, the active and reactive powers re-

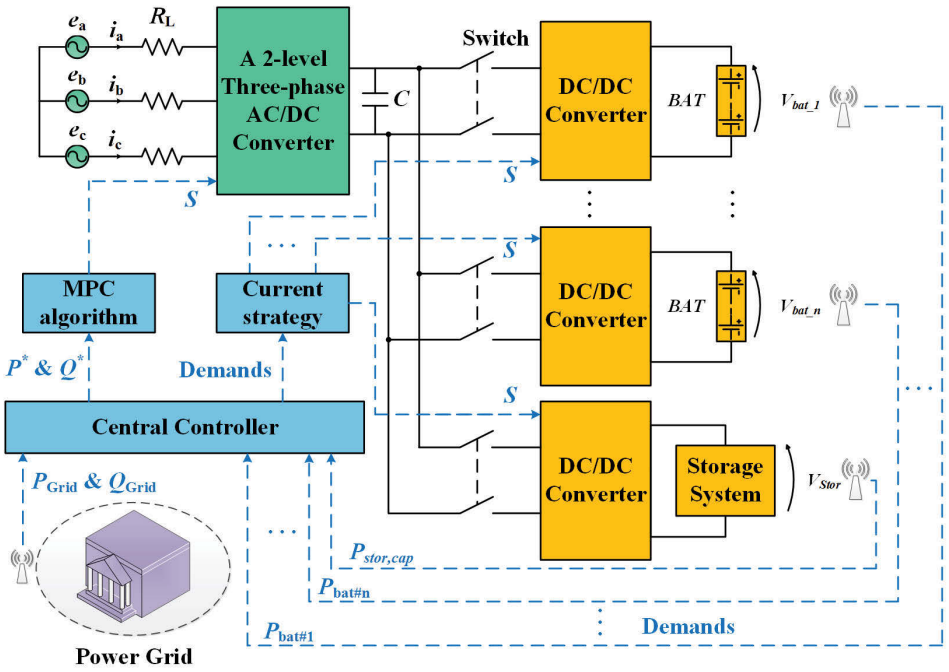

Figure 6.3 : Proposed DC bus for charging stations.

lationships among the main grid, EV batteries and the storage devices can be expressed as

$$P_{Grid} = \sum_{n=1}^{N} P_{dc\#n} + P_{Stor}, \tag{6.1}$$

$$Q_{Grid} = \sum_{n=1}^{N} Q_{dc\#n} + Q_{Stor}, \tag{6.2}$$

where P_{Grid}, Q_{Grid}, P_{Stor}, Q_{Stor}, $P_{dc\#n}$ and $Q_{dc\#n}$ are the active and reactive powers provided by the grid, absorbed by the storage system, transferred by the nth DC/DC converter, respectively, and N is the current number of EVs parking in the smart car park. The positive direction of the active and reactive powers flows from the grid to the batteries.

Each EV battery will be plugged into the charging station after arriving at the car park, and the battery demands are sent to the central controller via the WiFi connection. Therefore, the nth battery expected energy ($P^*_{bat\#n}$) can be represented

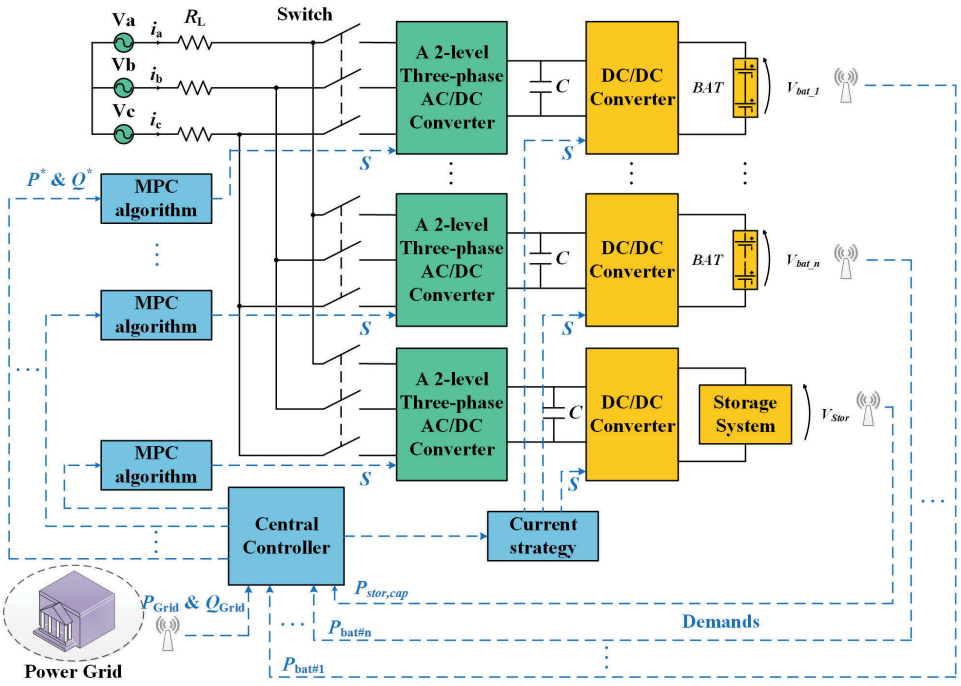

Figure 6.4 : Proposed AC bus for charging stations.

as

$$P^*_{bat\#n} = P^*_{dc\#n} \quad (n = 1, \cdots, N). \tag{6.3}$$

where $P^*_{dc\#n}$ is the reference value of the nth DC/DC converter active power. $P^*_{bat\#n}$ is determined by the nth EV's parking time, expected SOC and rated capacity.

The grid active and reactive power are sent to the MPC strategy as the reference values to control the AC/DC converters, and can be expressed as

$$P^*_{Grid} = \sum_{m=1}^{M} P_{ac\#m} \tag{6.4}$$

$$Q^*_{Grid} = \sum_{m=1}^{M} Q_{ac\#m} \tag{6.5}$$

where $P_{ac\#m}$ and $Q_{ac\#m}$ are the transferred active and reactive power of the mth AC/DC converter, and M is the number of the current connected AC/DC converters.

From Fig. 6.3, it can be seen that one main three-phase 2-level AC/DC converter is needed in the DC Bus, which means M is equal to 1. Thus, (6.4) and (6.5) can

be rewritten as

$$P^*_{Grid} = P_{ac} = \sum_{n=1}^{N} P^*_{bat\#n} + P_{Stor}, \tag{6.6}$$

$$Q^*_{Grid} = Q_{ac}, \tag{6.7}$$

In the AC bus system, as shown in Fig. 6.4, each DC/DC bidirectional charger interfaces with the main power grid via an AC/DC boost converter. Hence, (6.4) and (6.5) can rewritten as

$$P^*_{Grid} = \sum_{n=1}^{N+1} P_{ac\#n} = \sum_{n=1}^{N} P^*_{bat\#n} + P_{Stor}, \tag{6.8}$$

$$Q^*_{Grid} = \sum_{n=1}^{N+1} Q_{ac\#n} = \sum_{n=1}^{N} Q^*_{dc\#n} + Q_{Stor}, \tag{6.9}$$

Once the active power commands obtained from the main grid and the EVs are determined, the storage device is used to compensate the difference between them. Since the capacitor of the storage system ($P_{Stor,cap}$) is limited, one system constraint is defined as

$$P_{Stor} \leq P_{Stor,cap}. \tag{6.10}$$

6.3 Numerical Simulation

Comparative simulation results obtained from the smart car park system with DC and AC buses are presented in this section. In order to simplify the observation of the power flow during transmission and the EV battery information, five charging stations are used in this simulation. The smart car park system electric parameters are shown in Table 6.2. The five EVs arrival and departure time information are presented in Fig. 6.5. The active power reference vector of EVs P^*_{bat} is defined as [1000 -500 -1000 2000 500] (W). The two topologies are compared in the G2V, V2G, inductive or capacitive V4G, and the combination of G2V or V2G with (inductive/capacitive) V4G operations. Note that the vehicle-to-vehicle (V2V) operation mode exists along with the aforementioned eight operations.

Table 6.2 :

System parameters for bidirectional charger

Symbol	Quantity	Value
R	Grid line resistance	0.25 Ω
L	Filter inductor	10 mH
C	Filter capacitor	470 μF
L_{dc}	DC inductor	100 μF
V_{LL}	Grid line-line voltage (RMS)	100 V
f	Grid frequency	50 Hz
T_s	Sample time	50 μs
V_{bat}	Battery rated voltage	300 V
SOC_{ini}	Battery initial SOC	50%

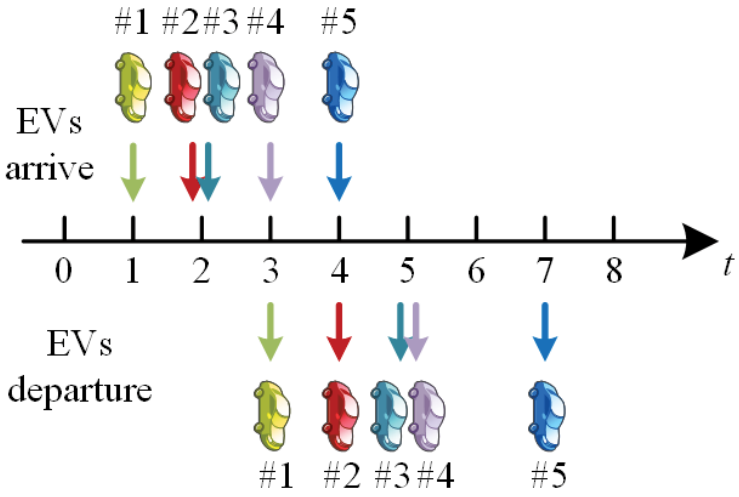

Figure 6.5 : Arrival and departure time of the parking EVs.

Fig. 6.6 compares the dynamic response of active and reactive powers provided by the main power grid with DC bus and AC bus connection topologies, respectively. It can be observed that with the proposed two circuit structures, the system can be controlled to meet the grid active and reactive power requirements effectively. However, both the active and reactive powers obtained from the AC bus topology have larger ripples than the power from the DC bus, as shown in Figs. 6.6(a) and 6.6(b), respectively.

Fig. 6.7 shows that all the EVs can be charged or discharged with expected powers based on their demands, arrival and departure times. For example, the 1st EV (#1) is plugged into the station at $t = 1s$ and parked for $2s$ with the power reference equal to 1000 W. It can be seen that the charger can track the EV's demand and has a fast dynamic performance. The battery active power reference P_{bat} is set to be zero when no EVs are plugged into the chargers.

A storage device, such as a super-capacitor, is used to compensate the active power difference between the grid and the EVs. It works effectively in both DC and AC buses, as shown in Fig. 6.8. According to the demands from the grid and the EV customers, the storage system can operate as the energy consumption load or an active power generator. On the other hand, when the active power provided from the grid is equal to the active power absorbed by the EV batteries, no action is performed in the storage system. As an example, since no EVs are plugged in during the first time interval ($0 \sim 1s$), the storage device is considered as the only load to absorb the energy from the grid to meet the needs.

In Figs. 6.9 and 6.10, the batteries' SOCs and currents are described according to the expected batteries charging power P_{bat}. From the results, the fast dynamic response and the great steady-state performance are further verified. The battery SOC keeps constant when EV battery is unplugged.

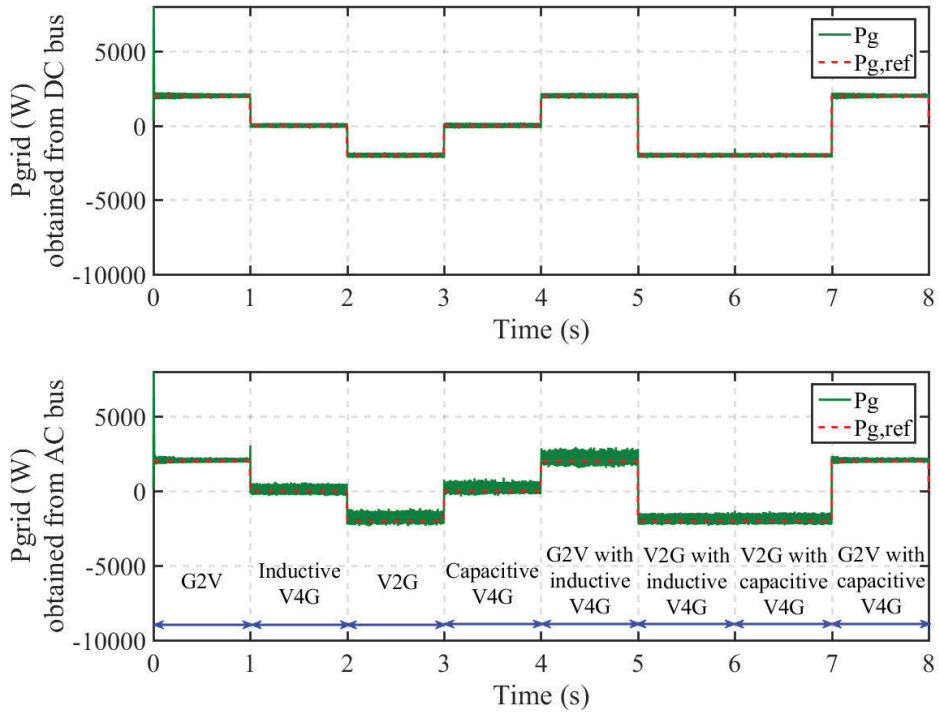

(a) Active power.

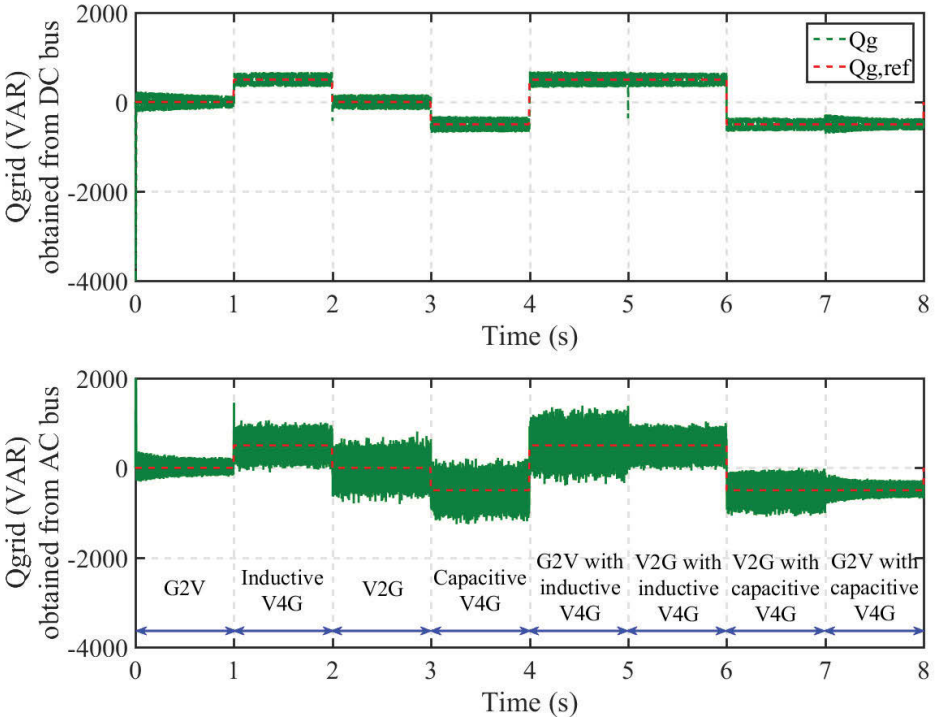

(b) Reactive power.

Figure 6.6 : Active and reactive powers of the power grid.

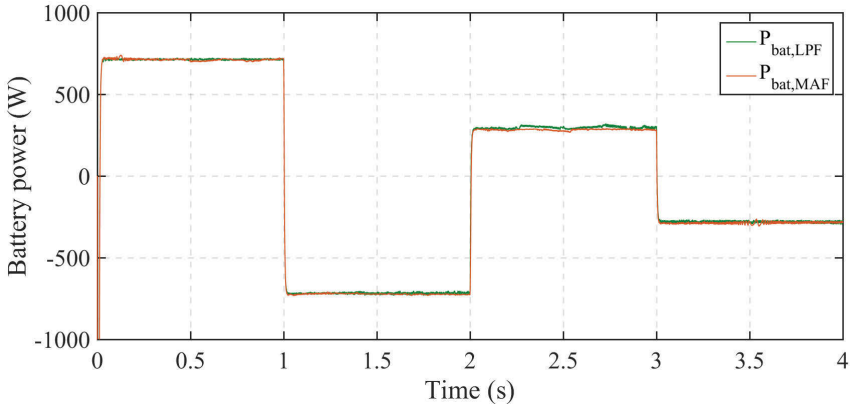

Figure 6.7 : Active power of the EV batteries.

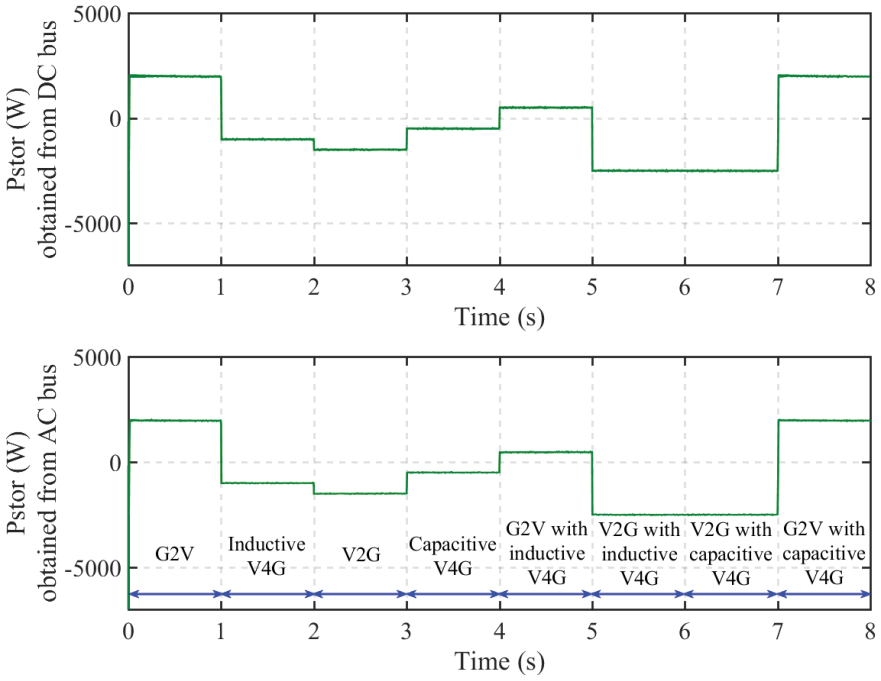

Figure 6.8 : Active power of the storage device.

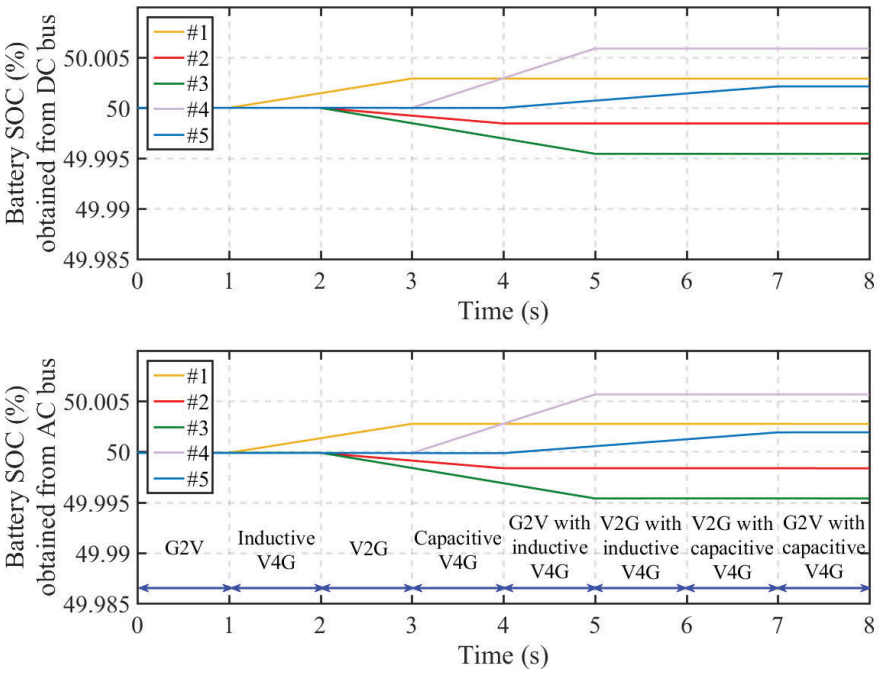

Figure 6.9 : SOC of EV batteries while connected to charging stations.

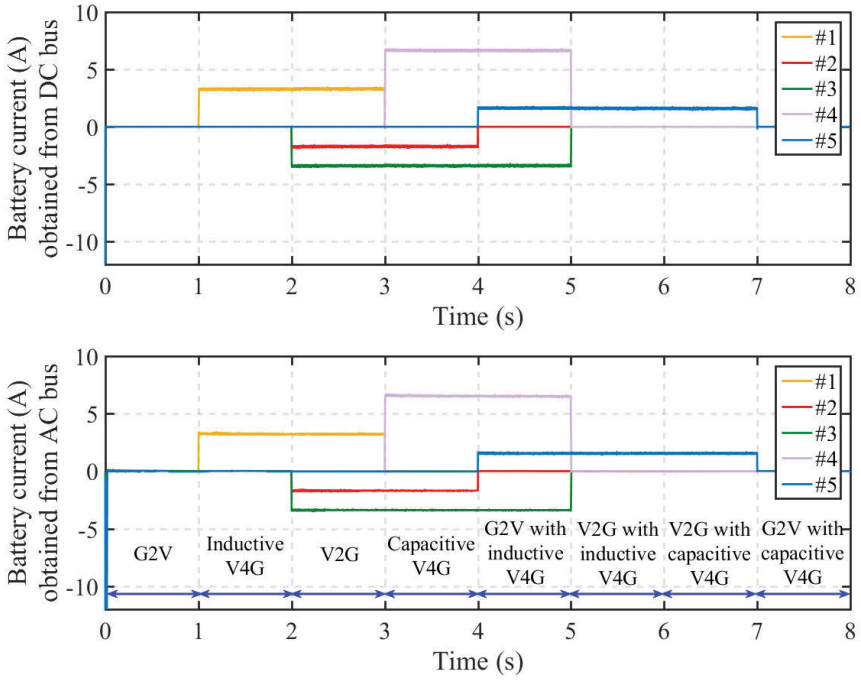

Figure 6.10 : Currents of EV batteries while connected to charging stations.

Table 6.3 :

System performance of DC and AC buses

Parameters		DC Bus	AC Bus
Ripple	P_{Grid}	92 W	144 W
	Q_{Grid}	87 VAR	203 VAR
THD	G2V	4.3%	5.9%
	V2G	18.0%	33.0%
	Inductive V4G	5.0%	12.0%
	Capacitive V4G	20.5%	41.0%
	G2V with inductive V4G	4.9%	11.0%
	V2G with inductive V4G	4.4%	8.4%
	V2G with capacitive V4G	4.1%	8.5%
	G2V with capacitive V4G	4.0%	5.5%
	Execute time	115 sec	775 sec

Table 6.3 presents the comparison results of DC and AC bus systems in the dynamic performance, including the power ripple, THD and execute time. From the comparisons, it can be seen that lower active and reactive power ripples can be achieved with the DC bus topology. The THD obtained from the DC bus system is much smaller than that from the AC bus during numerical simulation operations. The execute time is reduced from $775s$ to $115s$ by using a DC bus instead of an AC parallel structure. It should be noted that the active and reactive power ripples were calculated using standard deviations.

6.4 Concluding Remarks

DC bus and AC bus topologies for bidirectional power flow chargers in the smart car park have been presented in this chapter. The two system structures have been compared from the users view and the grid side. With a main central AC/DC converter, the system reliability of the DC bus topology is limited and affected. The AC/DC converter power level is higher in the DC bus system than the AC system. On the other hand, the system cost and size can be reduced due to less components compared with the AC parallel structure. The MPC strategy is utilized to track the commands sent by the grid and the EV customers. Both circuits operate under G2V, V2G, V4G and the combinations of G2V and V4G or V2G and V4G modes, to support the grid and the batteries. The storage device and EV batteries can be regarded as not only the general loads, but also the active power generator and the reactive power compensator. An efficiency comparison is presented in terms of power ripple, THD and execute time. This comparison was performed under the proposed eight operations. The obtained results show that both the DC and AC bus structures can track the grid references and satisfy the EV batteries demands effectively. The dynamic response is fast and the steady state performance is good in both two systems. However, the power ripples, THD, execute time are much

lower using a DC topology than applying an AC topology.

Chapter 7

CONCLUSIONS AND FUTURE WORK

7.1 Conclusions

This dissertation presents a smart car park system model and finite control set model predictive method for bidirectional chargers. A car park with numerous EVs can be regarded as an energy storage device. It can support the main power grid by exchanging active and reactive powers. The model predictive control theory has been used widely in science and it has received high attention for power electronics over the last several decades. Compared with PI control and direct power control, predictive control scheme show better system performance. This work develops a smart car park system where the EV batteries and charging stations exchange the active and reactive power using model predictive control or a modified MPC technique.

In Chapter 3, the infrastructure of a smart car park model with numerous EVs is presented. The proposed model has a control center to interface with the power grid and charging stations. The charging/discharging power rates, real-time electricity price and grid demand are considered in the model. Profits of the car park obtained from exchanging the active and reactive powers are detailed and described. An optimal charging/discharging method is proposed to maximize the profit for the car park owner and save the cost for EV drivers. From the simulation results, it can be seen that with the proposed optimal charging/discharging scheme, the car park profit is improved and the EV customers costs are reduced.

In Chapter 4, a modified model predictive control method for bidirectional power

flow control between the EV chargers and the main grid is proposed. In contrast to the conventional finite control set model predictive control which selects an optimal switching state from eight possible voltage vectors, the proposed MMPC is based on the application of an optimal voltage vector chosen from an extended set of 20 modulated voltage vectors with a fixed duty ratio. To reduce the computational burden introduced by the increased number of voltage sets, a pre-selection algorithm is developed for the MMPC method. Six voltage vectors are pre-selected from the 20 sectors. Due to the increased choice of voltage space vectors, the grid currents and active and reactive power performance can be improved by using the proposed MMPC scheme. Both the conventional and proposed methods are compared through numerical experimental test results of a two-level three-phase off-board EV charger. The active and reactive power ripples are reduced by using the MMPC method. Better steady-state stability and fast dynamic performance are achieved in the proposed scheme.

In Chapter 5, a model predictive sliding mode control scheme for a three-phase AC/DC converter is presented to achieve better stability and dynamic performances. In the conventional MPC method, a proportional integral controller is used to generate the active power reference. This traditional model predictive PI control scheme, however, produces a large overshoot/undershoot, a long settling time and a large steady state error under disturbances. To overcome these deficiencies, a sliding mode controller is employed to replace the PI controller. Since the control law and the controller are based on the system model, the proposed MPSMC scheme can reduce the effects of unexpected disturbances, such as the output voltage demand and the resistance load variations. Both methods were simulated in MATLAB/Simulink during various disturbances. Compared with the performances of MPPIC, the results obtained from MPSMC show that the settling time of the DC voltage can be minimized by about 91% and the overshoot can be eliminated from 9.13% during the

steady state progress. The active and reactive power from MPSMC can also be controlled to the desired values, respectively, with a much smaller overshoot/undershoot and a faster response speed. Similar dynamic improvements can be achieved with MPSMC when the DC voltage demand varies.

In Chapter 6, a comprehensive comparison of a smart car park with DC bus topology and AC bus topology for two-stage bidirectional electric vehicle battery chargers is presented. The model predictive control algorithm is applied in these two method. In terms of power ripple, THD, execute time, quantity of switches, AC/DC converter power level, switch cost and size, comparative simulations of the two topologies are performed under the proposed eight operations in Matlab/Simulink. The obtained results show that both the two system structures can operate effectively and the commands from the grid and EVs customers can be satisfied. On the other hand, the power ripple, THD, execute time, quantity of switches obtained from the DC bus topology are much lower compared with the AC bus system. Therefore, the switch cost and system size can be reduced in a DC bus. However, the power level of the AC/DC converter in a DC bus is much higher than the AC bus. Fast dynamic performance and better steady-state response are achieved in both topologies.

7.2 Future Work

This thesis takes the model predictive control for bidirectional EV chargers from numerical simulation to experimental testing results. However, there still is the potential for future research:

- In this thesis, the system can work effectively with an MPC method. However, two MPC controllers are used to control the two-level EV charger: the AC/DC converter and DC/DC converter. In my future work, one whole MPC controller will be studied to control the bidirectional two-level charger.

- Experimental validation for DC and AC bus systems in Chapter 6 will be developed to compare the characteristics of each topology.

References

[1] X. Wang, C. Jiang, and B. Lei, "Power-loss analysis and efficiency maximization of a silicon-carbide MOSFET-based three-phase 10-kW bidirectional EV charger using variable-DC-Bus control," *IEEE J. Emerg. Sel. Topics Power Electron.*, vol. 4, no. 5, pp. 880-892, Sep. 2016.

[2] B. Lee, J. Kim, and S. Kim, "An isolated/bidirectional PWM resonant converter for V2G(H) EV on-board charger," *IEEE Trans. Veh. Technol.*, vol. 66, no. 9, pp. 7741-7750, Sep. 2017.

[3] A. Schuller, B. Dieta, and C. M. Flath, "Charging strategies for battery electric vehicles: Economic benchmark and V2G potential," *IEEE Trans. Power Syst.*, vol. 29, no. 5, pp. 2014-2022, Sep. 2014.

[4] V. Monteiro, B. Exposto, and J. C. Ferreira, "Improved vehicle-to-home (iV2H) operation mode: Experimental analysis of the electric vehicle as off-line UPS," *IEEE Trans. Smart Grid*, vol. 8, no. 6, pp. 2702-2711, Nov. 2017.

[5] A. Rabiee, H. F. Farahani, and M. Khalili, "Integration of plug-in electric vehicles into microgrids as energy and reactive power providers in market environment," *IEEE Trans. Ind. Informat.*, vol. 12, no. 4, pp. 1312-1320, Aug. 2016.

[6] V. Menteiro, J. G. Pinto, and J. L. Afonso, "Operation modes for the electric vehicle in smart grids and smart homes: Present and proposed modes," *IEEE Trans. Veh. Technol.*, vol. 65, no. 3, pp. 1007-1020, Mar. 2016.

[7] https://www.energy.gov/articles/history-electric-car

[8] K. C. Nyns, E. Haesen, and J. Driesen, "The impact of charging plug-in hybrid electric vehicles on a residential distribution grid," *IEEE Tran. Power Syst.*, vol. 25, no. 1, pp. 371-380, Feb. 2010.

[9] https://www.energysage.com/electric-vehicles/101/pros-and-cons-electric-cars/

[10] M. C. Kisacikoglu, A. Bedir, and B. Ozpineci, "PHEV-EV charger technology assessment with an emphasis on V2G operation," *Oak Ridge Nat. Lab.*, Oak Ridge, TN, USA, Tech. Rep. ORNL/TM-2010/221 (2012).

[11] R. Yu, J. Ding,and W. Zhong, "PHEV charging and discharging cooperation in V2G networks: A coalition game approach," *IEEE Internet Things J.*, vol. 1, no. 6, pp. 578-589, Dec. 2014.

[12] K. Clement-Byns, E. Haesen, and J. Driesen, "The impact of charging plug-in hybrid electric vehicles on a residential distribution grid," *IEEE Trans. Power Syst.*, vol. 25, no. 1, pp. 371-380, Feb. 2010.

[13] Y. Ma and J. Wang, "Integrated power management and aftertreatment system control for hybrid electric vehicles with road grade preview," *IEEE Trans. Veh. Technol.*, vol. 66, no. 12, pp. 10935-10945, Dec. 2017.

[14] http://www.gumtree.com.au/scam-security-centre/buying-on-gumtree/the-ultimate-electric-cars-buying-guide/

[15] https://evobsession.com/electric-car-charging-101-types-of-charging-apps-more/

[16] https://www.ergon.com.au/network/smarter-energy/electric-vehicles/electric-vehicle-range

[17] M. Yilmaz and P. T. Krein, "Review of battery charger topologies, charging power levels, and infrastructure for plug-in electric and hybrid vehicles," *IEEE Trans. Power Electron.*, vol. 28, no. 5, pp. 2151-2169, Dec. 2013.

[18] D. P. Tuttle and R. Baldick, "The evolution of plug-in electric vehicle grid interactions," *IEEE Trans. Smart Grid*, vol. 3, no. 1, pp. 500-505, Mar. 2012.

[19] J. Lee, and B. Han, "A bidirectional wireless power transfer EV charger using self-resonant PWM," *IEEE Trans. Power Electron.*, vol. 30, no. 4, pp. 1784-1787, Apr. 2015.

[20] W. Li, H. Zhao, and J. Deng, "Comparison study on SS and double-sided LCC compensation topologies for EV/PHEV wireless chargers," *IEEE Trans. Veh. Technol.*, vol. 65, no. 6, pp. 4429-4439, Jun. 2016.

[21] M. C. Kisacikoglu, "EV/PHEV bidirectional charger assessment for V2G reactive power operation," *IEEE Trans. Power Electron.*, vol. 28, no. 12, pp. 5717-5727, Dec. 2013.

[22] S. Dusmez and A. Khaligh, "A compact and integrated multifunctional power electronic interface for plug-in electric vehicles," *IEEE Trans. Power Electron.*, vol. 28, no. 12, pp. 5690-5701, May 2013.

[23] M. C. Kisacikoglu, "Single-phase on-board bidirectional PEV charger for V2G reactive power operation," *IEEE Trans. Smart Grid*, vol. 6, no. 2, pp. 767-775, Mar. 2015.

[24] M. Kesler, M. C, Kisacikoglu, and L. M. Tolbert,"Vehicle-to-grid reactive power operation using plug-in electric vehicle bidirectional off-board charger," *IEEE Trans. Ind. Electron.*, vol. 61, no. 12, pp. 6778-6784, Dec. 2014.

[25] M. P. Kazmierkowski, R. Krishnan, and F. Blaabjerg,"Control in Power Electronics," *New York: Academic*, 2002.

[26] N. Mohan, T. M. Undeland, and W. P. Robbins,"Power Electronics," *Hoboken, NJ: Wiley*, 1995.

[27] A. Linder,"Modellbasierte Pradiktivregelung in Der Antriebstechnik," *Ph.D. dissertation*, Wuppertal Univ., Wuppertal, Germany, 2005.

[28] P. Cortes, M. P. Kazmierkowski, and R. M. Kennel,"Predictive control in power electronics and drives," *IEEE Trans. Ind. Electron.*, vol. 55, no. 12, pp. 4312-4324, Dec. 2008.

[29] D. Zhi, L. Xu, and B. W. Williams, "A new direct control strategy for grid connected voltage source converters," *Int. Conf. Electrical Machines and Systems, 2008 (ICEMS 2008)*, pp. 1157-1162.

[30] A. Bouafia, F. Krim and J. P. Gaubert,"Fuzzy-logic-based switching state selection for direct power control of three-phase PWM rectifier," *IEEE Trans. Ind. Electron.*, vol. 56, no. 6, pp. 1984-1992, June 2009.

[31] N. R. N. Idris and A. H. M. Yatim, "An improved stator flux estimation in steady-state operation for direct torque control of induction machines," *IEEE Trans. Ind. Appl.*, vol. 38, no. 1, pp. 110-116, Jan. 2002.

[32] G. Escobar, A. M. Stankovic, and J. M. Carrasco,"Analysis and design of direct power control (DPC) for a three phase synchronous rectifier via output regulation subspaces," *IEEE Trans. Power Electron.*, vol. 18, no. 3, pp. 823-830, May 2003.

[33] M. Monfared, H. Rastegar, H. M. Kojabadi,"High performance DPC for PWM converters," *IEEE Int. Conf. Electrical and Electronics Engineering*, 2009.

[34] S. Jin, L. Shi, and W. Cao,"Dual two-level converters based on direct power control for an open-winding brushless doubly-fed reluctance generator," *IEEE Trans. Ind. Appl.*, vol. 53, no. 4, pp. 3898-3906, June 2017.

[35] Y. Zhang, J. Gao, and C. Qu,"Relationship between two direct power control methods for PWM rectifiers under unbalanced network," *IEEE Trans. Power Electron.*, vol. 32, no. 5, pp. 4084-4094, May 2017.

[36] V. Repecho, D. Biel, and A. Arias,"Fixed switching period discrete-time sliding mode current control of a PMSM," *IEEE Trans. Power Electron.*, vol. 65, no. 3, pp. 2039-2048, Mar. 2018.

[37] K. D. Young, V. I. Utkin, and U. Ozguner,"A control engineers guide to sliding mode control," *IEEE Trans. Control Syst. Technol*, vol. 7, no. 3, pp. 328-342, May 1999.

[38] S. C. Tan, Y. M. Lai, and C. K. Tse,"General design issues of sliding-mode controllers in DCDC converters," *IEEE Trans. Ind. Electron.*, vol. 55, no. 3, pp. 1160-1174, Mar. 2008.

[39] V. I. Utkin,"Sliding mode control design principles and applications to electric drives," *IEEE Trans. Ind. Electron.*, vol. 40, no. 1, pp. 23-36, Feb. 1993.

[40] X. Yu, nd O. Kaynak,"Sliding-mode control with soft computing: A survey," *IEEE Trans. Ind. Electron.*, vol. 56, no. 9, pp. 3275-3285, Sep. 2009.

[41] J. Hu, J. Zhu, and D. G. Dorrell,"Model predictive control of inverters for both islanded and grid-connected operations in renewable power generations," *IET Renewable Power Generation*, vol. 8, no. 3, pp. 240-248, 2013.

[42] L. Tarisciotti, P. Zanchetta, and A. Watson,"Modulated model predictive control for a seven-level cascaded H-bridge back-to-back converter," *IEEE Trans. Ind. Electron.*, vol. 61, no. 10, pp. 5375-5383, Oct. 2014.

[43] S. Kouro, P. Cortes, and R. Vargas, "Model predictive control: A simple and powerful method to control power converters," *IEEE Trans. Ind. Electron.*, vol. 56, no. 6, pp. 1826-1838, June 2009.

[44] J. A. Rohten, J. R. Espinoza, and J. A. Muñoz, "Model predictive control for power converters in a distorted three-Phase power supply," *IEEE Trans. Ind. Electron.*, vol. 63, no. 9, pp. 5838-5848, Sept. 2016.

[45] J. Rodriguez, M. P. Kazmierkowski, and J. P. Espinoza, "State of the art of finite control set model predictive control in power electronics," *IEEE Trans. Ind. Informat.*, vol. 9, no. 2, pp. 1003-1016, May 2013.

[46] R. Vargas, P. Cotres, and U. Ammann, "Predictive control of a three-Phase neutral-point-clamped inverter," *IEEE Trans. Ind. Electron.*, vol. 54, no. 4, pp. 2697-2705, Oct. 2007.

[47] P. Cortes, J. Rodriguez, and C. Silva, "Delay compensation in model predictive current control of a three-phase inverter," *IEEE Trans. Ind. Electron.*, vol. 59, no. 2, pp. 1323-1325, Feb. 2012.

[48] P. Cortes, J. Rodriguez, and P. Antoniewicz, "Direct power control of an AFE using predictive control," *IEEE Trans. Power Electron.*, vol. 23, no. 5, pp. 2516-2523, Sep. 2008.

[49] T. He, D. Lu, and L. Li,"Model predictive sliding mode control for three-phase AC/DC converters," *IEEE Trans. Power Electron.*, DOI: 10.1109 / TPEL.2017.2783859.

[50] V. C. Gungor, B. Lu, and G. P. Hancke, "Opportunities and challenges of wireless sensor networks in smart grid," *IEEE Trans. Ind. Electron.*, vol. 57, no. 10, pp. 3557-3564, Oct. 2010.

[51] B. Sidhu, H. Singh, A. Chhabra,"Emerging wireless standards-WiFi, Zigbee and WiMAX," *World Academy of Science, Engineering and Technology*, vol. 25, pp. 308-313, 2007.

[52] Z. Md. Fadlullah, M. M. Fouda, and N. Kato,"Toward intelligent machine-to-machine communications in smart grid," *IEEE Communications Magazine*, pp. 60-65, Apr. 2011.

[53] IEEE 802.16 and WiMAX: Broadband Wireless Access for Everyone, Intel Corporation, 2003.

[54] H. K. Nguyen , and J. B. Song, "Optimal charging and discharging for multiple phevs with demand side management in vehicle-to-building," *Journal of Communications and Networks*, vol. 14, no.6, pp. 662-671, Dec. 2012.

[55] M. Esmaili, and M. Rajabi,"Optimal charging of plug-in electric vehicles observing power grid constraints," *IET Gener. Transm. Distrib.*, vol. 8, no. 4, pp. 583-590, Jun. 2014.

[56] M. Sjafie-khah, E. heydarian-Forushani, and G. J. Osório, " Optimal behavior of electric vehicle parking lots as demand response aggregation agents," *IEEE Trans. Smart Grid*, vol. 7, no. 6, pp. 2654-2665, Nov. 2016.

[57] H. Farzin, M. M. Aghtaie, and M. F. Firuzabad, "Reliability studies of distribution systems integrated with electric vehicles under battery-exchange mode," *IEEE Trans. Power Del.*, vol. 31, no. 6, pp. 2473-2482, Dec. 2016.

[58] E. Sortomme, and M. A. Ei-Sharkawi, "Optimal charging strategies for unidirectional Vehicle-to-Grid,"*IEEE Trans. Smart Grid*, vol. 2, no. 1, pp. 131-138, Mar. 2011.

[59] M. Kwon and S. Choi, "An electrolytic capacitorless bidirectional EV charger for V2G and V2H applications," *IEEE Trans. Power Electron.*, vol. 32, no. 9, pp. 6792-6799, Sept. 2017.

[60] Z. U. Zahid, Z. M. Dalala and R. Chen, "Design of bidirectional DC/DC resonant converter for vehicle-to-grid (V2G) applications," *IEEE Trans. Transport. Electrific.*, vol. 1, no. 5, pp. 232-244, Oct. 2015.

[61] Z. Yang, L. Sun, and M. Ke, "Optimal charging strategy for plug-in electric taxi with time-varying profits," *IEEE Trans. Smart Grid*, vol. 5, no. 6, pp. 2787-2797, Nov. 2014.

[62] Y. Mou, Z. Lin, M. Fu, "Decentralized optimal demand-side management for PHEV charging in a smart grid," *IEEE Trans. Smart Grid*, vol. 6, no. 2, pp. 726-736, Mar. 2015.

[63] W. Kempton, and J. Tomic, "Vehicle-to-grid power fundamentals: Calculating capacity and net revenue," *Journal of power sources*, vol. 144, no. 1, pp. 268-279, Jun. 2005.

[64] D. Anamika, and S. Santoso, "Electric vehicle charging on residential distribution systems: impacts and mitigations," *IEEE Access 3*, vol. 3, pp. 1871-1893, Sep. 2015.

[65] Z. Tian, Y. Wang and F. Zhang, "Real-time charging station recommendation system for electric-vehicle taxis," *IEEE Trans. Intell. Transp. Syst.*, vol. 17, no. 11, pp. 3098-3109, Apr. 2016.

[66] U. K. Madawala, and D. J. Thrimawithana, "A bidirectional inductive power interface for electric vehicles in V2G systems," *IEEE Trans. Ind. Electron.*, vol. 58, no. 10, pp. 4789-4796, Oct. 2011.

[67] C. Zhou, K. Qian, and M. Allan, "Modeling of the cost of EV battery wear due to V2G application in power systems," *IEEE Trans. Energy Convers.*, vol. 26, no. 4, pp. 1041-1050, Dec. 2011.

[68] M. A. Ortega-Vazquez, "Optimal scheduling of electric vehicle charging and vehicle-to-grid services at household level including battery degradation and price uncertainty," *IET Gener. Transm. Distrib.*, vol. 8, no. 6, pp. 1007-1016, 2014.

[69] S. Han, S. Han, K. Sezaki, "Estimation of achievable power capacity from plug-in electric vehicles for V2G frequency regulation: Case studies for market participation," *IEEE Trans. Smart Grid*, vol. 2, no. 4, pp. 632-641, Dec. 2011.

[70] R. Yu, J. Ding, and W. Zhong, "PHEV Charging and Discharging Cooperation in V2G Networks: A Coalition Game Approach," *IEEE Internet of Things J.*, vol. 1, no. 6, pp. 578-589, Dec. 2014.

[71] U. C. Chukwu, S. M. Mahajan, "Real-time management of power systems with V2G facility for smart-grid applications," *IEEE Trans. Sustain. Energy*, vol. 5, no. 2, pp. 558-566, Apr. 2014.

[72] C. Jin, J. Tang, and P. Ghosh, "Optimizing electric vehicle charging: a customer's perspective," *IEEE Trans. Veh. Technol.*, vol.62, no. 7, pp. 2919-2920, Sept. 2013.

[73] J. Hu, S. You, and M. Lind, "Coordinated Charging of Electric Vehicles for Congestion Prevention in the Distribution Grid," *IEEE Trans. Smart Grid*, vol. 5, no. 2, pp. 703-711, 2014.

[74] Y. He, B. Venkatesh, and L. Guan, "Optimal Scheduling for Charging and Discharging of Electric Vehicles," *IEEE Trans. Smart Grid*, vol. 3, no. 3, pp. 1095-1105, Sept. 2012.

[75] L. Zhang, T. Brown, and S. Samuelsen, "Evaluation of charging infrastructure requirements and operating costs for plug-in electric vehicles," *Journal of Power Sources*, vol. 240, no. 15, pp. 515-524, Oct. 2013.

[76] T. He, Y. Bai, and J. Zhu, "Optimal Charging Strategy of Electric Vehicles Customers in a Smart Electrical Car Park," *Proc. 8th IET Int. Conf. on Power Electronics, Machines and Drives (PEMD)*, Glasgow, UK, April 19-21, 2016.

[77] "Revolutionizing Fast Charging for Electric Vehicles," *Transportation Industry.* Available at: https://www.intel.com/content/dam/www/public/us/en/documents/solution-briefs/transportation-abb-terra-smart-connect-brief.pdf

[78] Australian Energy Market Operator (AEMO), Electricity Data, 2015. Available at: http://www.aemo.com.au/

[79] M. Yilmaz, and P. T. Krein, "Review of the impact of vehicle-to-grid technologies on distribution systems and utility interfaces," *IEEE Trans. Power Electron.*, vol. 28, no. 12, pp. 5673-5689, Dec. 2013.

[80] E. L. Karfopoulos, K. A. Panourgias, and N. D. Hatziargyriou, "Distributed coordination of electric vehicles providing V2G regulation services," *IEEE Trans. Power Syst.*, vol. 31, no. 4, pp. 2834-2846, Jul. 2016.

[81] M. J. E. Alam, M. Muttaqi, and D. Sutanto, "Effective utilization of available PEV battery capacity for mitigation of solar PV impact and grid support with integrated V2G functionality," *IEEE Trans. Smart Grid*, vol. 7, no. 3, pp. 1562-1571, May 2016.

[82] V. Monteiro, J. G. Pinto and J.L. Afonso, "Operation modes for electric vehicle in smart grids and smart homes: Present and proposed modes," *IEEE Trans. Veh. Technol.*, vol. 65, no. 3, pp. 1007-1020, 2016.

[83] Noguchi, T., Toniki, H., Kondo, S.: 'Direct Power Control of PWM Converter Without Power-Source Voltage Sensors', IEEE Trans. Ind. Appl., 1998, 34, (3), pp. 473–479

[84] W. Song, Z. Deng, and S. Wang, "A simple model predictive power control strategy for single-phase PWM converters with modulation function optimization," *IEEE Trans. Power Electron.*, vol. 31, no. 7, pp. 5279-5289, Jul. 2016.

[85] Y. Zhang, Y. Peng and H. Yang, "Performance improvement of two-vectors-based model predictive control of PWM rectifier," *IEEE Trans. Power Electron.*, vol. 31, no. 8, pp. 6016-6030, Aug. 2016.

[86] J. Rodriguez and P. Cortes, "Predictive control of power converters and electrical drives," in *A John Wiley & Sons, Ltd., Publication*, 1st ed. West Sussex, United Kingdom.

[87] M. P. Akter, S. Mekhilef, and N. M. L. Tan, "Modified model predictive control of a bidirectional ACDC converter based on Lyapunov function for energy storage systems," *IEEE Trans. Ind. Electron.*, vol. 63, no. 2, pp. 704-715, Feb. 2016.

[88] B. Singh, B. N. Singh and A, Chandra, "A review of three-phase improved power quality AC/DC converters," *IEEE Trans. Ind. Electron.*, vol. 51, no. 3, pp. 641-660, Jun. 2004.

[89] Y. Tao, Q. Wu, L. Wang, "Voltage sensorless predictive direct power control of three-phase PWM converters," *IET Power Electron.*, vol. 9, no. 5, pp. 1009-1018, 2016.

[90] J. Hu, J. Zhu, D. G. Dorrell, "In-depth study of direct power control strategies for power converters," *IET Power Electron.*, vol. 7, no. 7, pp. 1810-1820, 2014.

[91] P. Cortes, J. Rodrigues and D. E. Quevedo, "Predictive Current Control Strategy With Imposed Load Current Spectrum," *IEEE Trans. Power Electron.*, vol. 23, no. 2, pp. 612-618, Nov. 2008.

[92] Q. Xu, F. M, and Z. He, "Analysis and Comparison of Modular Railway Power Conditioner for High-Speed Railway Traction System," *IEEE Trans. Power Electron.*, vol. 32, no. 8, pp. 6031-6048, Aug. 2017.

[93] H. Zhao and L. Cheng, "Open Switch Fault Diagnostic Method for Back to Back Converters of Doubly Fed Wind Power Generation System," *IEEE Trans. Power Electron.*, to be published, DOI: 10.1109/TPEL.2017.2705985

[94] M. Davari, and Y. A. I. Mohamed, "Robust multi-objective control of VSC-based dc-voltage power port in hybrid ac/dc multi-terminal micro-grids," *IEEE Trans. Smart Grid*, vol. 4, no. 3, pp. 1597-1612, Mar. 2013.

[95] Y. Li, X. Shi, and B. Liu, "Development, Demonstration, and Control of a Testbed for Multiterminal HVDC System," *IEEE Trans. Power Electron.*, vol. 32, no. 8, pp. 6069-6078, Aug. 2017.

[96] S. K. Kim, D. K. Choi, and K. B. Lee, "Offset-Free Model Predictive Control for the Power Control of Three-Phase AC/DC Converters," *IEEE Trans. Power Electron.*, vol. 62, no. 11, pp. 7114-7126, Nov. 2015.

[97] Y. Zhang and C. Qu, "Table-Based Direct Power Control for Three-Phase AC/DC Converters Under Unbalanced Grid Voltages," *IEEE Trans. Power Electron.*, vol. 30, no. 12, pp. 7090-7099, Dec. 2015.

[98] S. C. Shin, H. J. Lee, and Y. H. Kim, "Transient Response Improvement at Startup of a Three-Phase AC/DC Converter for a DC Distribution System in Commercial Facilities," *IEEE Trans. Power Electron.*, vol. 29, no. 12, pp. 6742-6753, Dec. 2014.

[99] J. Liu, Y. Gao, and W. Luo, "TakagiSugeno fuzzy-model-based control of three-phase AC/DC voltage source converters using adaptive sliding mode technique," *IET Control Theory Appl.*, vol. 11, no. 8, pp. 1255-1263, 2017.

[100] R. Kadri, J. P. Gaubert, and G. Champenois, "An Improved Maximum Power Point Tracking for Photovoltaic Grid-Connected Inverter Based on Voltage-Oriented Control," *IEEE Trans. Ind. Electron.*, vol. 58, no. 1, pp. 66-75, Jan. 2011.

[101] W. Shireen, R. a. Kulkari, and M. Arefeen, "Analysis and minimization of input ripple current in PWM inverters for designing reliable fuel cell power systems," *Journal of Power Sources*, vol. 156, no. 2, pp. 448-454, Jun. 2006.

[102] J. Dannehl, C. Wessels, and F. W. Fuchs, "Limitations of voltage-oriented PI crrent control of grid-connected PWM rectifiers with LCL filters," *IEEE Trans. Ind. Electron.*, vol. 56, no. 2, pp. 380-388, Feb. 2009.

[103] Y. Zhang, W. Xie, and Z. Li, "Model predictive direct power control of a PWM rectifier with duty cycle optimization," *IEEE Trans. Power Electron.*, vol. 28, no. 11, pp. 5343-5351, Nov. 2013.

[104] Y. Cho and K. B. Lee, "Virtual-Flux-Based Predictive Direct Power Control of Three-Phase PWM Rectifiers With Fast Dynamic Response," *IEEE Trans. Power Electron.*, vol. 31, no. 4, pp. 3348-3359, Apr. 2016.

[105] J. Han, S. K. Solanki, and J. Solanki, "Coordinated predictive control of a wind/Battery Microgrid System," *IEEE J. of Emerg. Sel. Topics Power Electron.*, vol. 1, no. 4, pp. 296-305, Dec. 2013.

[106] Y. Zhang and C. Qu, "Direct Power Control of a Pulse Width Modulation Rectifier Using Space Vector Modulation Under Unbalanced Grid Voltages," *IEEE Trans. Power Electron.*, vol. 30, no. 10, pp. 5892-5901, Oct. 2015.

[107] D. K. Choi and K. B. Lee, "Dynamic performance improvement of AC/DC converter using model predictive direct power control with finite control set," *IEEE Trans. Ind. Electron.*, vol. 62, no. 2, pp. 757-767, Feb. 2015.

[108] S. Kwak and J. C. Park, "Model-predictive direct power control with vector preselection technique for highly efficient active rectifiers," *IEEE Trans. Ind. Informat.*, vol. 11, no. 1, pp. 44-52, Sep. 2015.

[109] J. Ma, W. Song, and S. Jiao, "Power calculation for direct power control of single-phase three-level rectifiers without phase-locked loop," *IEEE Trans. Ind. Electron.*, vol. 63, no. 5, pp. 2871-2882, May 2016.

[110] J. Knight, S. Shirsavar and W. Holderbaum, "An improved reliability cuk based solar inverter with sliding mode control," *IEEE Trans. Power Electron.*, vol. 21, no. 4, pp. 1107-1115, Jul. 2006.

[111] D. Cao and J. Fei, "Adaptive Fractional Fuzzy Sliding Mode Control for Three-Phase Active Power Filter," *IEEE Access*, vol. 4, pp. 6645-6651, 2016.

[112] F. Sebaaly, H. Vahedi, and H. Y. Kanaan, "Sliding mode fixed frequency current controller design for grid-connected NPC inverter," *IEEE J. of Emerg. Sel. Topics Power Electron.*, vol. 4, no. 4, pp. 1397-1405, Oct. 2016.

[113] J. J. More, P. F. Puleston, and C. Kunusch, "Development and implementation of a supervisor strategy and sliding mode control setup for fuel-cell-based hybrid generation systems," *IEEE Trans. Energy Convers.*, vol. 30, no. 1, pp. 218-225, Mar. 2015.

[114] X. Zhang, L. Sun, and K. Zhao, "Nonlinear speed control for PMSM system using sliding-mode control and disturbance compensation techniques," *IEEE Trans. Power Electron.*, vol. 28, no. 3, pp. 1358-1365, Mar. 2013.

[115] N. Derbel, J. Ghommam, and Q. Zhu, "Applications of sliding mode control" in *Springer Singapore*, vol. 79, Studies in Systems, Decision and Control, N. Derbel, Ed., 1st ed. Sfax, Tunisia: University of Sfax, 2017, pp. 335-337.

[116] O. L. Santos, L. M. Salamero, and G. Garcia, "Robust sliding-mode control design for a voltage regulated quadratic boost converter," *IEEE Trans. Power Electron.*, vol. 30, no. 4, pp. 2313-2327, Apr. 2015.

[117] J. Lee, S. Khoo, and Z. Wang, "DSP-based sliding-mode control for electromagnetic-levitation precise-position system," *IEEE Trans. Ind. Informat.*, vol. 9, no. 2, pp. 817-827, May 2013.

[118] J. F. Silva, "Sliding-mode control of boost-type unity-power-factor PWM rectifiers," *IEEE Trans. Ind. Electron.*, vol. 46, no. 3, pp. 594-603, Jun 1999.

[119] S. Li, M. Li, and X. Yu, "Design and implementation of terminal sliding mode control method for PMSM speed regulation system," *IEEE Trans. Ind. Informat.*, vol. 9, no. 4, pp. 1879-1891, Nov. 2013.

[120] T. He, L. L, and J. Zhu, "A novel model predictive sliding mode control for AC/DC converters witho voltage and load resistance variations," *IEEE Energy Conversion Congress and Exposition (ECCE)*, Milwaukee, USA, Sep. 18-22, 2016.

[121] M. P. Kazmierkowski, F. Blaabjerg, and R. Krishnan, "Control power electronics: Selected problems," *Academic Press*, California, USA, pp. 117-121, 2002.

[122] M. T. Sebastiani, R. Lüders, and KV. O. Fonseca, "Evaluating electric bus operation for a real-world BRT public transportation using simulation optimization," *IEEE Trans. Intell. Transp. Syst.*, vol. 17, pp. 2777-2786, 2016.

[123] K. Kandasamy, D. M. Vilathgamuwa, and U. K. Madawala, "Inductively coupled modular battery system for electric vehicles," *IET Power Electron.*, vol. 9, no. 3, pp. 600-609, 2016.

[124] S. Hu, Z. Zhang, and Y. Chen, "A new integrated hybrid power quality control system for electrical railway," *IEEE Transactions on Ind. Electron.*, vol. 62, no. 10, pp. 6222-6232, 2015.

[125] V. Monteiro, J. P. Carmo, and J. G. Pinto, "A flexible infrastructure for dynamic power control of electric vehicle battery chargers," *IEEE Trans. Veh. Technol.*, vol. 65, no. 6, pp. 4535-4547, Jun. 2016.

[126] J. Guanetti, S. Formentin, and S. M. Savaresi, "Energy management system for an electric vehicle with a rental range extender: A least costly approach," *IEEE Trans. Intell. Transp. Syst.*, vol. 17, no. 11, pp. 3022-3034, 2016.

[127] F. Akar, Y. Tavlasoglu, and E. Ugur, "A bidirectional non-isolated multi input DC-DC converter for hybrid energy storage systems in electric vehicles," *IEEE Trans. Veh. Technol.*, vol. 65, no. 10, pp. 7944-7955, 2016.

[128] F. Yi and W. Cai, "Modeling, control, and seamless transition of the bidirectional battery-driven switched reluctance motor/generator drive based on integrated multiport power converter for electric vehicle applications," *IEEE Trans. Power Electron.*, vol. 31, no. 10, pp. 7099-7111, 2016.

[129] Z. Liu, D. Wang, and H. Jia, "Aggregation and bidirectional charging power control of plug-in hybrid electric vehicles: Generation system adequacy analysis," *IEEE Trans. Sustain. Energy*, vol. 6, no. 2, pp. 325-335, 2015.

[130] G. Waltrich, M. A. M. Hendrix, and J. Duarte, "Three-phase bidirectional DC/DC converter with six inverter legs in parallel for EV applications," *IEEE Trans. Ind. Electron.*, vol. 63, no. 3, pp. 1372-1384, 2016.

[131] P. Kong and G. K. Karagiannidis, "Charging schemes for plug-in hybrid electric vehicles in smart grid: A survey," *IEEE Access 4*, pp. 6846-6875, 2016.

[132] M. N. Mojdehi and P. Ghosh,"An On-Demand Compensation Function for an EV as a Reactive Power Service Provider," *IEEE Trans. Veh. Technol.*, vol. 65, no. 6, pp. 4572-4583, 2016.

[133] H. Tanaka, F. Ikeda, and T. Tanaka,"Novel reactive power control strategy based on constant DC-capacitor voltage control for reducing the capacity of smart charger for electric vehicles on single-phase three-wire distribution feeders," *IEEE J. Emerg. Sel. Top. Power Electron.*, vol. 4, no. 2, pp. 481-488, 2016.

[134] Y. Zhang, J. Long, and Y. Zhang,"Table-based direct power control for three-level neutral point-clamped pulse-width modulated rectifier," *IET Power Electron.*, vol. 6, no. 8, pp. 1555-1562, 2013.

[135] A. Sannino, G, Postiglione, and M. H. J. Bollen,"Feasibility of a DC network for commercial facilities," *IEEE Trans. Ind. Appl.*, vol. 39, no. 5, pp. 1499-1507, 2003.

[136] S. Rivera, B. Wu, and S. Kouro,"Electric vehicle charging station using a neutral point clamped converter with bipolar DC bus," *IEEE Trans. Ind. Electron.*, vol. 62, no. 4, pp. 1499-1507, 2015.

[137] L. Zhang, K. Sun, and Y. Xing,"A modular grid-connected photovoltaic generation system based on DC bus," *IEEE Trans. Power Electron.*, vol. 26, no. 2, pp. 523-531, 2011.

[138] M. Wang, A. Q. Huang, and W. Yu,"A novel distributed PV system with ultra-high-frequncy-AC bus for residential applications," *2014 IEEE Energy Conversion Congress and Exposition (ECCE)*, Pittsburgh, PA, 2014, pp. 2328-2334.

List of Publications

Journal Papers

J-1. **Tingting He**, Dylan Lu, Li Li, Jianwei Zhang, Linfeng Zheng, Jianguo Zhu, "Model predictive sliding mode control for three-phase AC/DC converters," *IEEE Trans. Power Electron.*, DOI: 10.1109 / TPEL.2017.2783859.

J-2. **Tingting He**, Jianguo Zhu, Dylan Lu, and Linfeng Zheng, "Modified model predictive control for bidirectional four-quadrant EV chargers with extended set of voltage vectors," Submitted to *IEEE Trans. J. Emerging and Selected Topics in Power Electron.*, Accepted.

J-3. **Tingting He**, Jianguo Zhu, Dylan Lu, and Linfeng Zheng, "Model predictive control of a bidirectional EV charger with dynamic references," Submitted to *IEEE Trans. Power Electron.*, Under review.

Conference Papers

C-1. **Tingting He**, Yingjie Bai, and Jianguo Zhu, "Optimal charging strategy of electric vehicles customers in a smart electrical car park," *The 8th IET International Conference on Power Electronics, Machines and Drives (PEMD 2016)*, Glasgow, UK, 19-21 Apr., 2016.

C-2. **Tingting He**, Li Li, Jianguo Zhu and Linfeng Zheng, "A novel model predictive sliding mode control for AC/DC converters with output voltage and load resistance variations," *2016 IEEE Energy Conversion Congress and Exposition (ECCE 2016)*, Milwaukee, WI, 18-22 Sept., 2016.

C-3. **Tingting He**, Dylan Lu, Linfeng Zheng, and Jianguo Zhu, "Moving average

filter-based model predictive control for electric vehicles bidirectional chargers," *The 20th International Conference on Electrical Machines and Systems (IECMS 2017)*, Sydney, Australia, 11-14, Aug. 2017.

C-4. **Tingting He**, Jianguo Zhu Dylan Lu, and Linfeng Zheng, "Comparison study of electric vehicles charging stations with AC and DC buses for bidirectional power flow in smart car parks," *The 43rd Annual Conference of the IEEE Industrial Electronics Society (IECON 2017)*, Beijing, China, 29 Oct. - 1 Nov. 2017.